

University of Windsor

Scholarship at UWindor

Electronic Theses and Dissertations

Theses, Dissertations, and Major Papers

2002

Modeling and optimization of non-phased two-dimensional ultrasonic arrays.

Alexey A. Denisov
University of Windsor

Follow this and additional works at: <https://scholar.uwindsor.ca/etd>

Recommended Citation

Denisov, Alexey A., "Modeling and optimization of non-phased two-dimensional ultrasonic arrays." (2002). *Electronic Theses and Dissertations*. 2751.
<https://scholar.uwindsor.ca/etd/2751>

This online database contains the full-text of PhD dissertations and Masters' theses of University of Windsor students from 1954 forward. These documents are made available for personal study and research purposes only, in accordance with the Canadian Copyright Act and the Creative Commons license—CC BY-NC-ND (Attribution, Non-Commercial, No Derivative Works). Under this license, works must always be attributed to the copyright holder (original author), cannot be used for any commercial purposes, and may not be altered. Any other use would require the permission of the copyright holder. Students may inquire about withdrawing their dissertation and/or thesis from this database. For additional inquiries, please contact the repository administrator via email (scholarship@uwindsor.ca) or by telephone at 519-253-3000ext. 3208.

MODELING AND OPTIMIZATION OF NON-PHASED 2D
ULTRASONIC ARRAYS

By
Alexey A. Denisov

A DISSERTATION
SUBMITTED TO THE FACULTY OF GRADUATE STUDIES AND RESEARCH
THROUGH THE DEPARTMENT OF PHYSICS
IN PARTIAL FULFILLMENT OF THE REQUIREMENTS FOR
THE DEGREE OF DOCTOR OF PHILOSOPHY
AT THE UNIVERSITY OF WINDSOR

WINDSOR, ONTARIO

JULY 2002

© Copyright by Alexey A. Denisov, 2002



National Library
of Canada

Bibliothèque nationale
du Canada

Acquisitions and
Bibliographic Services

Acquisitions et
services bibliographiques

395 Wellington Street
Ottawa ON K1A 0N4
Canada

395, rue Wellington
Ottawa ON K1A 0N4
Canada

Your file *Votre référence*
ISBN: 0-612-92536-6
Our file *Notre référence*
ISBN: 0-612-92536-6

The author has granted a non-exclusive licence allowing the National Library of Canada to reproduce, loan, distribute or sell copies of this thesis in microform, paper or electronic formats.

L'auteur a accordé une licence non exclusive permettant à la Bibliothèque nationale du Canada de reproduire, prêter, distribuer ou vendre des copies de cette thèse sous la forme de microfiche/film, de reproduction sur papier ou sur format électronique.

The author retains ownership of the copyright in this thesis. Neither the thesis nor substantial extracts from it may be printed or otherwise reproduced without the author's permission.

L'auteur conserve la propriété du droit d'auteur qui protège cette thèse. Ni la thèse ni des extraits substantiels de celle-ci ne doivent être imprimés ou autrement reproduits sans son autorisation.

In compliance with the Canadian Privacy Act some supporting forms may have been removed from this dissertation.

Conformément à la loi canadienne sur la protection de la vie privée, quelques formulaires secondaires ont été enlevés de ce manuscrit.

While these forms may be included in the document page count, their removal does not represent any loss of content from the dissertation.

Bien que ces formulaires aient inclus dans la pagination, il n'y aura aucun contenu manquant.

Canada

Abstract

Ultrasonic image acquisition with non-phased 2D arrays is a relatively new method in NDE inspection. Historically, ultrasonic array development progressed mostly in the medical imaging where phased arrays found a great application. However, in the field of NDE inspection of metals, heavy plastics and composites, and many other materials the applicability of phased arrays is often restricted due to physical limitations. On the other hand, using versatile systems with mechanical scanning is not always convenient. Therefore, non-phased arrays of independent elements have a strong potential for becoming a valuable tool for rapid ultrasonic image acquisition in the industrial environment as well as in many other areas where conventional methods may not be applicable. The main motivation of this work is to build the necessary mathematical apparatus for estimating the process of signal and image formation in such systems. A model of signal penetration through a complex multilayered structure with non-parallel interfaces is discussed in the plane-wave approximation. This model is then refined to finite-size transducers and finite-size defects inside the sample. A new method of obtaining the beam structure in such multi-layered media is presented. The advantage of this method is that it allows for a very fast calculation while the precision is still comparable to more precise and more computationally expensive methods. A new method of calculating the response of the transducer to defects inside the sample is presented and discussed. The results of numerical calculations using these two methods are discussed and compared with experimental data. Using these models, image formation algorithms together with new image refining techniques are discussed.

To my family

Aknowledgements

This work was carried out at the Centre for Imaging Research and Advanced Materials Characterization, School of Physical Sciences, University of Windsor.

I would like to express my sincere gratitude to Roman Gr. Maev, Professor, Head of the Centre, for support, advice, and excellent working conditions. It is hard to imagine this project would succeed without his energy and insight.

My sincere gratitude is due to Serge Titov and Andrei Ptchelintsev whose knowledge and expertise in the area of ultrasound, engineering and electronics has been an inexhaustible source for me and a crucial resource for developing our own array system.

My deepest respect and appreciation is due to Elena Maeva and other members of the Centre and the School of Physical Sciences for their work and great support.

I would be remiss if I did not mention our secretaries Sarah Beneteau, Emily Schmidt and Sharon Horne, who I bothered repeatedly and was rewarded only by their kindness and generosity.

Of course, all of this would have no meaning if I did not thank my parents. There will never be enough words to express my love and convey my deepest appreciation for their support, encouragement, and patience.

Contents

List of Tables	viii
List of Figures	ix
1 Introduction	1
2 Basic Principles	6
2.1 Propagation of Elastic Waves in Unbounded Media	7
2.2 Reflection and Transmission	14
2.2.1 General Boundary Conditions	15
2.2.2 Reflection and Transmission at a Solid-Solid Interface	19
2.2.3 Reflection and Transmission at a Fluid→Solid Interface	24
2.2.4 Longitudinal Wave Incidence on a Solid→Fluid Interface	25
2.2.5 Shear (SV) Wave Incidence on a Solid→Fluid Interface	26
2.2.6 Reflection of a Shear (SH) Wave from an Interface	28
2.3 Attenuation	29
3 Reflection and Refraction at Multiple Interfaces	32
3.1 The Measurement Model	32
3.1.1 Reflection and Transmission at the Delay-Coupling Interface	35
3.1.2 Reflection and Transmission at the Coupling-Sample Interface	36
3.1.3 Reflection from the Defect	40

3.1.4	Combining Reflection and Transmission Factors	40
4	Modeling Matrix Transducer Elements	44
4.1	The Piston Transducer Model	45
4.2	Stationary Phase Approach	48
4.3	Propagation through Interfaces—Direct Calculation	51
4.4	Equivalent Transformations	52
4.5	Calculating the Detected Signal	56
4.6	Comparing Different Methods	59
5	Studying the Behavior of the Model	65
5.1	Specifying the Reference System	65
5.2	Influence of Delay Line and Immersion Layer	68
5.3	Influence of Defect Location and Orientation	71
5.4	Dependence on Transducer Frequency	75
5.5	Obtaining Images	79
6	Conclusions and Future Work	86
A	MathCAD Source for Obtaining Transmission and Reflection Factors	89
B	Obtaining Angle of Incidence from Discrete Phase Values	108
	Bibliography	110

List of Tables

3.1 Mechanical properties of some materials 33

5.1 Parameters of the modelled system 66

List of Figures

2.1	Polarization of the acoustic wave relative to the interface	15
2.2	Reflection and transmission of a plane longitudinal and shear wave in general case	16
2.3	Reflection and transmission of a plane longitudinal wave at a fluid-solid interface	24
2.4	Reflection and transmission of a plane longitudinal wave at a solid-fluid interface	26
2.5	Reflection and transmission of a shear (SV) wave at a solid-fluid interface	27
3.1	A simplified model of the measurement system	34
3.2	Reflection and transmission at the immersion–delay interface	37
3.3	Reflection and transmission at the delay–immersion interface	37
3.4	Reflection and transmission at the immersion–sample interface	37
3.5	Reflection and transmission at the sample–immersion interface, P-wave incidence	38
3.6	Reflection and transmission at the sample–immersion interface, SV- wave incidence	38
3.7	Reflection from the void defect, P-wave incidence	39
3.8	Reflection from the void defect, SV-wave incidence	39
3.9	Conversion of wave modes inside the sample	41

3.10	Effective reflection factors from a flat-parallel defect	42
3.11	Effective angles and reflection factors, flat-parallel defect, $\phi = 0^\circ$	43
3.12	Effective angles and reflection factors, flat-parallel defect, $\phi = 10^\circ$	43
4.1	A planar piston transducer model	45
4.2	The amplitude of pressure distribution for a flat square transducer	47
4.3	On-axis pressure for circular and rectangular transducers	48
4.4	Propagation of a wave through an interface along a ray path	53
4.5	Geometrical interpretation of equivalent transformations	54
4.6	Equivalent transformation for multiple interfaces	55
4.7	General model for obtaining detected signal	56
4.8	Comparison of exact calculations with the method of equivalent transformations	61
4.9	Using different approximations to calculate transducer response	63
4.10	Comparing experimental and theoretical results	64
5.1	Dependence of signal on transducer tilt for reference system	67
5.2	Dependence of the signal on thickness of delay line	69
5.3	Angular sensitivity for different thicknesses of delay line	69
5.4	Influence of immersion layer thickness	70
5.5	Dependence of the signal on thickness of the water column	70
5.6	Angular sensitivity for various thicknesses of the water column	71
5.7	Reflection amplitudes vs. defect depth for various sizes of defects	72
5.8	Dependence of the reflected signal on defect tilt for various defect sizes	73
5.9	Lateral displacement of defects and partial coverage	73
5.10	Dependence of reflected signal on lateral defect displacement for various defect sizes	74

5.11	Choosing the effective size of the matrix element	76
5.12	Effective sizes of matrix elements	77
5.13	Dependence on transducer frequency	78
5.14	Frequency shift for two different angles of transducer	79
5.15	A typical waveform received by the element of a transducer	80
5.16	The matrix transducer and calibration samples	83
5.17	Interpolated images of calibration sample	84
B.1	Phase delays on a rectangular grid	108

CHAPTER 1

Introduction

Acoustical imaging is one of the important applications of ultrasound. For many researchers the ability to visualize the distribution of mechanical properties has been a driving force in developing new and improving existent methods and techniques in this area. Today we have methods for studying live cell structures and locating sunken ships on the sea bottom, obtaining images of an embryo and finding corrosion under paint films, checking for structural integrity in novel composites and mapping elastic properties of various materials on the nanoscale.

To build an image, the information on mechanical properties should be obtained at different locations in the sample; therefore, some sort of scanning is involved. The two common scanning methods are mechanical scanning and phased arrays with a synthetic aperture. Mechanical scanning is mostly used in desktop systems, such as scanning acoustic microscopes, or industrial *nondestructive evaluation* (NDE) systems based on a 3D mechanical scan in a water tank. In such systems the ultrasonic probe is moved in one, two, or three dimensions relative to the investigated object collecting

information at each scanning point. The systems based on the principle of synthetic aperture, also known as beam steering, scan the studied object by sending ultrasonic waves in a specific direction. To achieve that, an electric pulse is delivered to piezoelectric elements in the array with slightly different delays; the time lag is controlled mechanically or electronically to produce the required shape of the wavefront.

The non-phased array transducers, discussed in this dissertation, are simpler than phased arrays. The design of the probe incorporates a two-dimensional matrix of transducers, where each element functions both as transmitter and receiver of ultrasonic waves. Instead of working in ensemble with other elements to synthesize the aperture, each element of the matrix works independently. Common principles on which the function of the array is based are the same as in many pulse-echo ultrasonic devices [1, 2, 3, 4, 5, 6]. The construction of the probe is also in many ways similar to the phased arrays [7, 8, 9, 10, 11, 12, 13, 14] and is described in [15, 16]. There are some important differences, however. For example, the ratio of the element size to the wavelength is larger, and there is more power feed to each element in the array.

The resolution of non-phased arrays is limited by the size of its elements. There is always a compromise between the sensitivity of the array and its resolution. Arrays with higher density provide better resolution, however there are both manufacturing and physical limitations on how small the element can be. From the point of view of manufacturing, it is harder to provide sufficient power to smaller elements of the array and it is more difficult to build high density arrays with uniform properties across all the elements. At the same time, smaller element sizes result in a larger spreading of the beam causing blurring of the image and more energy loss. Another important issue involves the angular stability of the system. That is, how the probe sensitivity is affected by its orientation to surface of the sample.

Comparing characteristics of non-phased arrays with their phased siblings or systems with mechanical scanning is not a rewarding task now, at the early stages of their development. The signal to noise ratio is insufficient for obtaining images with high contrast, the spatial resolution is low, there are no arrays with focused elements available at the moment, and finally, the manufacturing price is relatively high. On the other hand, there are many application areas where neither mechanical scanning, nor phased arrays can be used. Regarding the mechanical scanning systems, they are fragile, heavy and there are just a few of them designed in portable implementations. At present they cannot achieve the level of miniaturization and robustness already available with phased and non-phased arrays. The phased arrays, historically, were designed for medical application and due to physical limitations they cannot be used effectively for inspection of metals, dense plastics and composites. In addition, the true 2D phased arrays are only in the development stage at present. Therefore, despite all the issues with non-phased arrays, they seem to have a strong potential of becoming a valuable tool for rapid ultrasonic image acquisition in the industrial environment as well as in many other areas where usage of conventional methods is restricted. With advances in piezomaterials, transducer manufacturing, electronics, and other related areas this technology is becoming a real portable alternative to desktop acoustical scanners.

The present dissertation is a part of a larger project carried out in the Centre for Imaging Research and Advanced Materials Characterization, in the University of Windsor. The main goal of this project is to build a 2D non-phased array system. The objectives of this project include:

- developing technologies for manufacturing non-phased 2D transducers;
- developing electronics which includes pulser-receiver, multi-channel multiplexer,

digital-to-analog converter, and a controller;

- developing controlling software together with signal and image processing methods;
- developing computer vision or fuzzy logic algorithms for automatic recognition and measurement of defects or structural features.

The more we understand the physics behind the function of the array transducer the more effectively many of these tasks can be fulfilled. Here are some of the advantages to having a consistent mathematical model of transducer operation:

- choosing the characteristics of the transducer, such as size, frequency, immersion, delay line, etc. to develop an optimal configuration for a specific task
- developing new methods for signal and image processing
- generating artificial data sets for tuning and testing the image processing methods and computer vision/fuzzy logic algorithms

We begin in Chapter 2 by reviewing the basic principles of wave propagation in continuous unbounded media, extending this knowledge to the reflection and transmission problem at various types of interfaces. Unfortunately, in many books the solution for reflection and transmission factors contains errors, so a lot of attention is focused on deriving these equations accurately.

The equations obtained are used in Chapter 3 to study the reflection and transmission problem numerically. In addition, a more complex case of multiple media and interfaces is discussed. In this chapter we start formulating the mathematical model of a single transducer element.

In Chapter 4, the beam structure of a finite size transducer element is discussed. We also demonstrate how the structure of the beam can be obtained in the stationary

phase approximation. For multiple interfaces, using a high-frequency approximation obtained in [1], a method of equivalent transformations is derived. In the paraxial approach, this method has more restricted applicability, however its performance is much higher. In the stationary phase approximation, it allows obtaining the beam structure analytically. In addition, we show the method of calculating the signal received by the transducer operating in the reflective mode. The advantage of this method is that it does not require calculating the beam structure of the reflected wave. Only the structure of the forward propagating wave, location, orientation, and material of the defect are required to estimate the response of the transducer. The methods and approximations described in this chapter are compared and the differences are discussed. In addition, we demonstrate that results of our mathematical model are consistent with experiment.

In Chapter 5, we study the behavior of the model in various configurations. Several virtual experiments are staged to illustrate how the model responds to changes in size and frequency of the transducer element, properties of the immersion, location and orientation of the defect, etc. Finally we discuss the process of image formation and demonstrate several methods to improve the quality and stability of the images obtained.

CHAPTER 2

Basic Principles

This chapter presents an overview of basic physical aspects of elastic wave propagation, covering questions of reflection, refraction and dissipation of the ultrasound. The discussion starts with a derivation of the basic equations describing the physical effects created by external forces acting upon continuum elastic media. These equations create a basis with which to study the propagation of waves in continuous media. The next step is investigating the propagation of acoustic waves through interfaces, where expressions for reflection and transmission factors are discussed. Derived for various types of interfaces between fluids and solids, these factors provide necessary tools for studying propagation of ultrasonic beams in complex multi-layer structures. Finally, various mechanisms and effects of attenuation are considered.

2.1 Propagation of Elastic Waves in Unbounded Media

Prior to studying the propagation of sound in complex systems with multiple materials and interfaces, we need to understand the basic principles of sound wave propagation in unbounded media.

The starting point of this discussion is the principle of conservation of linear momentum within an arbitrary volume. Expressed in terms of particle displacement u , it can be written in Cartesian coordinates as

$$\frac{\partial \sigma_{ij}}{\partial x_i} + \rho b_j = \rho \ddot{u}_j; \quad i, j = 1, 2, 3; \quad (2.1)$$

where σ_{ij} is the *stress tensor*, ρ is the density, b_j is the body force per unit mass, and \ddot{u}_j is the particle acceleration. This equation is sometimes called the Cauchy equation of motion. In a normal environment, the body forces, such as gravity, are negligible.

The principle of conservation of angular momentum is satisfied if the stress tensor σ is symmetrical (see, for example, [17], or [18])

$$\sigma_{ij} = \sigma_{ji}. \quad (2.2)$$

The *strain tensor*, also referred as the Lagrangian strain tensor is related to particle displacement u as

$$\varepsilon_{ij} = \frac{1}{2} \left(\frac{\partial u_i}{\partial x_j} + \frac{\partial u_j}{\partial x_i} + \frac{\partial u_m}{\partial x_i} \frac{\partial u_m}{\partial x_j} \right). \quad (2.3)$$

For small deformations, the product terms in equation (2.3) can be neglected. Under these conditions the strain tensor is

$$\varepsilon_{ij} = \frac{1}{2} \left(\frac{\partial u_i}{\partial x_j} + \frac{\partial u_j}{\partial x_i} \right). \quad (2.4)$$

The relationship between the strain and the related stress is a property of the material; it is described by *constitutive equations*. If the continuum media is a linear

and elastic material, these stress-strain relations are referred to as the *generalized Hooke's law*:

$$\sigma_{ij} = c_{ijkl}\varepsilon_{kl} \quad (2.5)$$

where c_{ijkl} is the *elastic stiffness tensor*. The generalized Hooke's law by itself is nothing more than a statement that the stress is proportional to the gradient of deformation occurring in the material. These equations assume a linear relationship between the components of the stress tensor and strain tensor, which is generally valid for the case of small deformations. In this thesis, we focus our attention on matrix transducers which produce ultrasonic waves with amplitudes below the level where nonlinear effects can be observed. The vast majority of ultrasonic NDE equipment operates in linear mode.

Since the stress σ and strain ε are tensors, we can conclude that the stiffness is a fourth order tensor. Due to the symmetry of the stress and strain tensors, the stiffness tensor must satisfy the relation

$$c_{ijkl} = c_{ijlk} = c_{jikl} = c_{jilk}; \quad (2.6)$$

and, in general, only 36 of the 81 constants are independent.

To simplify the analysis, it is common to replace the components of tensors by introducing new quantities:

$$\begin{bmatrix} \varepsilon_{11} & \varepsilon_{12} & \varepsilon_{13} \\ \varepsilon_{21} & \varepsilon_{22} & \varepsilon_{23} \\ \varepsilon_{31} & \varepsilon_{32} & \varepsilon_{33} \end{bmatrix} = \begin{bmatrix} \varepsilon_1 & \varepsilon_4 & \varepsilon_5 \\ \varepsilon_4 & \varepsilon_2 & \varepsilon_6 \\ \varepsilon_5 & \varepsilon_6 & \varepsilon_3 \end{bmatrix}; \quad (2.7)$$

similarly

$$\begin{bmatrix} \sigma_{11} & \sigma_{12} & \sigma_{13} \\ \sigma_{21} & \sigma_{22} & \sigma_{23} \\ \sigma_{31} & \sigma_{32} & \sigma_{33} \end{bmatrix} = \begin{bmatrix} \sigma_1 & \sigma_4 & \sigma_5 \\ \sigma_4 & \sigma_2 & \sigma_6 \\ \sigma_5 & \sigma_6 & \sigma_3 \end{bmatrix}. \quad (2.8)$$

The strain tensor can now be expressed as

$$\begin{bmatrix} \varepsilon_1 \\ \varepsilon_2 \\ \varepsilon_3 \\ \varepsilon_4 \\ \varepsilon_5 \\ \varepsilon_6 \end{bmatrix} = \begin{bmatrix} \frac{\partial u_1}{\partial x_1} \\ \frac{\partial u_2}{\partial x_2} \\ \frac{\partial u_3}{\partial x_3} \\ \frac{1}{2} \left(\frac{\partial u_1}{\partial x_2} + \frac{\partial u_2}{\partial x_1} \right) \\ \frac{1}{2} \left(\frac{\partial u_2}{\partial x_3} + \frac{\partial u_3}{\partial x_2} \right) \\ \frac{1}{2} \left(\frac{\partial u_3}{\partial x_1} + \frac{\partial u_1}{\partial x_3} \right) \end{bmatrix}. \quad (2.9)$$

In this notation, the generalized Hooke's law becomes

$$\sigma_i = c_{ij}\varepsilon_j; \quad i, j = 1, \dots, 6; \quad (2.10)$$

where

$$\begin{aligned} c_{n1} &= c_{ij11} & c_{n4} &= c_{ij12} \\ c_{n2} &= c_{ij22} & c_{n5} &= c_{ij13} \\ c_{n3} &= c_{ij33} & c_{n6} &= c_{ij23}; \end{aligned} \quad (2.11)$$

and

$$n = \begin{cases} i, & i = j = 1, 2 \text{ or } 3 \\ i + j + 1, & i \neq j \text{ and } i = 1 \text{ or } 2. \end{cases} \quad (2.12)$$

Furthermore, for isotropic materials, the additional axes of symmetry will result in further reduction of the elastic stiffness tensor

$$\begin{bmatrix} \sigma_1 \\ \sigma_2 \\ \sigma_3 \\ \sigma_4 \\ \sigma_5 \\ \sigma_6 \end{bmatrix} = \begin{bmatrix} c_{11} & c_{12} & c_{12} & 0 & 0 & 0 \\ c_{12} & c_{11} & c_{12} & 0 & 0 & 0 \\ c_{12} & c_{12} & c_{11} & 0 & 0 & 0 \\ 0 & 0 & 0 & c_{44} & 0 & 0 \\ 0 & 0 & 0 & 0 & c_{44} & 0 \\ 0 & 0 & 0 & 0 & 0 & c_{44} \end{bmatrix} \begin{bmatrix} \varepsilon_1 \\ \varepsilon_2 \\ \varepsilon_3 \\ \varepsilon_4 \\ \varepsilon_5 \\ \varepsilon_6 \end{bmatrix}; \quad (2.13)$$

$$c_{44} = \frac{1}{2}(c_{11} - c_{12});$$

which has only two independent constants. By introducing new constants

$$\lambda = c_{11} - 2c_{44}; \quad \mu = c_{44}, \quad (2.14)$$

and returning back to the double index notation, the equation (2.13) can be rewritten as

$$\sigma_{ij} = 2\mu\varepsilon_{ij} + \lambda\varepsilon_{kk}\delta_{ij}. \quad (2.15)$$

The constants λ and μ are called *Lamé constants*. The relations between the Lamé constants and more commonly used elastic constants are

$$E = \frac{\mu(3\lambda + 2\mu)}{\lambda + \mu} \quad \text{Young's modulus} \quad (2.16)$$

$$G = \mu \quad \text{Shear modulus} \quad (2.17)$$

$$\nu = \frac{\lambda(\lambda + \mu)}{2} \quad \text{Poisson ratio} \quad (2.18)$$

$$k = \frac{E}{3(1 - 2\nu)} \quad \text{Bulk modulus} \quad (2.19)$$

Equations (2.1), (2.2), (2.4), and (2.15) are the basic equations of linear elasticity. After expanding the indices, they produce 15 equations with 15 unknowns

$$u_1, u_2, u_3, \sigma_1, \sigma_2, \sigma_3, \sigma_4, \sigma_5, \sigma_6, \varepsilon_1, \varepsilon_2, \varepsilon_3, \varepsilon_4, \varepsilon_5, \varepsilon_6. \quad (2.20)$$

which represent 3 displacements, 6 stresses and 6 strains. These equations can be combined and written as one set of equations. The resulting equations are known as *Navier's equations* for the displacements u_i over the range $i = 1, 2, 3$. To derive Navier's equations, we calculate $\partial\sigma_{ij}/\partial x_j$ in terms of the displacements u_i and substitute the results into the momentum equation (2.1).

Neglecting the body forces, we write the final form of Navier's equations in Cartesian coordinates

$$(\lambda + \mu)\frac{\partial^2 u_k}{\partial x_k \partial x_i} + \mu\frac{\partial^2 u_i}{\partial x_j^2} = \rho\ddot{u}_i, \quad i = 1, 2, 3; \quad (2.21)$$

In vector form these equations can be expressed as

$$(\lambda + \mu)\nabla(\nabla \cdot \mathbf{u}) + \mu\nabla^2\mathbf{u} = \rho\ddot{\mathbf{u}}. \quad (2.22)$$

This is the fundamental differential equation of three-dimensional elasticity.

Navier's equations can be simplified using the *Helmholtz decomposition theorem*, see for example [18]. By representing the displacement vector $\mathbf{u} = \mathbf{u}_l + \mathbf{u}_s$ as a combination of longitudinal ($\nabla \times \mathbf{u}_l = 0$) and shear ($\nabla \cdot \mathbf{u}_s = 0$) waves, we separate equation (2.22) into two independent ordinary *wave equations*:

$$\rho \frac{\partial^2 \mathbf{u}_l}{\partial t^2} - (\lambda + 2\mu)\nabla^2 \mathbf{u}_l = 0, \quad (2.23)$$

$$\rho \frac{\partial^2 \mathbf{u}_s}{\partial t^2} - \mu\nabla^2 \mathbf{u}_s = 0. \quad (2.24)$$

This may also be expressed in terms of *longitudinal* and *shear* (or *transversal*) velocities c_l and c_s

$$c_l = \sqrt{c_{11}/\rho} = \sqrt{(\lambda + 2\mu)/\rho}; \quad (2.25)$$

$$c_s = \sqrt{c_{44}/\rho} = \sqrt{\mu/\rho}. \quad (2.26)$$

Thus, our wave equations (2.23) and (2.24) may be rewritten

$$\frac{\partial^2 \mathbf{u}_l}{\partial t^2} - c_l^2 \nabla^2 \mathbf{u}_l = 0; \quad (2.27)$$

$$\frac{\partial^2 \mathbf{u}_s}{\partial t^2} - c_s^2 \nabla^2 \mathbf{u}_s = 0. \quad (2.28)$$

A well known plane harmonic wave solution for equations (2.27) and (2.28) can be presented in the form

$$\mathbf{u}(\mathbf{r}, t) = A\mathbf{p}e^{i(\mathbf{k}\cdot\mathbf{r} \mp \omega t)}, \quad (2.29)$$

where A is the amplitude, ω is the *angular frequency*, \mathbf{k} is the *wave vector*, and \mathbf{p} is the *polarization vector*. The negative sign corresponds to a wave travelling along the

\mathbf{k} vector, and the positive sign corresponds to the opposite travelling wave. For longitudinal waves, the polarization vector \mathbf{p} coincides with the direction of propagation, while for shear waves it lies in the plane perpendicular to the direction of propagation. Since the direction of wave propagation is determined by the wave vector \mathbf{k} , the following conditions are imposed on the polarization

$$\mathbf{p} \times \mathbf{k} = 0, \quad \text{for the longitudinal wave;} \quad (2.30)$$

$$\mathbf{p} \cdot \mathbf{k} = 0, \quad \text{for the shear wave.} \quad (2.31)$$

An alternative way of obtaining solutions for Navier's equations (2.22) involves using vector potentials. In this case, the displacement field \mathbf{u} is presented as

$$\mathbf{u} = \nabla\phi + \nabla \times \boldsymbol{\psi}; \quad (2.32)$$

where ϕ is the scalar part and $\boldsymbol{\psi}$ is a vector part of the vector potential. The wave equations in this case have the same form as equation (2.27) and equation (2.28)

$$\frac{\partial^2 \phi}{\partial t^2} - c_i^2 \nabla^2 \phi = 0; \quad (2.33)$$

$$\frac{\partial^2 \boldsymbol{\psi}}{\partial t^2} - c_s^2 \nabla^2 \boldsymbol{\psi} = 0. \quad (2.34)$$

Additional considerations are required when considering fluids instead of elastic solids. Generally, the accurate consideration of sound propagation in fluids should take into account the fluid viscosity. Therefore, the theory of wave propagation in fluids normally deals with velocities instead of displacements, and involves velocity strain tensors instead of displacement strain tensors, as in elastic solids. The corresponding equations of motion can be found in literature as Navier-Stokes-Duhem equations [17]. However, when considering an idealized model with no viscosity, the fluid behavior can be explained in the same terms as the behavior of an elastic solid with zero resistance

to shear strains. By setting $\mu = 0$, the stiffness tensor simplifies to

$$c_{ij} = \begin{bmatrix} \lambda & \lambda & \lambda & 0 & 0 & 0 \\ \lambda & \lambda & \lambda & 0 & 0 & 0 \\ \lambda & \lambda & \lambda & 0 & 0 & 0 \\ 0 & 0 & 0 & 0 & 0 & 0 \\ 0 & 0 & 0 & 0 & 0 & 0 \\ 0 & 0 & 0 & 0 & 0 & 0 \end{bmatrix}; \quad (2.35)$$

Therefore, from equation (2.15), the constitutive equations for an ideal fluid are

$$\sigma_{ij} = \lambda \varepsilon_{kk} \delta_{ij}. \quad (2.36)$$

The ε_{kk} factor has an explicit physical meaning. Let's express it through the particle displacement:

$$\varepsilon_{kk} = \frac{1}{2}(u_{k,k} + u_{k,k}) = u_{k,k} = \frac{\partial u_x}{\partial x} + \frac{\partial u_y}{\partial y} + \frac{\partial u_z}{\partial z}. \quad (2.37)$$

This is a relative change in an elementary volume, or *dilatation*. The product of the dilatation and λ , which in this case is known as the bulk modulus of a fluid, corresponds to the pressure inside the elementary volume:

$$p = -\lambda \varepsilon_{kk}; \quad (2.38)$$

where the negative sign reflects the fact that the pressure is proportional to the volume compression.

Similar to the elastic solid case, we obtain Navier's equations in Cartesian coordinates

$$\lambda u_{k,ki} = \rho \ddot{u}_i; \quad (2.39)$$

or in the vector form

$$\lambda \nabla^2 \mathbf{u} = \rho \ddot{\mathbf{u}}. \quad (2.40)$$

In terms of the sound velocity in a fluid, $c = \sqrt{\lambda/\rho}$, the three dimensional wave equations for a fluid have the same form as longitudinal wave equations for an elastic solid

$$\frac{\partial^2 \mathbf{u}}{\partial t^2} - c^2 \nabla^2 \mathbf{u} = 0, \quad \nabla \times \mathbf{u} = 0. \quad (2.41)$$

Similarly, we can obtain the wave equation for pressure

$$\frac{\partial^2 p}{\partial t^2} - c^2 \nabla^2 p = 0. \quad (2.42)$$

The harmonic plane wave solution for this equation has the same form as equation (2.29):

$$p(\mathbf{r}, t) = A e^{i(\mathbf{k} \cdot \mathbf{r} - \omega t)}. \quad (2.43)$$

As we can see, there are many similarities between the fluid and solid media. In fact, when the shear waves are unimportant, it is often convenient to consider the solid media as a fluid.

2.2 Reflection and Transmission

One of the important topics in studying wave propagation is the wave reflection and transmission at an interface between two different media. The most common approach to obtaining reflection and transmission relations involves specifying and applying boundary conditions at the interface. Here we consider a simplified case of a plain harmonic wave hitting a plain interface between two semi-infinite media. Solving the interface problem in this case implies obtaining angles and amplitudes of reflected and transmitted waves for a given amplitude and angle of the incident wave using specific boundary conditions, such as phase, displacement, and strain matching at the interface.

2.2.1 General Boundary Conditions

From the practical point of view, if the first medium is an elastic solid, it is convenient to consider the cases of incident longitudinal (P) and shear (S) waves separately. Furthermore, it is common to separate vertical (SV) and horizontal (SH) polarizations of the shear wave, which correspond to displacements parallel and perpendicular to the interface (figure 2.1).

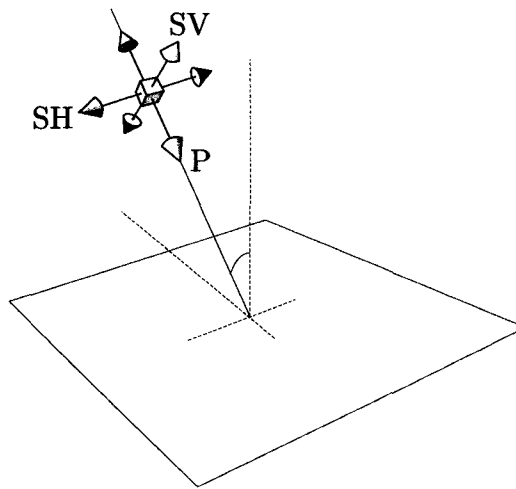


Figure 2.1. Polarization of the acoustic wave relative to the interface

Assume that medium 1 is in the half-space $z < 0$ and medium 2 is in the half-space $z > 0$. The coordinate system is chosen such that the wave vector of the incident wave lies in the xz plane perpendicular to the interface. For isotropic media, in such a coordinate system, the P and SV waves have displacement components in the same xz plane, while SH waves have displacements along the y axis. Since SH waves do not couple with either P or SV waves, the problem, therefore, can be solved separately for SH waves and combinations of P and SH waves.

Consider now the geometry shown in figure 2.2. The displacement vector \mathbf{u} , lying

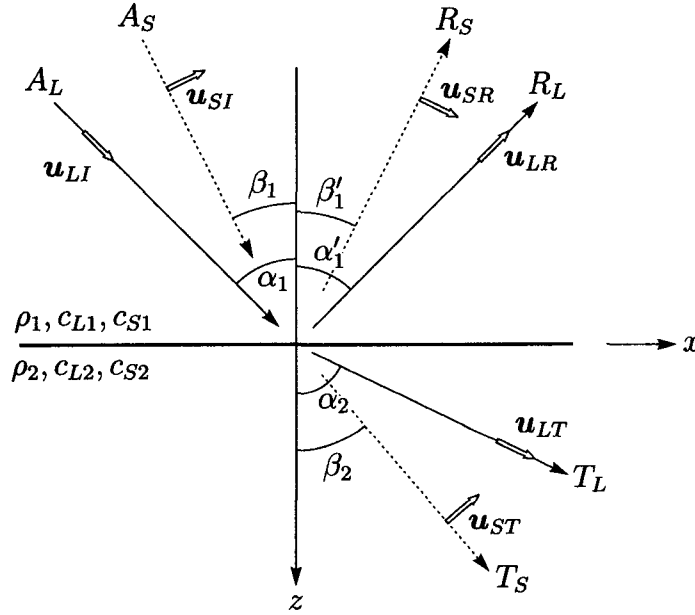


Figure 2.2. Reflection and transmission of a plane longitudinal and shear wave in general case

in the xz plane, can be represented as

$$\mathbf{u} = \begin{pmatrix} u_x \\ u_z \end{pmatrix}. \quad (2.44)$$

The wave displacements then can be written as

$$u_{LI} = A_L \begin{pmatrix} \sin \alpha_1 \\ \cos \alpha_1 \end{pmatrix} \exp[ik_{L1}(x \sin \alpha_1 + z \cos \alpha_1) - i\omega t]; \quad (2.45)$$

$$u_{SI} = A_S \begin{pmatrix} \cos \beta_1 \\ -\sin \beta_1 \end{pmatrix} \exp[ik_{S1}(x \sin \beta_1 + z \cos \beta_1) - i\omega t]; \quad (2.46)$$

$$u_{LR} = R_L \begin{pmatrix} \sin \alpha'_1 \\ -\cos \alpha'_1 \end{pmatrix} \exp[ik_{L1}(x \sin \alpha'_1 - z \cos \alpha'_1) - i\omega t]; \quad (2.47)$$

$$u_{SR} = R_S \begin{pmatrix} \cos \beta'_1 \\ \sin \beta'_1 \end{pmatrix} \exp[ik_{S1}(x \sin \beta'_1 - z \cos \beta'_1) - i\omega t]; \quad (2.48)$$

$$u_{LT} = T_L \begin{pmatrix} \sin \alpha_2 \\ \cos \alpha_2 \end{pmatrix} \exp[ik_{L2}(x \sin \alpha_2 + z \cos \alpha_2) - i\omega t]; \quad (2.49)$$

$$u_{ST} = T_S \begin{pmatrix} \cos \beta_2 \\ -\sin \beta_2 \end{pmatrix} \exp[ik_{S2}(x \sin \beta_2 + z \cos \beta_2) - i\omega t]. \quad (2.50)$$

Recall the stress-strain relations from the previous chapter. In our two-dimensional coordinate system, the strain tensor (2.4) has the following components:

$$\varepsilon_{xx} = \frac{\partial u_x}{\partial x}, \quad (2.51)$$

$$\varepsilon_{zz} = \frac{\partial u_z}{\partial z}, \quad (2.52)$$

$$\varepsilon_{xz} = \frac{1}{2} \left(\frac{\partial u_x}{\partial z} + \frac{\partial u_z}{\partial x} \right); \quad (2.53)$$

and the corresponding stress-strain relationship (2.15) can be rewritten as

$$\sigma_{zz} = 2\mu\varepsilon_{zz} + \lambda(\varepsilon_{xx} + \varepsilon_{zz}) = 2\mu \frac{\partial u_z}{\partial z} + \lambda \left(\frac{\partial u_x}{\partial x} + \frac{\partial u_z}{\partial z} \right); \quad (2.54)$$

$$\sigma_{xz} = 2\mu\varepsilon_{xz} = \mu \left(\frac{\partial u_x}{\partial z} + \frac{\partial u_z}{\partial x} \right). \quad (2.55)$$

By differentiating wave displacements, we obtain expressions for normal and tangential strains:

$$\begin{pmatrix} \sigma_{xz}^{LI} \\ \sigma_{zz}^{LI} \end{pmatrix} = A_L ik_{L1} \begin{pmatrix} \mu_1 \sin 2\alpha_1 \\ 2\mu_1 \cos^2 \alpha_1 + \lambda_1 \end{pmatrix} \exp[\dots]; \quad (2.56)$$

$$\begin{pmatrix} \sigma_{xz}^{SI} \\ \sigma_{zz}^{SI} \end{pmatrix} = A_S ik_{S1} \begin{pmatrix} \mu_1 \cos 2\beta_1 \\ -\mu_1 \sin 2\beta_1 \end{pmatrix} \exp[\dots]; \quad (2.57)$$

$$\begin{pmatrix} \sigma_{xz}^{LR} \\ \sigma_{zz}^{LR} \end{pmatrix} = R_L ik_{L1} \begin{pmatrix} -\mu_1 \sin 2\alpha'_1 \\ 2\mu_1 \cos^2 \alpha'_1 + \lambda_1 \end{pmatrix} \exp[\dots]; \quad (2.58)$$

$$\begin{pmatrix} \sigma_{xz}^{SR} \\ \sigma_{zz}^{SR} \end{pmatrix} = R_S ik_{S1} \begin{pmatrix} -\mu_1 \cos 2\beta'_1 \\ -\mu_1 \sin 2\beta'_1 \end{pmatrix} \exp[\dots]; \quad (2.59)$$

$$\begin{pmatrix} \sigma_{xz}^{LT} \\ \sigma_{zz}^{LT} \end{pmatrix} = T_L ik_{L2} \begin{pmatrix} \mu_2 \sin 2\alpha_2 \\ 2\mu_2 \cos^2 \alpha_2 + \lambda_2 \end{pmatrix} \exp[\dots]; \quad (2.60)$$

$$\begin{pmatrix} \sigma_{xz}^{ST} \\ \sigma_{zz}^{ST} \end{pmatrix} = T_S ik_{S2} \begin{pmatrix} \mu_2 \cos 2\beta_2 \\ -\mu_2 \sin 2\beta_2 \end{pmatrix} \exp[\dots]; \quad (2.61)$$

where the $\exp[\dots]$ expression is the same as for the displacements.

The phase matching conditions force the k projection on the z -axis to be constant, which leads to *Snell's law*

$$\frac{\sin \alpha_1}{c_{L1}} = \frac{\sin \alpha'_1}{c_{L1}} = \frac{\sin \alpha_2}{c_{L2}} = \frac{\sin \beta_1}{c_{S1}} = \frac{\sin \beta'_1}{c_{S1}} = \frac{\sin \beta_2}{c_{S2}}; \quad (2.62)$$

Snell's law, in turn, defines angles for reflected and transmitted waves.

Using Snell's law we may further simplify the strain equations using the identity

$$2\mu \cos^2 \alpha + \lambda = (\lambda + 2\mu) \cos 2\beta; \quad (2.63)$$

where α corresponds to the longitudinal wave and β corresponds to the shear wave.

Consider now the phase factor

$$\exp[ik(x \sin \alpha \pm z \cos \alpha) - i\omega t]. \quad (2.64)$$

After applying Snell's law, the phase factor at the interface ($z = 0$) becomes the same for all types of waves. It is possible to get rid of it just by choosing an appropriate time and x coordinate.

Recall also that the Lamé coefficients in terms of longitudinal (c_L) and shear (c_S) velocities are

$$\lambda + 2\mu = \rho c_L^2, \quad \mu = \rho c_S^2. \quad (2.65)$$

To further simplify the equations, we introduce the *acoustic impedance*

$$Z = \rho c \quad (2.66)$$

Let's rewrite the expressions for strains taking into account (2.62) and (2.63), and

assuming the phase exponent equals 1:

$$\begin{aligned}\sigma_{xz}^{LI} &= i\omega A_L Z_{S1} \cdot 2 \cos \alpha_1 \sin \beta_1; & \sigma_{zz}^{LI} &= i\omega A_L Z_{L1} \cos 2\beta_1; \\ \sigma_{xz}^{SI} &= i\omega A_S Z_{S1} \cos 2\beta_1; & \sigma_{zz}^{SI} &= -i\omega A_S Z_{S1} \sin 2\beta_1;\end{aligned}\quad (2.67)$$

$$\begin{aligned}\sigma_{xz}^{LR} &= -i\omega R_L Z_{S1} \cdot 2 \cos \alpha_1 \sin \beta_1; & \sigma_{zz}^{LR} &= i\omega R_L Z_{L1} \cos 2\beta_1; \\ \sigma_{xz}^{SR} &= -i\omega R_S Z_{S1} \cos 2\beta_1; & \sigma_{zz}^{SR} &= -i\omega R_S Z_{S1} \sin 2\beta_1;\end{aligned}\quad (2.68)$$

$$\begin{aligned}\sigma_{xz}^{LT} &= i\omega T_L Z_{S2} \cdot 2 \cos \alpha_2 \sin \beta_2; & \sigma_{zz}^{LT} &= i\omega T_L Z_{L2} \cos 2\beta_2; \\ \sigma_{xz}^{ST} &= i\omega T_S Z_{S2} \cos 2\beta_2; & \sigma_{zz}^{ST} &= -i\omega T_S Z_{S2} \sin 2\beta_2;\end{aligned}\quad (2.69)$$

These expressions, together with the expressions for displacements (similarly assuming the exponent to be 1), form the basis for studying reflection and propagation at different types of interface.

2.2.2 Reflection and Transmission at a Solid-Solid Interface

The interface problem for a boundary between two elastic solids is strongly influenced by physical conditions at the interface. Normally these conditions may vary from a welded contact to a smooth contact. For the case of the welded contact, the normal and tangential components of displacements and stresses are the same at $z = 0$ from both sides of the interface. For the smooth contact, also referred to as a slipping contact, only the normal components of displacements are preserved and the shear stress is assumed to vanish at the interface. Physically the smooth contact can be described as two solids separated by a negligibly thin liquid coupling, which does not transfer the shear stresses.

Together with Snell's law, the physical conditions at the interface form the full

description of the boundary problem, permitting the calculation of the angles and amplitudes of the reflected and transmitted waves.

Physical boundary conditions for the welded contact are that the displacements and stresses are continuous across the interface:

$$\begin{aligned} \sum u_z^{(1)} &= \sum u_z^{(2)}; & \sum u_x^{(1)} &= \sum u_x^{(2)}; \\ \sum \sigma_{zz}^{(1)} &= \sum \sigma_{zz}^{(2)}; & \sum \sigma_{xz}^{(1)} &= \sum \sigma_{xz}^{(2)}; \end{aligned} \quad (2.70)$$

or, expressed in matrix form,

$$\mathbf{a} = M\mathbf{d}; \quad \mathbf{a} = \begin{bmatrix} U_z^I \\ U_x^I \\ \sigma_{zz}^I \\ \sigma_{xz}^I \end{bmatrix}; \quad \mathbf{d} = \begin{bmatrix} R_L \\ R_S \\ T_L \\ T_S \end{bmatrix}; \quad (2.71)$$

$$M = \begin{bmatrix} -\cos \alpha_1 & \sin \beta_1 & \cos \alpha_2 & -\sin \beta_2 \\ \sin \alpha_1 & \cos \beta_1 & \sin \alpha_2 & \cos \beta_2 \\ Z_{L1} \cos 2\beta_1 & -Z_{S1} \sin 2\beta_1 & Z_{L2} \cos 2\beta_2 & -Z_{S2} \sin 2\beta_2 \\ -2Z_{S1} \cos \alpha_1 \sin \beta_1 & -Z_{S1} \cos 2\beta_1 & 2Z_{S2} \cos \alpha_2 \sin \beta_2 & Z_{S2} \cos 2\beta_2 \end{bmatrix}; \quad (2.72)$$

where \mathbf{d} holds reflection and transmission amplitudes. The components of \mathbf{a} are the normal and tangential amplitudes (U_z^I and U_x^I) and the normal and tangential stresses (σ_{zz}^I and σ_{xz}^I) for the incident wave. Generally, these amplitudes and stresses are linear combinations of the corresponding amplitudes and stresses for longitudinal and shear waves. Since the system is linear, the longitudinal and shear waves can be considered independently:

$$\mathbf{a} = A_L \begin{bmatrix} \cos \alpha_1 \\ \sin \alpha_1 \\ Z_{L1} \cos 2\beta_1 \\ 2Z_{S1} \cos \alpha_1 \sin \beta_1 \end{bmatrix}, \quad \text{for P wave input,}$$

and

$$\mathbf{a} = A_S \begin{bmatrix} -\sin \beta_1 \\ \cos \beta_1 \\ -Z_{S1} \sin 2\beta_1 \\ Z_{S1} \cos 2\beta_1 \end{bmatrix}, \quad \text{for SV wave input.}$$

By setting the amplitude of the incident wave as $A_L = 1$ or $A_S = 1$, and solving this linear system of equations, we obtain reflection and transmission factors corresponding to incident longitudinal or shear wave polarizations correspondingly.

The physical boundary conditions for the smooth contact are that normal components of displacements and stresses are continuous across the interface, while the tangential stresses vanish:

$$\begin{aligned} \sum u_z^{(1)} &= \sum u_z^{(2)}; & \sum \sigma_{zz}^{(1)} &= \sum \sigma_{zz}^{(2)}; \\ \sum \sigma_{xz}^{(1)} &= 0; & \sum \sigma_{xz}^{(2)} &= 0; \end{aligned} \quad (2.73)$$

or, in matrix form,

$$M = \begin{bmatrix} -\cos \alpha_1 & \sin \beta_1 & \cos \alpha_2 & -\sin \beta_2 \\ Z_{L1} \cos 2\beta_1 & -Z_{S1} \sin 2\beta_1 & Z_{L2} \cos 2\beta_2 & -Z_{S2} \sin 2\beta_2 \\ -2Z_{S1} \cos \alpha_1 \sin \beta_1 & -Z_{S1} \cos 2\beta_1 & 0 & 0 \\ 0 & 0 & 2Z_{S2} \cos \alpha_2 \sin \beta_2 & Z_{S2} \cos 2\beta_2 \end{bmatrix} \quad (2.74)$$

where

$$\mathbf{a} = A_L \begin{bmatrix} \cos \alpha_1 \\ Z_{L1} \cos 2\beta_1 \\ Z_{S1} \sin 2\alpha_1 \\ 0 \end{bmatrix}, \quad \text{for P wave input,}$$

and

$$\mathbf{b} = A_S \begin{bmatrix} -\sin \beta_1 \\ -Z_{S1} \sin 2\beta_1 \\ Z_{S1} \cos 2\beta_1 \\ 0 \end{bmatrix}, \quad \text{for SV wave input.}$$

Similar to welded contacts, reflection and transmission factors are obtained by solving this system.

The factors obtained relate the *displacement* amplitudes. In the literature it is possible to find alternative approaches, where instead of displacement amplitudes authors obtain transmission and reflection factors in terms of particle velocities [2], strains and pressures, field potentials [1], etc.

Note that the displacement amplitude is related to strain as

$$\sigma_{nn} = ik_L(\lambda + 2\mu)U_L, \quad \text{for longitudinal waves;} \quad (2.75)$$

$$\sigma_{nt} = ik_S\mu U_S, \quad \text{for shear waves;} \quad (2.76)$$

where U_L and U_S are the displacement amplitudes; σ_{nn} and σ_{nt} are, respectively, the strain components along, and perpendicular to the direction of propagation. Therefore, conversion of displacement factors to pressure/strain factors is a very simple procedure:

$$T^{(P)} = \frac{\sigma_2}{\sigma_1} = \frac{Z_2 U_2}{Z_1 U_1} = \frac{Z_2}{Z_1} T \quad (2.77)$$

Recall also that pressure in fluids corresponds to a negative longitudinal strain in solids. For different combinations of solids and fluids, one of the following equations is valid:

$$T^{(P)} = \frac{\sigma_2}{\sigma_1} = \frac{p_2}{p_1} = \frac{-\sigma_2}{p_1} = \frac{p_2}{-\sigma_1}. \quad (2.78)$$

Similarly, we define transmission and reflection factors in terms of energies. For a harmonic wave, the intensity is given by

$$I_L = \frac{\rho c_L \omega^2 U_L^2}{2} = \frac{\sigma_{nn}^2}{2\rho c_L}, \quad \text{for longitudinal waves;} \quad (2.79)$$

$$I_S = \frac{\rho c_S \omega^2 U_S^2}{2} = \frac{\sigma_{nt}^2}{2\rho c_S}, \quad \text{for shear waves;} \quad (2.80)$$

which leads to intensity reflection and transmission factors:

$$T^{(I)} = \frac{I_2}{I_1} = \frac{Z_2}{Z_1} T^2 = \frac{Z_1}{Z_2} T^{(P)2}. \quad (2.81)$$

To determine how the energy of an incident wave is partitioned at the interface, we introduce *normalized intensity*, which corresponds to the averaged energy flux delivered across the interface

$$I^* = I(\mathbf{k} \cdot \mathbf{n})/k = I \cos(\theta); \quad (2.82)$$

where \mathbf{n} is the interface normal; θ is the angle of incidence. Therefore, in terms of normalized intensities, the reflection and transmission angles, can be expressed as

$$T^{(*)} = \frac{I_2 \cos \theta_2}{I_1 \cos \theta_1} = \frac{Z_2 \cos \theta_2}{Z_1 \cos \theta_1} T^2. \quad (2.83)$$

An important consequence of the energy conservation law is that the normalized intensities sum up to the normalized intensity of the incident wave; or in terms of reflection and transmission factors

$$1 = \Sigma R^{(*)} + \Sigma T^{(*)}; \quad (2.84)$$

where $R^{(*)}$ and $T^{(*)}$ are the reflection and transmission factors expressed in terms of normalized intensities.

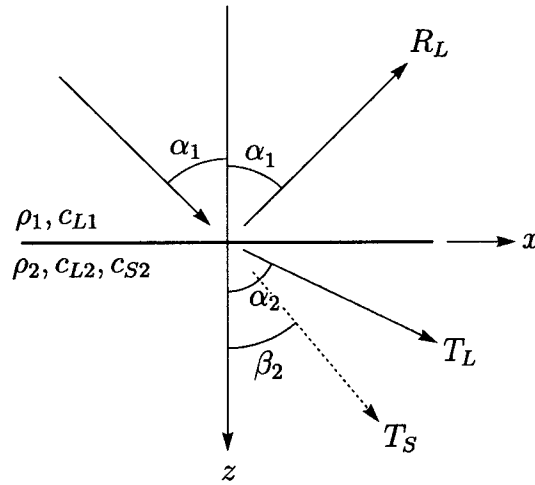


Figure 2.3. Reflection and transmission of a plane longitudinal wave at a fluid-solid interface

2.2.3 Reflection and Transmission at a Fluid→Solid Interface

Consider now a plane harmonic wave in a fluid hitting a plane fluid-solid interface, as shown in figure 2.3

There are no shear stresses in fluid media, and the boundary conditions are simplified:

$$\sum u_z^{(1)} = \sum u_z^{(2)}; \quad \sum \sigma_{zz}^{(1)} = \sum \sigma_{zz}^{(2)}; \quad \sum \sigma_{xz}^{(2)} = 0; \quad (2.85)$$

which requires only a 3×3 scattering matrix:

$$\begin{bmatrix} \cos \alpha_1 \\ Z_{L1} \\ 0 \end{bmatrix} = \begin{bmatrix} -\cos \alpha_1 & \cos \alpha_2 & -\sin \beta_2 \\ Z_{L1} & Z_{L2} \cos 2\beta_2 & -Z_{S2} \sin 2\beta_2 \\ 0 & 2Z_{S2} \cos \alpha_2 \sin \beta_2 & Z_{S2} \cos 2\beta_2 \end{bmatrix} \begin{bmatrix} R_L \\ T_L \\ T_S \end{bmatrix} \quad (2.86)$$

Solving this system, we find the reflection and transmission factors:

$$\begin{aligned} R_L &= \frac{X_{L1} - Y}{X_{L1} + Y}; \\ T_L &= \frac{Z_{L1} 2X_{L2} \cos 2\beta_2}{Z_{L2} (X_{L1} + Y)}; \\ T_S &= -\frac{Z_{L1} 2X_{S2} \sin 2\beta_2}{Z_{S2} (X_{L1} + Y)}; \end{aligned} \quad (2.87)$$

where

$$\begin{aligned} X_{L1} &= \frac{Z_{L1}}{\cos \alpha_1}; & X_{L2} &= \frac{Z_{L2}}{\cos \alpha_2}; & X_{S2} &= \frac{Z_{S2}}{\cos \beta_2}; \\ Y &= X_{L2} \cos^2 2\beta_2 + X_{S2} \sin^2 2\beta_2. \end{aligned}$$

The X -parameter is often referred to as the *normal acoustic impedance*:

$$X = \frac{Z}{\cos \theta} = \frac{\rho c}{\cos \theta}. \quad (2.88)$$

Note that the phase of the reflected wave can change depending on material properties or wave angles.

2.2.4 Longitudinal Wave Incidence on a Solid→Fluid Interface

Consider an incident P wave hitting a solid-fluid interface (figure 2.4). In this case, the boundary conditions are

$$\sum u_z^{(1)} = \sum u_z^{(2)}; \quad \sum \sigma_{zz}^{(1)} = \sum \sigma_{zz}^{(2)}; \quad \sum \sigma_{xz}^{(1)} = 0; \quad (2.89)$$

This again results in a 3×3 matrix:

$$\begin{bmatrix} \cos \alpha_1 \\ Z_{L1} \cos 2\beta_1 \\ 2Z_{S1} \cos \alpha_1 \sin \beta_1 \end{bmatrix} = \begin{bmatrix} -\cos \alpha_1 & \sin \beta_1 & \cos \alpha_2 \\ Z_{L1} \cos 2\beta_1 & -Z_{S1} \sin 2\beta_1 & Z_{L2} \\ -2Z_{S1} \cos \alpha_1 \sin \beta_1 & -Z_{S1} \cos 2\beta_1 & 0 \end{bmatrix} \begin{bmatrix} R_L \\ R_S \\ T_L \end{bmatrix} \quad (2.90)$$

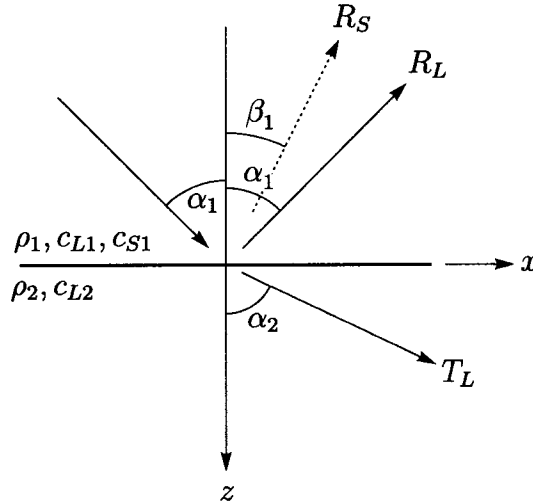


Figure 2.4. Reflection and transmission of a plane longitudinal wave at a solid-fluid interface

Solving this system, we obtain the corresponding transmission and reflection factors:

$$\begin{aligned}
 R_L &= \frac{X_{L1} \cos^2 2\beta_1 - Y}{X_{L1} \cos^2 2\beta_1 + Y}; \\
 R_S &= -\frac{Z_{L1}}{Z_{S1}} \cdot \frac{2X_{S1} \sin 2\beta_1 \cos 2\beta_1}{X_{L1} \cos^2 2\beta_1 + Y}; \\
 T_L &= \frac{Z_{L1}}{Z_{L2}} \cdot \frac{2X_{L2} \cos 2\beta_1}{X_{L1} \cos^2 2\beta_1 + Y}
 \end{aligned} \tag{2.91}$$

where

$$Y = X_{S1} \sin^2 2\beta_1 + X_{L2};$$

2.2.5 Shear (SV) Wave Incidence on a Solid→Fluid Interface

The case of a vertically polarized incident shear wave hitting a solid-fluid interface (figure 2.5) is in many ways similar to the longitudinal incoming wave, discussed in the previous section. The boundary conditions are the same, and so is the scattering matrix M . The only difference is in the input vector, which is determined by the displacements and stresses in the shear wave. Thus the boundary conditions can be

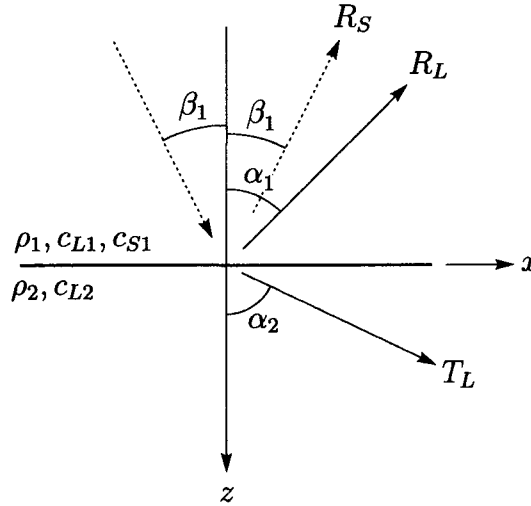


Figure 2.5. Reflection and transmission of a shear (SV) wave at a solid-fluid interface

written in matrix form as

$$\begin{bmatrix} -\sin \beta_1 \\ -Z_{S1} \sin 2\beta_1 \\ Z_{S1} \cos 2\beta_1 \end{bmatrix} = \begin{bmatrix} -\cos \alpha_1 & \sin \beta_1 & \cos \alpha_2 \\ Z_{L1} \cos 2\beta_1 & -Z_{S1} \sin 2\beta_1 & Z_{L2} \\ -2Z_{S1} \cos \alpha_1 \sin \beta_1 & -Z_{S1} \cos 2\beta_1 & 0 \end{bmatrix} \begin{bmatrix} R_L \\ R_S \\ T_L \end{bmatrix}. \quad (2.92)$$

The transmission and reflection factors in this case are

$$\begin{aligned} R_L &= -\frac{Z_{S1}}{Z_{L1}} \cdot \frac{2X_{L1} \sin 2\beta_1 \cos 2\beta_1}{X_{S1} \sin^2 2\beta_1 + Y}; \\ R_S &= \frac{X_{S1} \sin^2 2\beta_1 - Y}{X_{S1} \sin^2 2\beta_1 + Y}; \\ T_L &= -\frac{Z_{S1}}{Z_{L2}} \cdot \frac{2X_{L2} \sin 2\beta_1}{X_{S1} \sin^2 2\beta_1 + Y}; \end{aligned} \quad (2.93)$$

where

$$Y = X_{L2} + X_{L1} \cos^2 2\beta_1;$$

2.2.6 Reflection of a Shear (SH) Wave from an Interface

Finally, consider a horizontally polarized shear wave, travelling in an elastic solid, and incident on an interface. As mentioned earlier, there is no coupling of SH waves with either P or SV waves. For a welded contact, it is easy to show that the shear wave is transmitted and reflected similar to the pressure wave at a fluid-fluid interface. The corresponding reflection and transmission factors are

$$R^{SH} = \frac{X_1 - X_2}{X_1 + X_2}; \quad (2.94)$$

$$T^{SH} = \frac{2X_1}{X_1 + X_2}. \quad (2.95)$$

For an arbitrary angle of incidence, we separate the incoming wave into SV and SH polarized components. Since this is a simple geometric procedure, we just show the basic vector operations that can be used to split an arbitrary shear wave incident on an arbitrary oriented interface.

Let's define the interface as a plane in space

$$(\mathbf{x} - \mathbf{s}) \cdot \mathbf{n} = 0; \quad (2.96)$$

where \mathbf{n} is the surface normal and \mathbf{s} is an arbitrary point on the interface. Let the incident wave be determined by the wave vector \mathbf{k} and polarization vector \mathbf{p} , ($|\mathbf{p}| = 1$; $\mathbf{p} \cdot \mathbf{k} = 0$). The normal and tangential components of the wave vector are

$$\mathbf{k}_n = (\mathbf{k} \cdot \mathbf{n})\mathbf{n}; \quad \mathbf{k}_t = \mathbf{k} - \mathbf{k}_n. \quad (2.97)$$

The angle of incidence is

$$\theta = \arccos \left(\frac{|\mathbf{k}_n|}{|\mathbf{k}|} \right); \quad (2.98)$$

and the new coordinate system can be chosen as

$$\hat{\mathbf{e}}_1 = \frac{\mathbf{k}_t}{|\mathbf{k}_t|}; \quad \hat{\mathbf{e}}_2 = \mathbf{n} \times \hat{\mathbf{e}}_1; \quad \hat{\mathbf{e}}_3 = \mathbf{n}. \quad (2.99)$$

Contributions of SH and SV waves, correspondingly, are

$$A_{SH} = \mathbf{p} \cdot \hat{\mathbf{e}}_2; \quad A_{SV} = \sqrt{1 - A_{SH}^2}. \quad (2.100)$$

By solving the interface problem separately for SV and SH waves, for the general case, we obtain three solutions: a P wave and an SV wave corresponding to an incident SV wave, and a single SH wave, resulting from an incident SH wave. For the first two waves, the obtained reflected and refracted factors should be multiplied by the A_{SV} factor and for the SH wave—by the A_{SH} factor.

2.3 Attenuation

In previous chapters, only the propagation of sound in media without attenuation has been considered. In practice, however, the intensity of the wavefront diminishes as it progresses through the media. The list of physical effects involved in this process includes scattering, absorption, cavitation, and many others. Building a precise mathematical model including all the possible factors is impractical due to a large variety of physical phenomena and because of the statistical nature of attenuation. Fortunately, there exists a common empiric relation covering attenuation losses in the wave amplitude:

$$\frac{A_1}{A_0} = \exp[-\alpha \Delta z], \quad (2.101)$$

where α is an *attenuation factor* and Δz is the distance travelled.

It is common to measure the attenuation factor on a logarithmic scale to accommodate for a very wide range of amplitude ratios encountered in practice. Use of the logarithmic scale also allows addition of successive attenuations. One of the methods of representing the attenuation is a simple logarithm of the amplitude ratio. It gives

the attenuation measured in *nepers*:

$$\text{Attenuation} = \alpha \Delta z \text{ nepers.} \quad (2.102)$$

The attenuation factor α is therefore said to have units of nepers/meter.

A more commonly used logarithmic scale is based on the *decibel* (dB), where the attenuation over Δz distance is defined as:

$$\text{Attenuation} = 10 \log(\exp[-\alpha(f)\Delta z])^2 = 20(\log e)\alpha \Delta z \text{ dB.} \quad (2.103)$$

It is often convenient to subclass the attenuation into *scattering* and *absorption* losses. If attenuation is caused by scattering, the total energy of the ultrasonic wave is conserved. However, the energy flow is partially deflected from the wave path due to reflections and refractions on microstructural levels. For the case of multiple scattering, a ray of energy may eventually be returned back to the main beam. However, due to differences in path length travelled by the scattered component, the phase relations are affected. Additionally, some part of the energy can be converted to different wave modes. Absorption losses, on the other hand, are associated with material viscosity and similar effects, when part of the wave energy is transformed into other forms. Normally, absorption may adequately be described by introducing a viscous damping term. Commonly referred to as *material viscosity*, the attenuation often includes other effects which influence the wave propagation in a similar manner. For the absorption, the attenuation at room temperature is typically proportional to f^2 .

At room temperature, most single crystal materials have acoustic attenuations that increase with the square of the frequency. The physical mechanisms contributing to this viscous damping include the *thermoelastic mechanism* and the *Akhieser mechanism*. Thermoelastic attenuation is due to irreversible heat flow from compression regions to rarefaction regions. It occurs only in longitudinal waves, since shear waves

do not produce changes in size of the elementary volume elements. At finite temperatures in all materials there exists an equilibrium distribution of thermally-excited acoustic waves (phonons). Passage of a coherently-excited acoustic wave disturbs this phonon equilibrium, with a resulting energy absorption or damping. This mechanism is known as Akhieser (or phonon) damping. In metals the predominant damping mechanism depends upon the type of wave. Thermoelastic effects contribute about one half of the observed compressional wave attenuation and the remainder is explained by Akhieser damping. For shear waves, there is no thermoelastic damping and the Akhieser mechanism is believed to be the major contributor.

In noncrystalline materials, which consist of small, randomly oriented single crystal grains, the thermoelastic and Akhieser mechanisms do not display significant contribution up to several tenths of a gigahertz, and most of the attenuation is usually attributed to grain scattering. As a rule, there is a wide variety of experimental attenuation-frequency curves.

A multitude of other effects may contribute to attenuation, such as micro eddy currents, frictional losses in powder metal compactions, cavitation in liquids, interaction with conduction electrons in semiconductors, chemical reactions induced by passing of the ultrasonic waves, etc.

Material attenuation is usually considered together with the *dispersion* phenomena. In a common environment, the sound velocity does not depend of frequency until extremely high frequencies when, strictly speaking, the material should no longer be considered as continuous. However, for some materials, there exist exceptions. The anomalous dispersion, accompanied by the non-quadratic attenuation, can be caused by such phenomena as resonance excitation of internal degrees of freedom, or by mechanical relaxation. For more detailed information on attenuation and dispersion, see [3].

CHAPTER 3

Reflection and Refraction at Multiple Interfaces

In this chapter we discuss the process of propagation of a plane ultrasonic wave through multiple interfaces. A model for oblique incidence on the stack of tilted plain interfaces is considered. Results of numerical modeling for common materials are presented here, while the MathCAD source for these calculations can be found in Appendix A.

3.1 The Measurement Model

Some degree of understanding of wave propagation phenomena in real systems can be achieved by studying a simplified plane wave model. This can often be considered a good approximation when the wavelength is small compared to the transducer size. However, for matrix transducers, as well as for many other ultrasonic devices, this is not always the case. Therefore, diffraction phenomena should be combined with the results obtained here, which will be done in Chapter 5.

We start with specifying a model for studying reflection and refraction indices.

Material properties are chosen to be close to that in experimental setup to be able to compare the modeling approach with experimental data.

The model, sketched in figure 3.1, consists of three layers: polystyrene, ultrasonic gel, and the steel sample containing a defect. Ultrasonic parameters of these materials are presented in table Table 3.1.

Table 3.1. Mechanical properties of some materials

Material	Sound Velocity		Density	Impedance
	c_l , m/s	c_t , m/s	ρ , kg/m ³	Z , kg/m ² s $\times 10^6$
Water	1480	—	1000	1.48
Ultrasonic gel	1900	—	1300	2.47
Polystyrene	2400	1100	1050	2.52
Aluminum	6300	3100	2750	17.33
Steel	5900	3200	7900	46.61

Most of the numerical results are obtained for a steel sample. The reason for that is not only because it is a common material for NDE inspection, but also because mechanical properties of steel promote it close to the “worst case” scenario. Having one of the highest acoustic impedances amongst the constructional materials, steel represents a sufficient challenge, from both a modeling and experimental point of view. In modeling, for example, it narrows the scope of the paraxial approach; in experiment, it suppresses penetration of sound inside the sample by returning it back into immersion, which makes resulting signals extremely weak and sometimes hard to detect on the noisy background. Therefore, following success with steel, we can expect the same model to be applicable to materials with smaller impedances.

To simplify the problem, we consider it in two dimensions, that is only P (pressure)

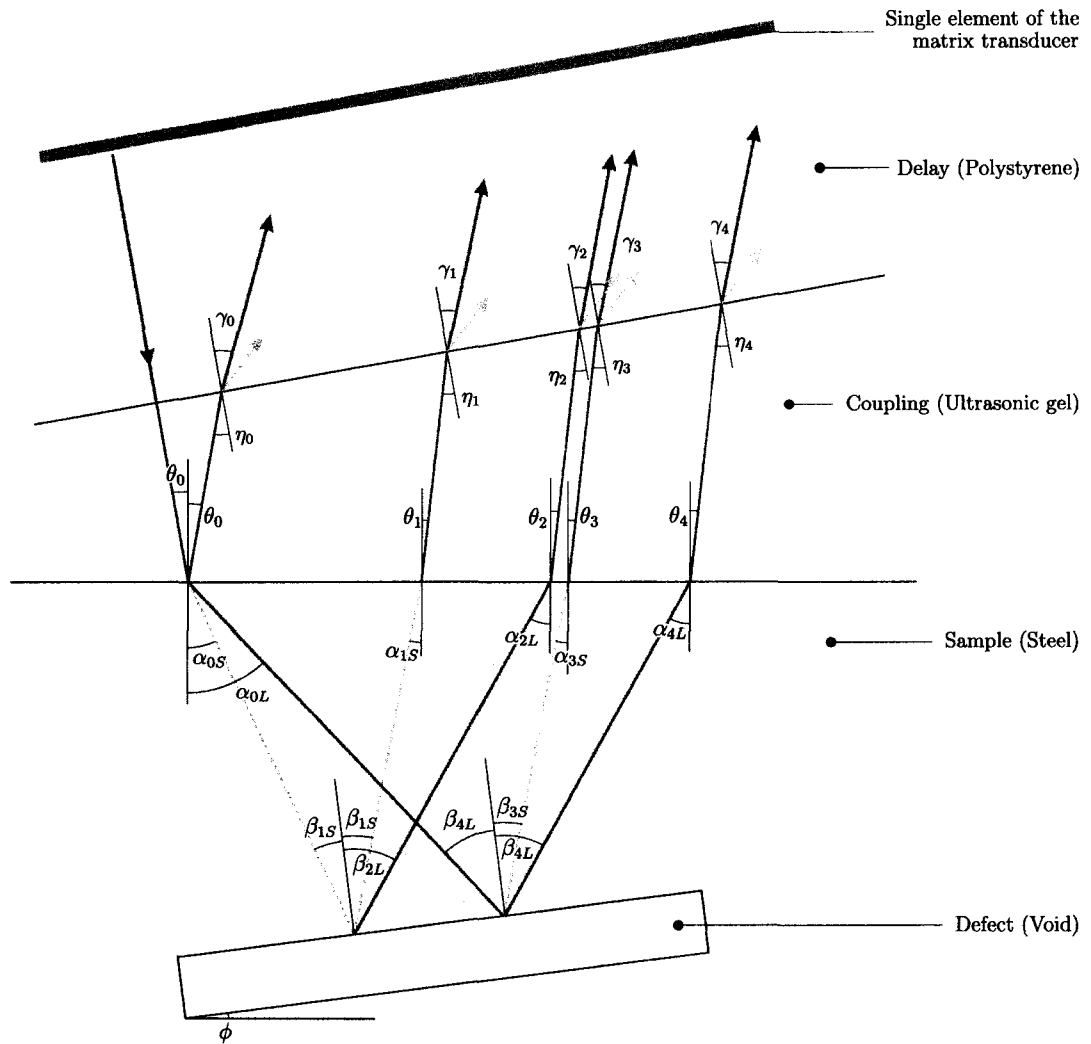


Figure 3.1. A simplified model of the measurement system. Red lines correspond to P-wave paths; blue lines correspond to SV-wave paths

and SV (vertically sheared) polarizations are involved. Both transducer and defect tilts are considered to be in the same plane (figure 3.1).

The longitudinal ultrasonic wave is generated in polystyrene by the transducer. The polystyrene delay is assumed to be flat-parallel, so that the initial wave has a normal collision with the first interface. The wave passes through ultrasonic gel, penetrates into the steel sample, reflects from the defect inside, and returns back passing through the same stack of materials. The defect is modelled as a plain interface with no material (or air) on the other side.

Throughout this chapter, we consider reflection and refraction factors at each interface. Then the obtained results are combined to obtain effective reflection factors for different wave paths within the system.

3.1.1 Reflection and Transmission at the Delay-Coupling Interface

According to the selected model, a forward propagating wave, travelling away from the transducer, undergoes a normal collision with the first interface. The matching of acoustic impedances for polystyrene and ultrasonic gel is so close, that according to equations (2.91), almost 100% of the energy is transmitted¹. In fact, even for 5° tilts, more than 99% of the energy is still transmitted, and for angles of up to 30° there is still more than 90% of the energy passing through the polystyrene-gel boundary (see figure 3.2). Therefore, small angles that may occur due to wearing of the delay line, or due to imperfections in delay manufacturing, should not change the general picture of wave propagation compared to that obtained for normal incidence.

For a backward propagating wave, travelling in the opposite direction, the angular

¹To convert amplitude reflection and transmission factors to normalized intensity factors, we use equation (2.83)

dependance of reflection and transmission factors can be obtained using (2.87). Results of numerical calculations are illustrated in figure 3.3 for normalized intensity factors. Notice that for the backward propagating wave, there exists a critical angle at 52° .

In this figure, as well as in many other figures throughout this chapter, the following notation is used:

- α_1, β_1 – angles for incident/reflected longitudinal and shear waves;
- α_2, β_2 – angles for transmitted longitudinal and shear waves;
- $R_L^{(*)}$, $R_S^{(*)}$, $T_L^{(*)}$, and $T_S^{(*)}$ – reflection (R) and transmission (T) factors in terms of normalized intensities for longitudinal (L) and shear (S) waves correspondingly.

3.1.2 Reflection and Transmission at the Coupling-Sample Interface

Consider now the immersion-sample boundary. Due to a large difference in impedances of ultrasonic gel and steel, only a small portion of the wave energy penetrates through this interface.

Reflection and transmission factors for the forward propagating wave are shown in figure 3.4. The first critical angle is at 18° ; above which only the shear polarization penetrates inside the sample. The second critical angle, at 36° , corresponds to the full reflection of both shear and longitudinal polarizations.

The energy participation for the backward propagating P-wave is shown in figure 3.5. Similarly, for the backward propagating SV-wave, transmission and reflection factors are shown in figure 3.6. A critical angle in this case is 33° .

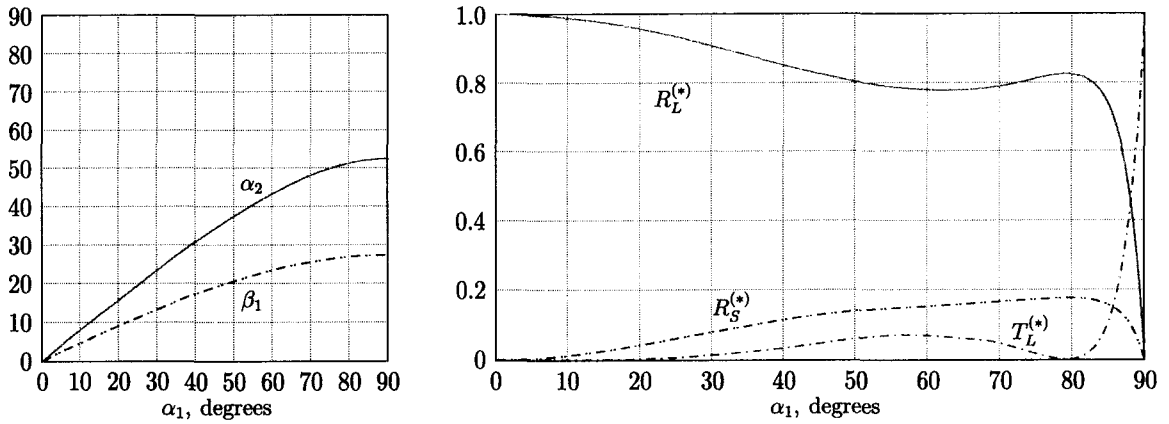


Figure 3.2. Reflection and transmission at the immersion–delay interface

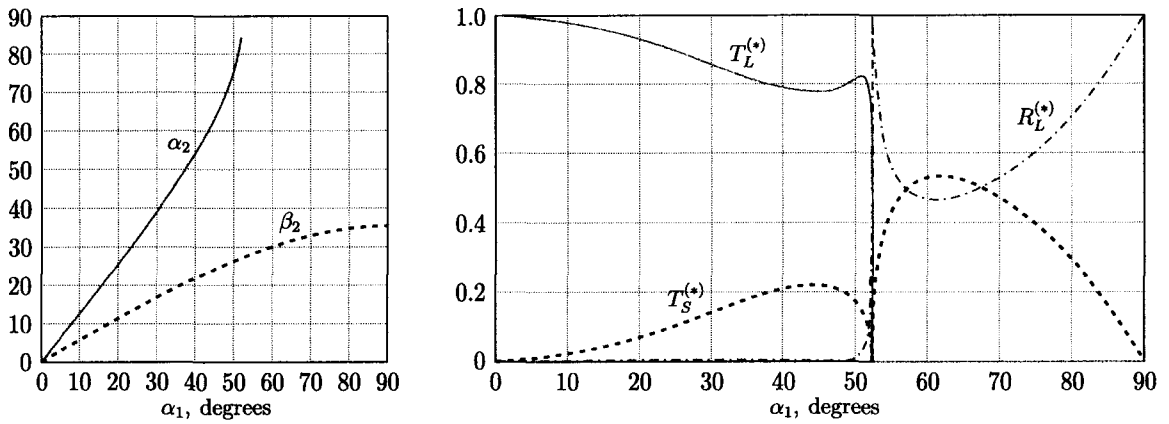


Figure 3.3. Reflection and transmission at the delay–immersion interface

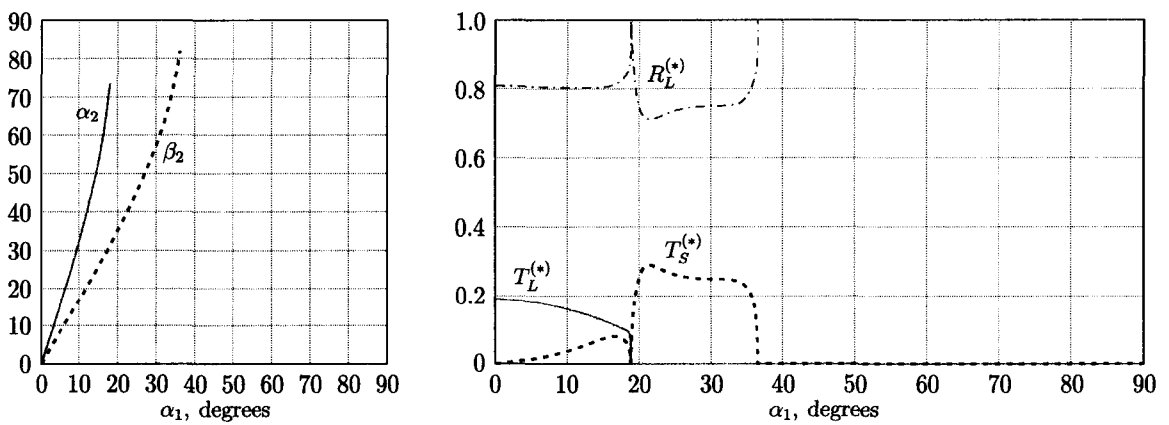


Figure 3.4. Reflection and transmission at the immersion–sample interface

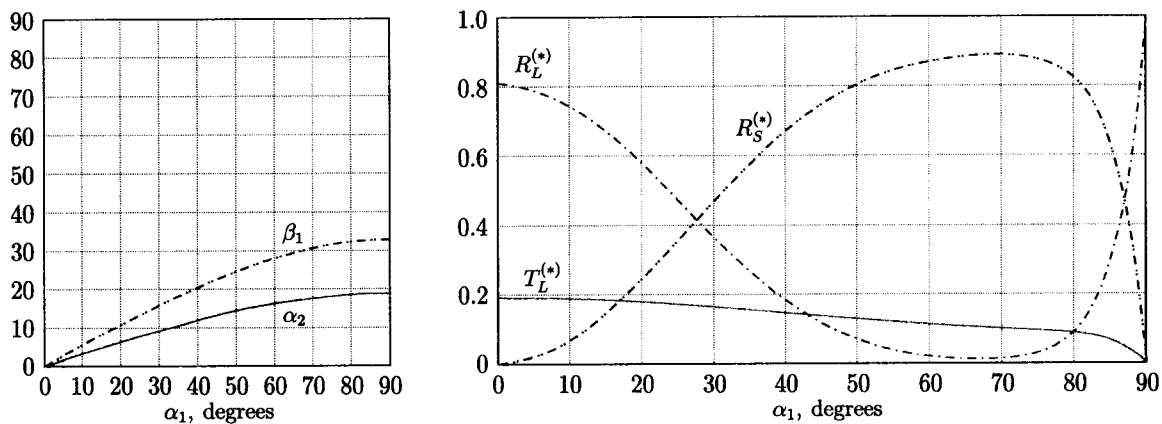


Figure 3.5. Reflection and transmission at the sample-immersion interface, P-wave incidence

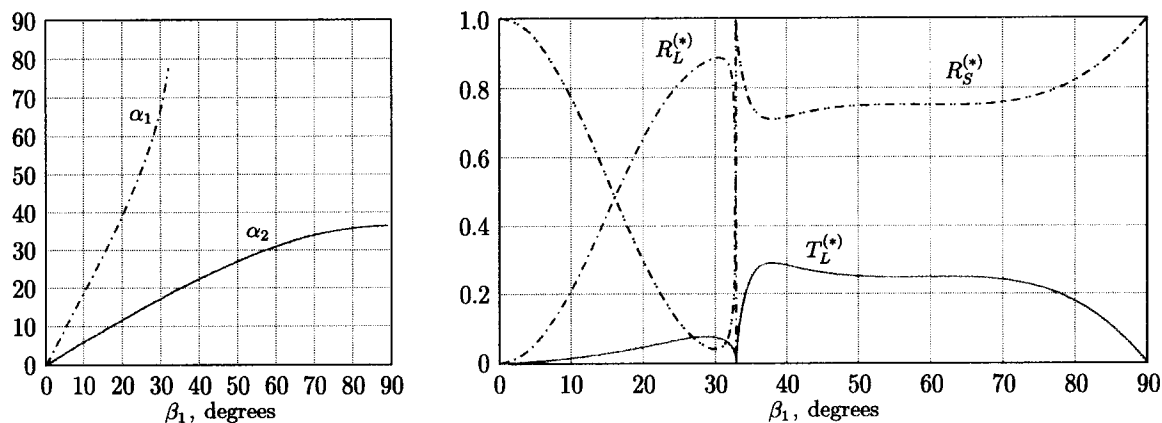


Figure 3.6. Reflection and transmission at the sample-immersion interface, SV-wave incidence

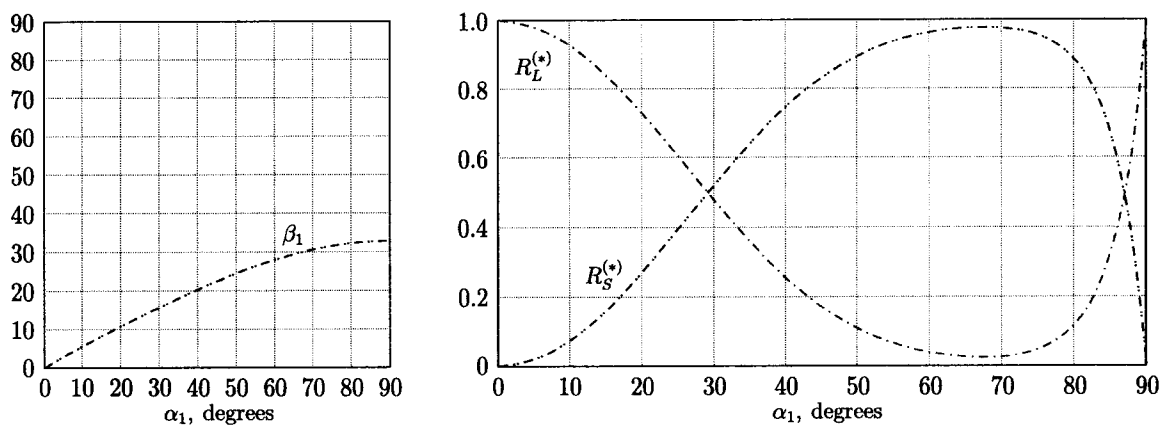


Figure 3.7. Reflection from the void defect, P-wave incidence

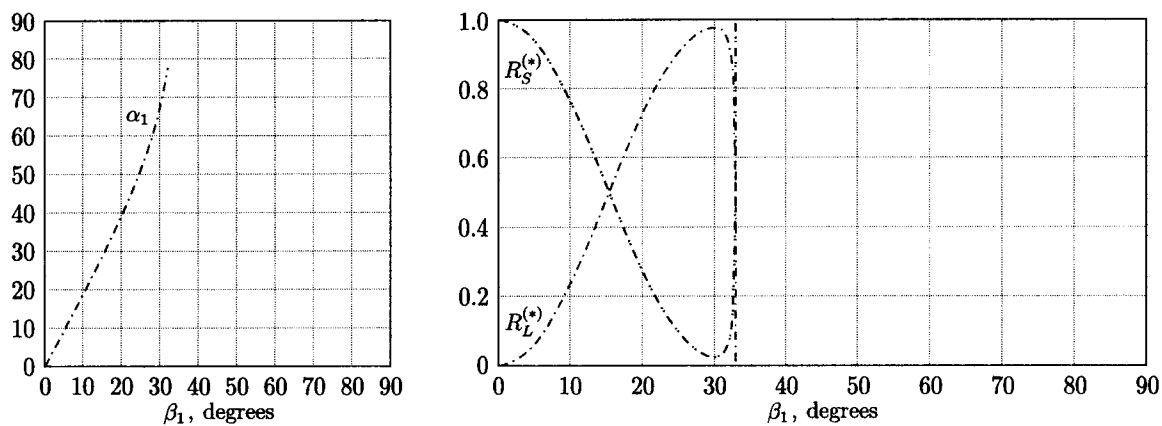


Figure 3.8. Reflection from the void defect, SV-wave incidence

3.1.3 Reflection from the Defect

We model the defect inside the sample as a flat void cavity, that is, all the incoming energy is reflected back. The angular dependence of reflection and transmission factors in this case is very similar to those at the sample-immersion interface, which can be explained by the big difference of impedances in both cases. For the incident longitudinal wave, the distribution is shown in figure 3.7. For the incident shear wave, the energy partition is shown in figure 3.8.

3.1.4 Combining Reflection and Transmission Factors

When the reflection and transmission factors have been determined at each interface, they can be combined to obtain effective reflection factors for the whole system. Consider the signal, reflected from the surface of the sample, and four different types of first-order reflections from the defect.

The existence of these four paths inside the sample is caused by the mode conversion at the front boundary of the sample and at the defect's boundary (figure 3.9). The main path, usually referred to as the LL-wave, does not include any mode conversion. LT- and TL-waves result from the consecutive mode transformation at front and back faces. The sound passes one way as a longitudinal wave and one way as a shear wave. Both LT- and TL-waves have very similar angles, phases and intensities, and it is usually impossible to separate them in the reflected signal. The last case for a TT-wave includes a double conversion of the wave mode at the front face of the sample, once when it enters the sample, and for the second time when it returns. The sound travels within the sample as a transverse wave in both directions.

The effective reflection factors and corresponding angles are denoted by (see also figure 3.1):

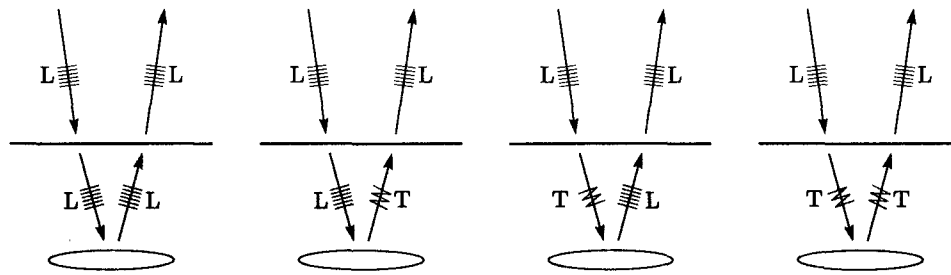


Figure 3.9. Conversion of wave modes inside the sample. L stands for a longitudinal pressure wave; T is a transversal SV wave

- R_0, γ_0 – reflection from the surface;
- R_1, γ_1 – TT-wave;
- R_2, γ_2 – TL-wave;
- R_3, γ_3 – LT-wave;
- R_4, γ_4 – LL-wave.

If the angle of the defect, relative to the sample's surface is $\phi = 0$, then all the angles of the reflected waves are the same. Figure 3.10 shows these angles and reflection factors as a function of the angle θ_0 between the transducer and the sample.

Note that the relative contribution of TT-, TL-, and LT-waves for flat-parallel defects is relatively small. Let's zoom into details of internal reflections and study the reflection angles and factors in more detail. The values of the reflection factors for the two values of $\phi = 0^\circ$ and $\phi = 10^\circ$ are shown in figures 3.11 and 3.12.

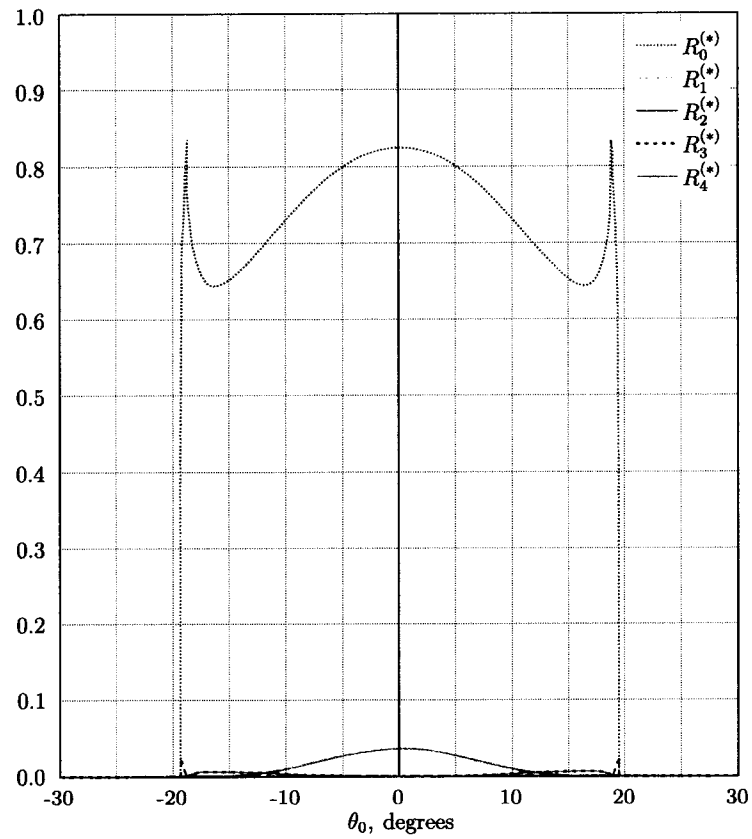
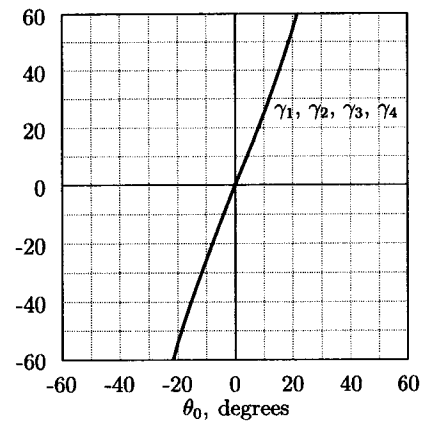


Figure 3.10. Effective reflection factors from a flat-parallel defect

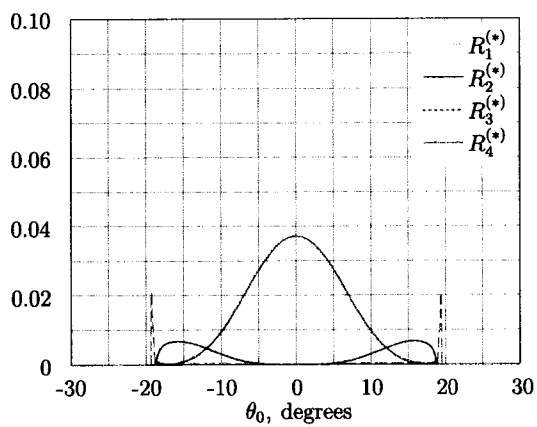


Figure 3.11. Effective angles and reflection factors, flat-parallel defect, $\phi = 0^\circ$

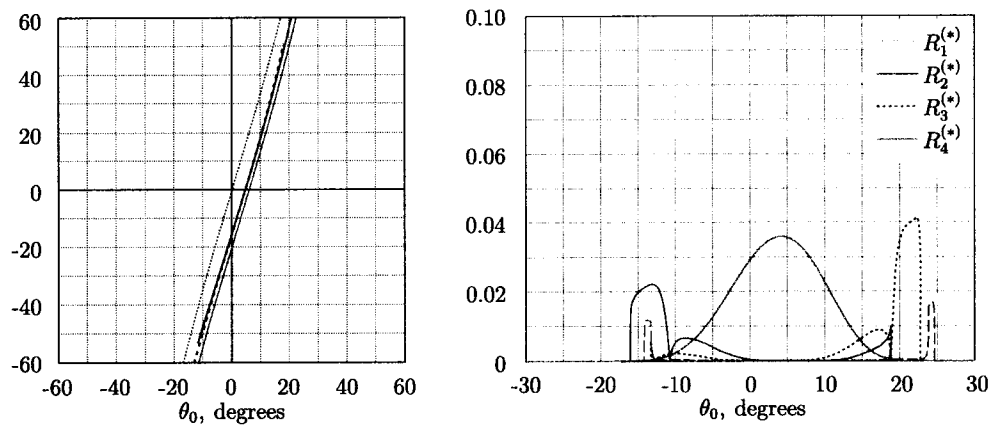


Figure 3.12. Effective angles and reflection factors, flat-parallel defect, $\phi = 10^\circ$

CHAPTER 4

Modeling Matrix Transducer Elements

An important part of any ultrasonic system is the *transducer*. This typically incorporates a piezoelectric element, which converts electrical signals into acoustic waves (transmit mode) and acoustic waves into electrical signals (receive mode).

The ultrasonic field generated by such a transducer is often the feature that determines the performance of the entire system. This is why the modeling of ultrasonic beam formation and propagation is important. Not only does it provide better understanding of physical processes which take place inside the system, but it also the optimization of the transducer design.

In this chapter attention is paid to modeling the field generated by a single planar transducer element. The results of this modeling are used later in Chapter 5, when the process of image formation is discussed.

4.1 The Piston Transducer Model

A common ultrasonic transducer radiates sound waves directly into an immersion liquid or hard delay line. Before reaching the area of interest inside the investigated sample, this beam transmits through one or more material boundaries. The structure of the field in such systems is extremely complex. With various types of surface, leaky and other waves being generated, building a precise mathematical model seems impossible. More importantly, it is not necessary from the practical point of view since the model can often be simplified down to a reasonable extent.

Before modeling the entire system, with all materials and interfaces, we first consider a simplified model of an ultrasonic transducer in a homogeneous medium. The most common approach for planar sound sources is the *piston transducer model*. The transducer is described as a finite region S in the x - y plane, surrounded by a motionless infinite boundary, as shown in figure 4.1. The velocity inside S is taken to be constant in space and directed along the z axis.

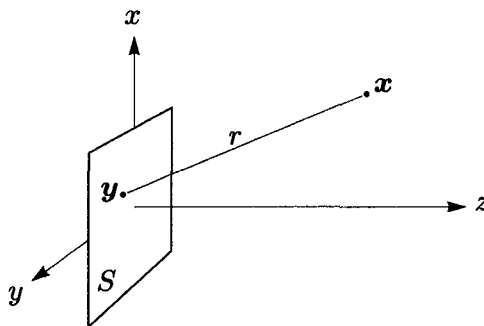


Figure 4.1. A planar piston transducer model

In transducer modeling, especially for the piston transducer model, it is common to treat the coupled media as a fluid, even when the transducer is coupled to the solid delay line. Indeed, the transducer primarily generates (and detects) longitudinal

waves, therefore neglecting the shear strength of the solid media seems reasonable. Moreover, as shown in [1], where a full elastic model for contact transducers is developed, this approximation does represent the transducer fields accurately. Shear waves, however, should be taken into account when considering beam propagation through interfaces. From the previous chapter, it follows that for specific geometries and relatively small angles, the shear component can be neglected. Based on this, we will treat *all* solid materials as equivalent fluids, thus operating on scalar pressures instead of stress tensors or displacement vectors.

Following the Huygens-Fresnel principle, the distribution of pressure in the uniform homogeneous half-space \mathbb{V} ($z \geq 0$) can be obtained using the *Rayleigh-Sommerfeld integral*

$$p(\mathbf{x}) = \frac{-i\omega\rho V_0}{2\pi} \iint_S \frac{e^{ikr}}{r} dS, \quad (4.1)$$

where V_0 is the velocity of the transducer surface, $\mathbf{x} \in \mathbb{V}$ is a point where the pressure is measured, and r is the distance from \mathbf{x} to a point \mathbf{y} inside S .

In figure 4.2, the results of numerical calculations are presented. These results are obtained for a 1×1 -mm transducer radiating at 15 MHz directly into polystyrene.

The field structure varies with changes in frequency, geometry or material parameters. However, the general picture remains similar to that shown in figure 4.2. There is a noticeable similarity in the field structure characteristic of circular transducers. First of all, it is easy to locate a near-field zone, with a series of amplitude oscillations. The last maximum, in our case located 2.2 mm along the central axis, is commonly referred to as a natural focus of a flat transducer—see figure 4.3. It separates near and far field zones. In the far field, the structure of the field no longer depends on the particular shape of the sound source, and the on-axis pressure curve approaches the one calculated for the circular transducer. In the far field, the amplitude of the ultrasonic

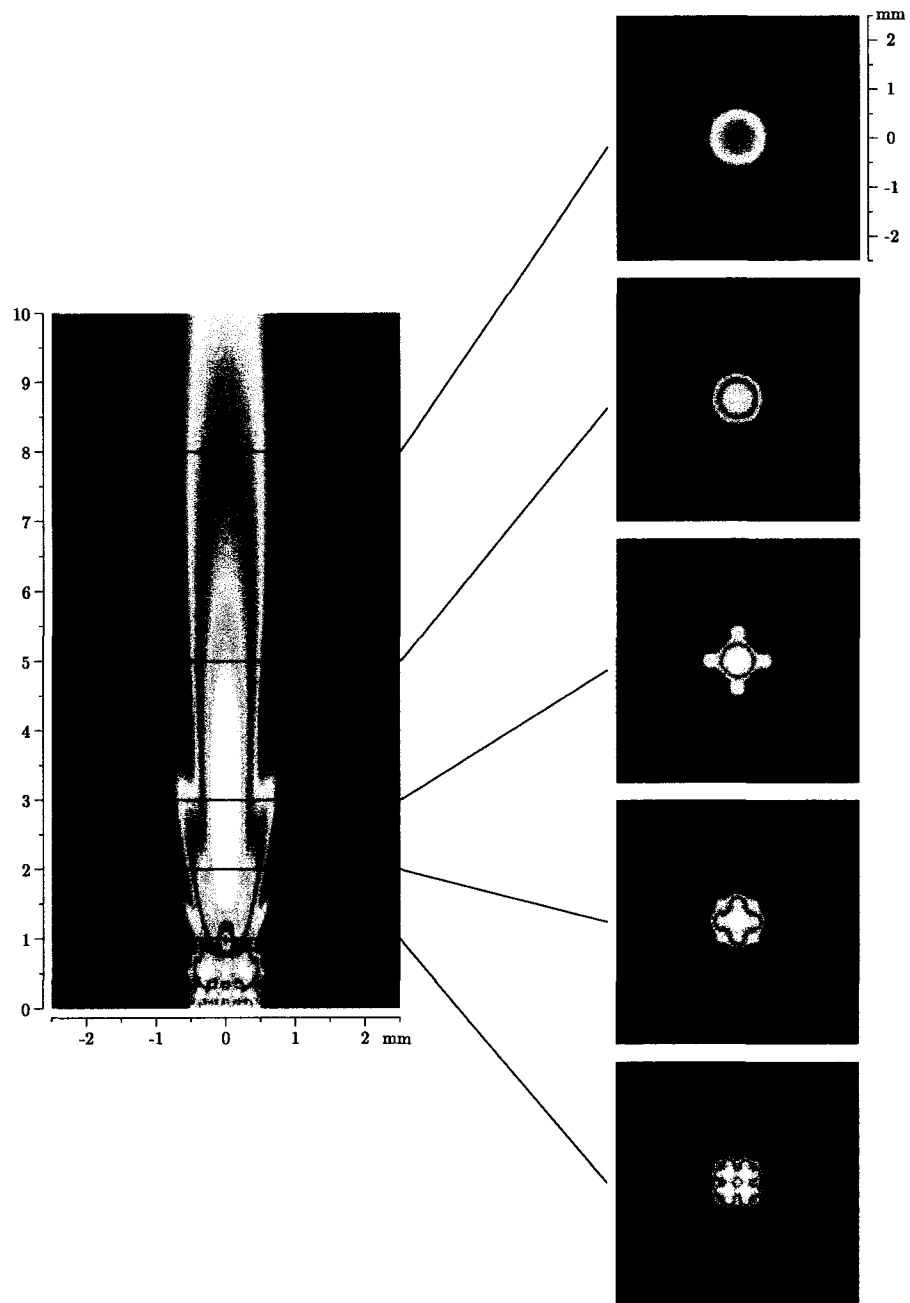


Figure 4.2. The amplitude of pressure distribution for a flat square transducer radiating directly into polystyrene. The results are obtained using direct numerical integration of the Rayleigh-Sommerfeld equation. Frequency: 15 MHz; transducer size: 1×1 mm, sound velocity: 2400 m/s

wave diminishes inversely proportionally to the square of the distance. The decrease in beam amplitude with distance is sometimes referred to as attenuation caused by beam spreading.

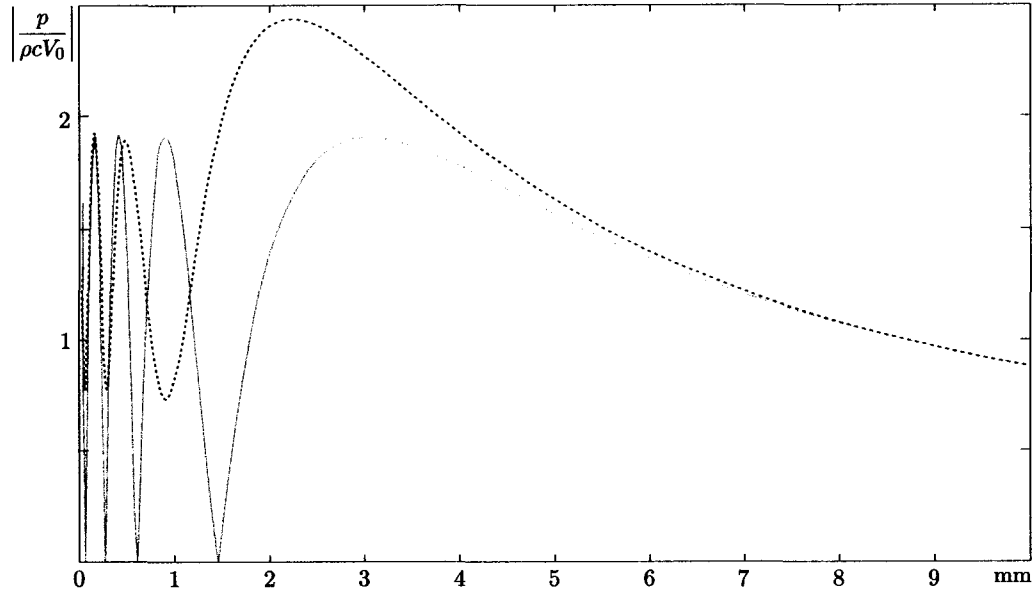


Figure 4.3. On-axis pressure for circular (solid red line) and rectangular (dashed blue line) transducers. Frequency: 15 MHz; sound velocity: 2400 m/s. Both transducers have the same area, 1 mm^2

4.2 Stationary Phase Approach

For the general case, equation (4.1) cannot be expressed analytically and its direct numerical integration is a computationally expensive task. The *stationary phase* approach provides considerably better performance. Rewriting equation (4.1) in a simplified form gives

$$I = \iint_S f(r) e^{i\phi(r)} dS. \quad (4.2)$$

We use the fact that for distant points the exponential part $e^{i\phi(r)}$ oscillates rapidly compared to $f(r) = 1/r$.

As a first step, the surface S of the transducer is subdivided into flat elements S_m ($m = 1, \dots, M$) to set the function $f(r)$ approximated in first order as constant. Let the distance from \mathbf{x} to the center of each element \mathbf{y}_m be

$$r_m = |\mathbf{r}_m| = |\mathbf{x} - \mathbf{y}_m|. \quad (4.3)$$

Denoting $f_m = f(r_m)$, we obtain

$$I = \sum_m f_m \iint_{S_m} e^{i\phi(r)} dS. \quad (4.4)$$

For an arbitrary point \mathbf{y} in S_m , the distance r can be approximated as

$$\mathbf{e}_m = \mathbf{r}_m/r_m; \quad r = r_m - \mathbf{e}_m \cdot (\mathbf{y} - \mathbf{y}_m). \quad (4.5)$$

Similarly, for the phase $\phi(r) = kr$, we have

$$\phi = \phi_m - k\mathbf{e}_m \cdot (\mathbf{y} - \mathbf{y}_m). \quad (4.6)$$

Equation (4.4) then becomes

$$I = \sum_m f_m e^{i\phi_m} \iint_{S_m} \exp[-ik\mathbf{e}_m \cdot (\mathbf{y} - \mathbf{y}_m)] dS. \quad (4.7)$$

Returning back to the Rayleigh-Sommerfeld expression (4.1), we obtain

$$p(\mathbf{x}) = \frac{-i\omega\rho V_0}{2\pi} \sum_m \frac{e^{ikr_m}}{r_m} I_m, \quad (4.8)$$

where

$$I_m = \iint_{S_m} \exp[-ik\mathbf{e}_m \cdot (\mathbf{y} - \mathbf{y}_m)] dS. \quad (4.9)$$

So far, the shape of S_m was arbitrary. Let's consider the case when S_m is a small rectangle with width a along the x axis and height b along the y axis. Equation (4.9) then can be rewritten as

$$I_m = \int_{-b/2}^{b/2} \int_{-a/2}^{a/2} \exp[-ik(e_{mx}u + e_{my}v)] du dv, \quad (4.10)$$

where e_{mx} and e_{my} are the components of vector $\mathbf{e}_m = \mathbf{r}_m/r_m$ along the x and y axes.

Integrating equation (4.10), we obtain the Fraunhofer diffraction expression:

$$I_m = ab \frac{\sin\left(\frac{a}{2}ke_{mx}\right)}{\frac{a}{2}ke_{mx}} \frac{\sin\left(\frac{b}{2}ke_{my}\right)}{\frac{b}{2}ke_{my}}. \quad (4.11)$$

The final expression for the pressure field generated by a flat piston transducer inside the liquid media is

$$p(x, y, z) = \frac{-i\omega\rho V_0}{2\pi} \sum_m \frac{e^{ikr_m}}{r_m} ab \frac{\sin\left(\frac{a}{2}ke_{mx}\right)}{\frac{a}{2}ke_{mx}} \frac{\sin\left(\frac{b}{2}ke_{my}\right)}{\frac{b}{2}ke_{my}}, \quad (4.12)$$

where

$$\mathbf{x} = (x, y, z); \quad \mathbf{y}_m = (u_m, v_m, 0); \quad (4.13)$$

$$r_m = \sqrt{(x - u_m)^2 + (y - v_m)^2 + z^2}; \quad (4.14)$$

$$e_{mx} = (x - u_m)/r_m; \quad e_{my} = (y - v_m)/r_m; \quad (4.15)$$

Using the stationary phase approach it is possible to reduce the number of elements into which the transducer surface S is subdivided. The applicability of this method is limited by the assumption that, in each element S_m , the distance attenuation term $1/r$ changes slowly compared to phase changes. For low frequencies (or small distances) this can require densities of the grid close to that required for direct application of Rayleigh-Sommerfeld integration, which makes the Fraunhofer approximation less effective.

4.3 Propagation through Interfaces—Direct Calculation

Direct numerical calculation of the field using the Rayleigh-Sommerfeld integral (4.1) or Fraunhofer approximation (4.12) can be adapted to an interface propagation case. Although, being computationally expensive, this approach provides an exact solution to the problem.

To calculate the field transmitted through an interface, one can take the following steps:

1. Subdivide the interface with a mesh, choosing its density to be small compared to the period of the phase oscillation across the interface;
2. Use equation (4.1) or (4.12) to calculate the distribution of the complex amplitude across the interface;
3. Knowing the wave number k in the first medium, and using the phase of the complex amplitude, calculate the local angle of incidence at each point and the corresponding transmission factor;
4. Multiply the amplitude of the incident wave by the transmission factor at each point and use the mesh from step 1 as a set of point sources to calculate the field in the second medium.

The calculation of local phase and transmission factors can be avoided in the paraxial approach. However, there are no strong reasons for doing this since it takes sufficiently less time compared to surface integrals, whether it is the Rayleigh-Sommerfeld integral (4.1) or the Fraunhofer approximation (4.12).

4.4 Equivalent Transformations

The number of calculation involved in the direct method makes this approach unsuitable for studying the general behavior of the system. The time required to calculate the beam structure also grows dramatically when more than one interface is involved, especially if the wavelength is relatively short and dense meshes must be used. Here we try to come up with a close approximation method, which is still good for particular geometries and materials.

As shown by Lester and Schmerr in [1], the transducer field in the second medium can be expressed as:

$$p = \frac{-i\omega\rho_1 V_0}{2\pi} \iint_S T(\theta_1) \frac{e^{i(k_1 D_1 + k_2 D_2)}}{\sqrt{D_1 + \frac{c_2}{c_1} D_2} \sqrt{D_1 + \frac{c_2 \cos^2 \theta_1}{c_1 \cos^2 \theta_2} D_2}} dS, \quad (4.16)$$

where D_1 is the distance from the point \mathbf{y} on the transducer to the interface and D_2 is the distance from the interface to \mathbf{x} along a ray that satisfies Snell's law (figure 4.4). This equation is valid in the high-frequency approximation, but it does not account for various types of interface waves. However for many practical applications it is likely to be sufficient.

In the paraxial approach, denoting

$$\gamma_1 = \frac{c_2 \cos \theta_1}{c_1 \cos \theta_2} \cong \frac{c_2 \cos \theta_{10}}{c_1 \cos \theta_{20}}, \quad (4.17)$$

where θ_{10} and θ_{20} are the stationary values for θ_1 and θ_2 , one can reduce (4.16) to

$$p = \frac{-i\omega\rho_1 V_0}{2\pi} \iint_S T(\theta_1) \frac{e^{i\phi}}{D_1 + \gamma_1 D_2} dS. \quad (4.18)$$

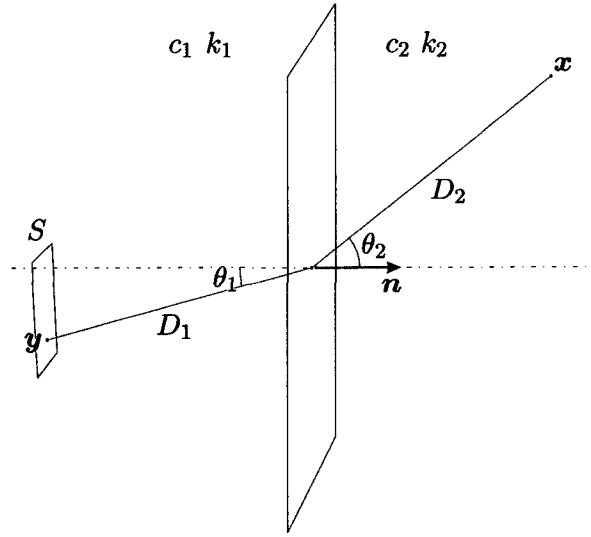


Figure 4.4. Propagation of a wave through an interface along a ray path

Similarly, the phase term can be approximated as

$$\begin{aligned}
 \phi &= k_1 D_1 + k_2 D_2 \\
 &= k_1(D_1 + \gamma_1 D_2) + k_2 D_2 - k_1 \gamma_1 D_2 \\
 &= k_1(D_1 + \gamma_1 D_2) + k_2 D_2(1 - \gamma_1 c_2/c_1).
 \end{aligned} \tag{4.19}$$

Finally, the expression for pressure in the second medium can be written as

$$p = \frac{-i\omega\rho_1 V_0 T(\theta_{10})}{2\pi} \exp [ik_2 D_2(1 - \gamma_1 c_2/c_1)] \iint_S \frac{e^{ik_1(D_1 + \gamma_1 D_2)}}{D_1 + \gamma_1 D_2} dS. \tag{4.20}$$

Equation (4.20) has the same form as the Rayleigh-Sommerfeld integral (4.1) with a phase correction term:

$$\Phi = \exp [ik_2 D_2(1 - \gamma_1 c_2/c_1)]. \tag{4.21}$$

Note that there exists a simple geometrical interpretation for equation (4.20). For a flat interface, defined with a plane equation in the vector form

$$(\mathbf{x} - \mathbf{s}) \cdot \mathbf{n} = 0, \tag{4.22}$$

we specify a vector transformation which transforms vectors in the second medium:

$$\mathbf{x}' = \Gamma(\mathbf{x}) = \mathbf{x} + [(\gamma_1 - 1) \mathbf{n} \cdot (\mathbf{x} - \mathbf{s})] \mathbf{n}. \quad (4.23)$$

Applying it to an arbitrary paraxial radius vector in the second medium, we can calculate the field at that point as if there were no interface. After that, the obtained value must be multiplied by the transmission coefficient T and phase correction factor Φ . Equation (4.23) defines the *equivalent transformation* for our system.

Geometrically, transformation Γ corresponds to stretching the post-interface half-space along the interface normal by a γ_1 factor (figure 4.5).

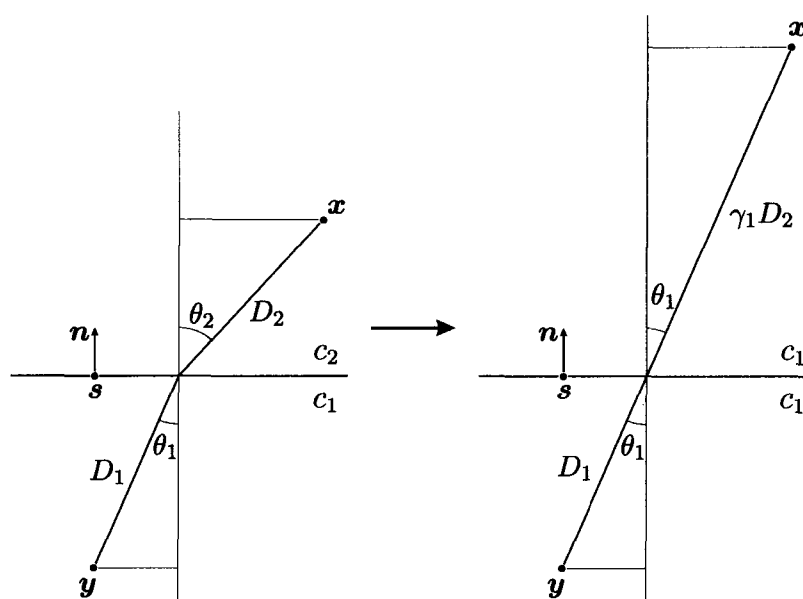


Figure 4.5. Geometrical interpretation of equivalent transformations

The important fact is that equivalent transformations can be applied to systems containing more than one interface, as shown in figure 4.6. For a paraxial point \mathbf{x} , located after the n -th interface, the equivalent transformation can be defined as

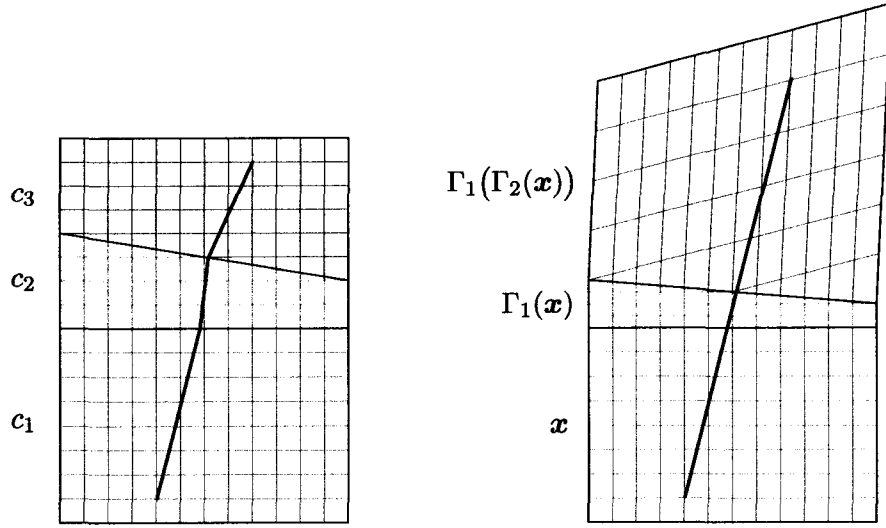


Figure 4.6. Equivalent transformation for multiple interfaces

$$\mathbf{x}^{(n)} = \Gamma_1(\Gamma_2(\dots \Gamma_n(\mathbf{x}))); \quad (4.24)$$

$$\Gamma_i(\mathbf{x}) = \mathbf{x} + [(\gamma_i - 1) \mathbf{n}_i \cdot (\mathbf{x} - \mathbf{s}_i)] \mathbf{n}_i; \quad (4.25)$$

$$\gamma_i = \frac{c_{i+1} \cos \theta_{i,0}}{c_i \cos \theta_{i+1,0}}; \quad (4.26)$$

and the final expression for the pressure after the n -th interface is

$$p = \frac{-i\omega\rho_1 V_0}{2\pi} \left[\prod_{i=1}^n T(\theta_i) \Phi_i \right] \iint_S \frac{e^{ik_n r_i^{(n)}}}{r_i^{(n)}} dS, \quad (4.27)$$

where

$$\Phi_i = \exp [ik_{i+1} D_{i+1} (1 - \gamma_i c_{i+1}/c_i)]; \quad (4.28)$$

$$r'_i = D_i + \gamma_i D_{i+1}. \quad (4.29)$$

The surface integral in (4.27) can in turn be estimated by direct numerical integration or by using the Fraunhofer formula (4.12). We should keep in mind, however, that this solution is based on the equation derived in the high-frequency approximation and in addition to that, we assumed paraxial location of the target point.

4.5 Calculating the Detected Signal

So far we considered only a forward-propagating wave. The next natural step is to show how this system is capable of detecting structural features and defects inside the sample, by measuring the reflected signal.

Consider an approximation where the transducer response to the incoming wave is linear to the wave pressure averaged across the transducer surface:

$$Q = \iint_{S_T} p_r(\mathbf{y}) dS(\mathbf{y}); \quad (4.30)$$

where point \mathbf{y} is in the transducer surface S_T (figure 4.7), and p_r is the pressure in the returning backward propagating wave, which is reflected from the defect inside the sample.

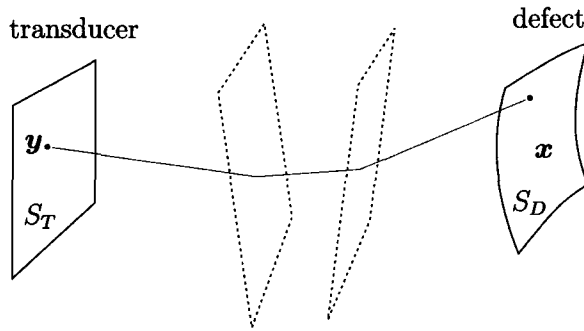


Figure 4.7. General model for obtaining detected signal

In the general case, the pressure at the surface of the defect can be expressed as

$$p(\mathbf{x}) = \frac{-ik_0 p_0}{2\pi} \iint_{S_T} \vec{\mathbb{T}} f(\mathbf{x}, \mathbf{y}) e^{i\phi(\mathbf{x}, \mathbf{y})} dS(\mathbf{y}); \quad (4.31)$$

where \mathbf{x} is the point at the surface of the defect S_D , and $\vec{\mathbb{T}}$ is the effective transmission factor. The function $f(\mathbf{x}, \mathbf{y})$ corresponds to the phase path from \mathbf{x} to \mathbf{y} and $\phi(\mathbf{x}, \mathbf{y})$ is

the corresponding phase factor. In the simplest case of no interfaces and no attenuation these functions can be as simple as

$$f(\mathbf{x}, \mathbf{y}) = \frac{1}{|\mathbf{x} - \mathbf{y}|}; \quad \phi(\mathbf{x}, \mathbf{y}) = e^{ik|\mathbf{x} - \mathbf{y}|}. \quad (4.32)$$

When working with multiple interfaces, these functions also include transmission and attenuation factors and can be evaluated using the Rayleigh-Sommerfeld integral, equivalent transformations, or other methods. The key feature here is that these functions do not depend on the direction of propagation, that is $f(\mathbf{x}, \mathbf{y}) = f(\mathbf{y}, \mathbf{x})$ and $\phi(\mathbf{x}, \mathbf{y}) = \phi(\mathbf{y}, \mathbf{x})$.

The surface of the defect reflects back a part of the incoming wave, acting as a secondary source for the backward propagating wave. Denoting the reflection factor at the defect boundary as $R(\mathbf{x})$, we obtain local amplitudes of the secondary sources as $R(\mathbf{x})p(\mathbf{x})$. Therefore the pressure p_r is

$$p_r(\mathbf{y}) = \frac{-ik}{2\pi} \iint_{S_D} R(\mathbf{x})p(\mathbf{x}) \overleftarrow{\mathbb{T}} f(\mathbf{y}, \mathbf{x}) e^{i\phi(\mathbf{y}, \mathbf{x})} dS(\mathbf{x}), \quad (4.33)$$

where $\overleftarrow{\mathbb{T}}$ is the effective transmission factor for the wave travelling back from defect to transducer.

Combining this with equation (4.30), we obtain

$$\begin{aligned} Q &= \iint_{S_T} \frac{-ik_N}{2\pi} \iint_{S_D} R(\mathbf{x})p(\mathbf{x}) \overleftarrow{\mathbb{T}} f(\mathbf{y}, \mathbf{x}) e^{i\phi(\mathbf{y}, \mathbf{x})} dS(\mathbf{x}) dS(\mathbf{y}) \\ &= \iint_{S_D} R(\mathbf{x})p(\mathbf{x}) \overleftarrow{\mathbb{T}} \frac{-ik_N}{2\pi} \iint_{S_T} f(\mathbf{y}, \mathbf{x}) e^{i\phi(\mathbf{y}, \mathbf{x})} dS(\mathbf{y}) dS(\mathbf{x}). \end{aligned} \quad (4.34)$$

Recall now that functions $f(\mathbf{x}, \mathbf{y})$ and $\phi(\mathbf{x}, \mathbf{y})$ are the same regardless of the direction of propagation. After swapping the arguments in these functions, the inner integral becomes similar to the pressure at the defect boundary induced by a forward propagating wave (4.33). The final expression for the transducer response can be written

as

$$Q = \frac{1}{p_0} \frac{\overleftarrow{\mathbb{T}} k_N}{\overrightarrow{\mathbb{T}} k_0} \iint_{S_D} R(\mathbf{x}) p^2(\mathbf{x}) dS(\mathbf{x}); \quad (4.35)$$

or, for relative amplitudes, and assuming variations of transmission factors are small within the main beam,

$$\frac{Q}{p_0} = \frac{c_0^2}{c_N^2} \iint_{S_D} R(\mathbf{x}) \frac{p^2(\mathbf{x})}{p_0^2} dS(\mathbf{x}); \quad (4.36)$$

Equation (4.36) shows that building the structure of a forward-propagating beam $p(\mathbf{x})$ provides enough information to estimate the response of the transducer to a great variety of defects. The only assumption in deriving this equation is that the variation of transmission factors is small across the main beam propagating through each interface. There was no assumption made on shape, location, or reflectivity of the defect boundary. Generally, the applicability of this method is limited by the precision of the method used to find the field pressure at the defect boundary.

As shown in Chapter 3, the reflection factor $R(\mathbf{x})$ is determined by material properties and by the angle of incidence. For each point of the defect's surface, this angle can easily be obtained from the phase distribution at that point. In order to estimate this angle numerically, consider the defect whose the surface is subdivided by a rectangular mesh $\mathbf{m}_{i,j}$ with grid step a ; that is $|\mathbf{m}_{i+1,j} - \mathbf{m}_{i,j}| = |\mathbf{m}_{i,j+1} - \mathbf{m}_{i,j}| = a$. Using the method of equivalent transformations we can estimate the phase $\phi_{i,j}$ of the incoming wave at each node of this mesh. Provided the mesh is dense enough to consider phase changes across each cell to be linear, the local angle of incidence can be approximated as (see Appendix B)

$$\alpha_{i,j} = \arccos \left[\frac{d_1^2}{a^2 - d_1^2} + \frac{d_2^2}{a^2 - d_2^2} + 1 \right]^{-1/2}, \quad (4.37)$$

where

$$d_1 = (\phi_{i+1,j} - \phi_{i,j}) / k; \quad d_2 = (\phi_{i,j+1} - \phi_{i,j}) / k. \quad (4.38)$$

A similar expression can be derived for an arbitrary non-rectangular mesh.

The choice of the mesh density is imposed by the phase variations in the direction tangential to the interface. In most cases, choosing the mesh step 5–10 times smaller than the average distance corresponding to a 2π -phase change across the boundary, appears to be sufficient. There are no noticeable changes in the results when the mesh step is smaller. Furthermore, the same mesh can be used to estimate the integral in (4.36).

In the following sections we study how relative alignment of transducer, sample surface, and defect surface inside the sample can influence the amplitude of the detected signal.

4.6 Comparing Different Methods

In order to estimate how much precision is lost due to a paraxial approach, let's compare results of exact calculations with those obtained using equivalent transformations.

A few refinements should be added to the model developed in Chapter 3. Consider a 1×1 -mm transducer radiating at 15 MHz into a 5 mm thick delay layer. As in the plane-wave model, the delay is made of polystyrene and is coupled with the ultrasonic gel. The investigated sample is a steel plate with an approximate depth of defects in 1–2 mm range.

First, we compare the structure of the field. In figure 4.8, the beam generated by the transducer was modelled using the three methods: the brute-force Rayleigh-Sommerfeld integration, equivalent transformations coupled with Rayleigh-Sommerfeld integration, and equivalent transformations with Fraunhofer approximation. The field distribution was calculated for a 1 mm thick gel layer and a 5° tilt of the sample relative

to the delay layer surface. The choice of a 5° angle is imposed by practical considerations; it is close to the maximum tilt at which the experimental system is still capable of recognizing defects lying at about 1 mm depth inside the metal.

To present the data in the most informative way, these images show only the beam structure as a result of diffraction; this amplitude should also be multiplied by the corresponding transmission factor after passing through each interface.

From the data obtained, we can see that the general picture of the field distribution is retained despite the approximations. The first apparent difference is a phase discontinuity, which is a characteristic feature of the Fraunhofer approach. However, these phase jumps are located in the area of zero amplitude separating main and side beams, therefore it does not contradict common sense. In addition, compared to exact calculations, the side beams diverge slightly less in data obtained using the equivalent transformations method. This is an obvious consequence of the paraxial approach. Taking into account the small amplitudes of these beams, one can expect this difference to be unimportant.

The main goal of applying the method of equivalent transformations is to increase the computational performance. It is not an easy task to provide exact benchmarking, but in any case the difference is of several orders of magnitude. When using the Fraunhofer approximation, the procedure of obtaining the pressure at an arbitrary location becomes completely analytical, and the resulting images of field distribution, similar to figure 4.8, can be obtained in less than a second on a standard PC.

To estimate the difference between the three methods numerically, let's compare results of the calculation for a large flat-parallel defect¹ (figure 4.9). From these results we conclude that the method of equivalent transformations provides numerical results

¹In this case the size of the defect is 8 mm which is large compared to the transducer size. The exact dependence of the signal on the defect size will be studied in the next chapter

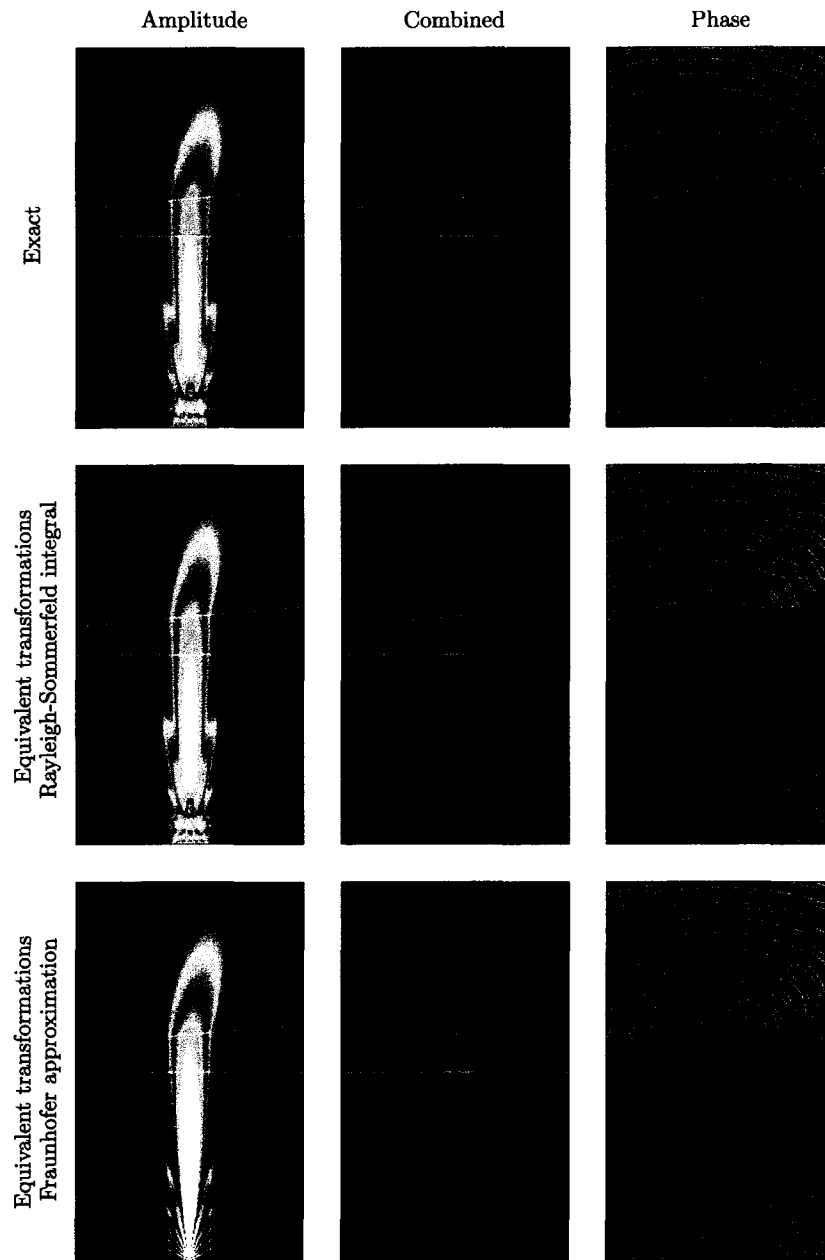


Figure 4.8. Comparison of exact calculations with the method of equivalent transformations. A 1×1 -mm transducer radiates at 15 MHz into a 5 mm polystyrene delay layer. The delay is coupled with 1 mm layer of ultrasonic gel adjoining to a tilted steel sample at the angle of 5° . Each image shows an area of 6×10 mm.

The amplitudes do not include the influence of the transmission factor.

close to those obtained using the brute-force Rayleigh-Sommerfeld integration. The small difference can be attributed to limitations of the paraxial approach. It can also be caused by that fact that transmission factors were calculated only for the central beam direction, while in the exact method, they were calculated locally at each point of the interface. In addition, the method of equivalent transformations is based on (4.16), which is valid in the high frequency approximation; for smaller distances the results might not be as accurate.

In fact, the accuracy of the experimental data is much worse when the differences between the approximations. In figure 4.10 a comparison between the experimental and theoretical data is provided. Since there is no reference point in terms of gain, the amplitude of the theoretical surface reflection has been fitted using least squares to the voltage of surface peaks in experimental data. Each experimental point in this graph corresponds to the averaged result of five neighboring elements.

The green 0.05 V zone at the bottom of the graph corresponds to the noise level in the measurement system. Due to its semi-regular structure, it is not possible to get rid of this noise by averaging several measurements; it also can not be filtered by the Fourier transform or other filtering methods because the frequency of this noise is close to the central frequency of the transducer. Determining the origins of this noise and methods of getting rid of it is an additional complex problem which lies beyond the scope of this work.

One of the important conclusions here is that the model yields results which are consistent with the experimental data. The continuous wave approximation proves to be sufficient despite that fact that the real transducer operates in a short-pulse mode, when the length of each pulse is just a few wavelengths.

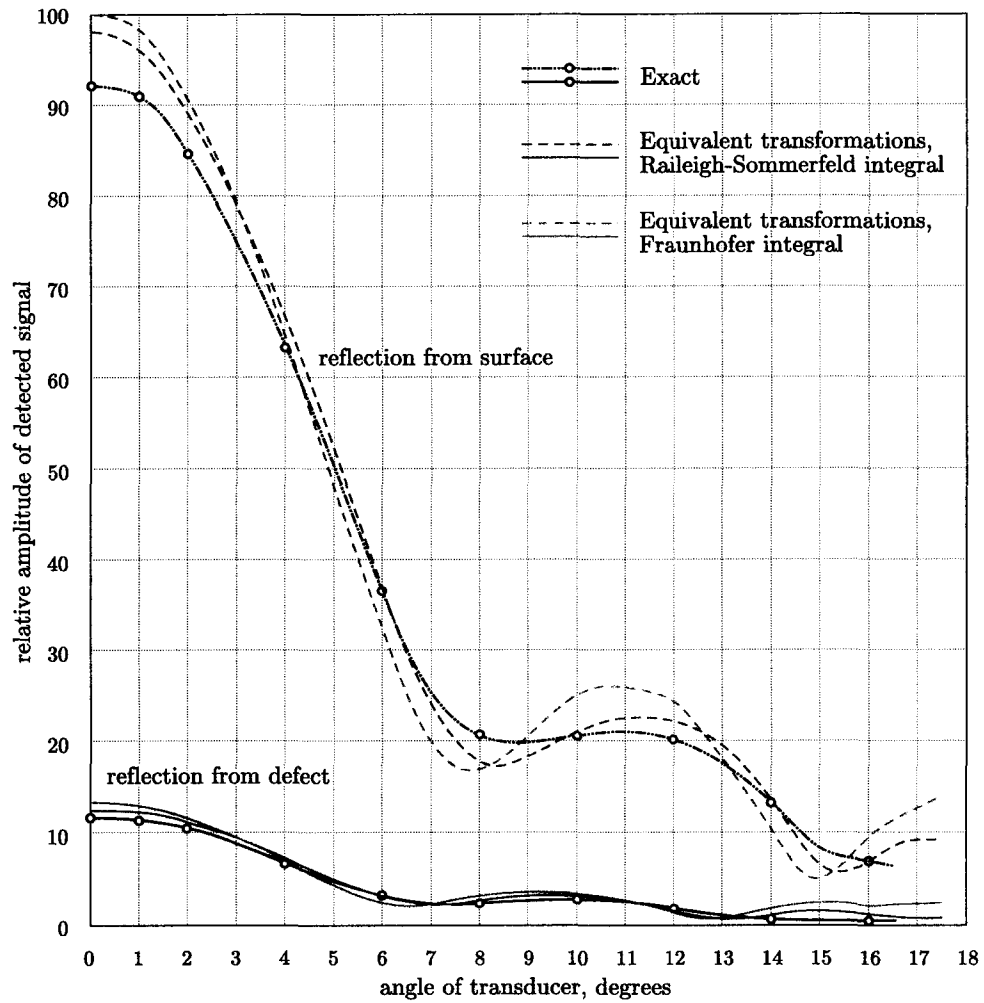


Figure 4.9. Using different approximations to calculate transducer response. Dashed lines correspond to the surface reflection, solid lines correspond to the reflection from a large flat 1 mm deep defect

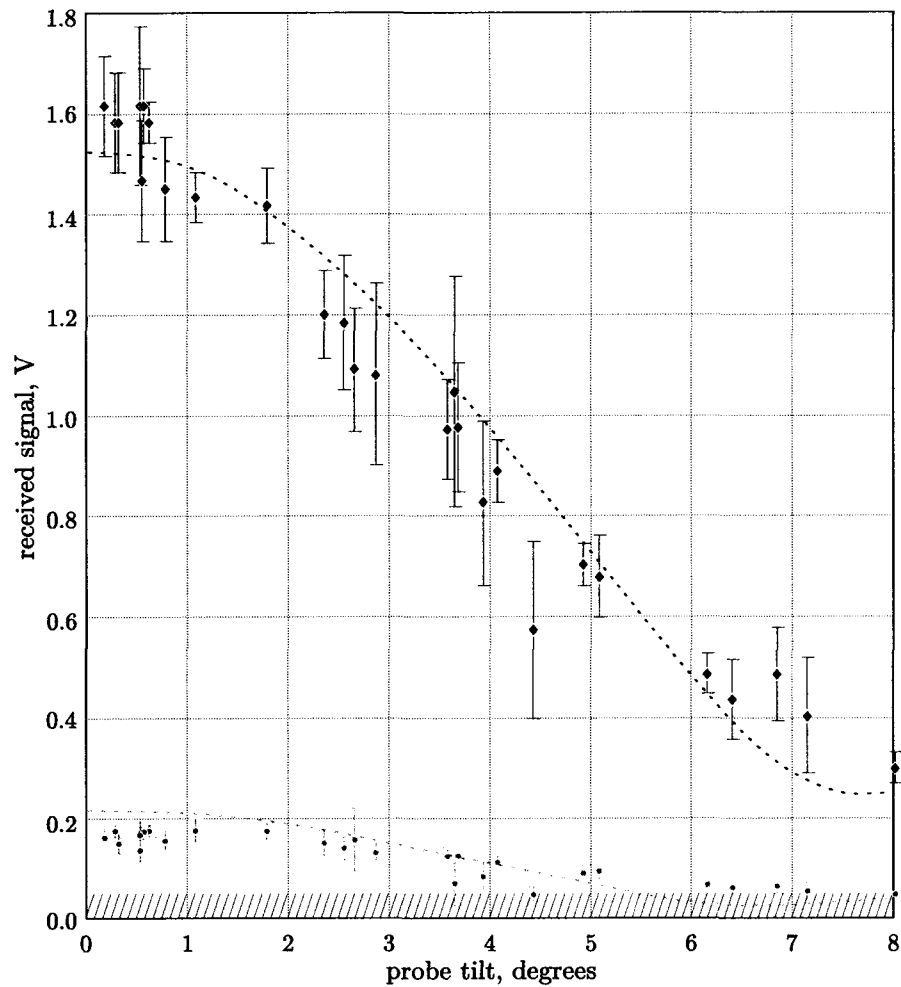


Figure 4.10. Comparing experimental and theoretical results. The upper line is a reflection from the surface, the lower line is a reflection from the bottom of a 1.5- mm steel plate. Dashed lines correspond to theoretical data, dots correspond to experiment

CHAPTER 5

Studying the Behavior of the Model

In this chapter the mathematical model designed for the single element is studied numerically. At the beginning, the response of a single transducer element is estimated in various situations, demonstrating how the model predicts the received signal amplitude. This data is gathered later to show how the whole matrix of multiple transducers is capable of visualizing various types of defects and structural features in investigated samples.

5.1 Specifying the Reference System

To estimate the behavior of a single element, the number of parameters influencing the transducer response should be studied. These parameters include the size of the transducer, its frequency, the thickness and the material of the delay line, the thickness and the acoustical properties of the immersion, the material of the sample, the location and the properties of the defect inside the sample, the shape of the defect

and its orientation, and other parameters. All together this satiates the model with many degrees of freedom, making the general discussion on its behavior inappropriate. Probably the best logical approach is to take a particular configuration and study how changes in one of two parameters influence the resulting signal. From such data, it should be possible to conclude what changes should be made to the initial configuration to optimize it for better performance in comparison to the initial system.

We choose the same reference configuration as in the previous chapter. The parameters of this system are presented in Table 5.1.

Table 5.1. Parameters of the modelled system

Part	Parameter	Value in reference system
Transducer	size	$1.0 \times 1.0 \text{ mm}^2$
	frequency	15 MHz
Delay line (polystyrene)	density, ρ	1050 kg/m^3
	velocity, c_L	2400 m/s
	thickness	5 mm
Immersion (ultrasonic gel)	density, ρ	1300 kg/m^3
	velocity, c_L	1900 m/s
	thickness	1 mm
Sample (steel)	density, ρ	7900 kg/m^3
	velocity, c_L	5900 m/s
Defect (air)	density, ρ	$\approx 1 \text{ kg/m}^3$
	velocity, c_L	350 m/s

In this chapter we are only interested in relative amplitudes of the received signal. The amplitude of 100% will be attributed to the reference system, when it radiates into a flat-parallel immersion layer (1 mm thick) and the large flat parallel defect is located

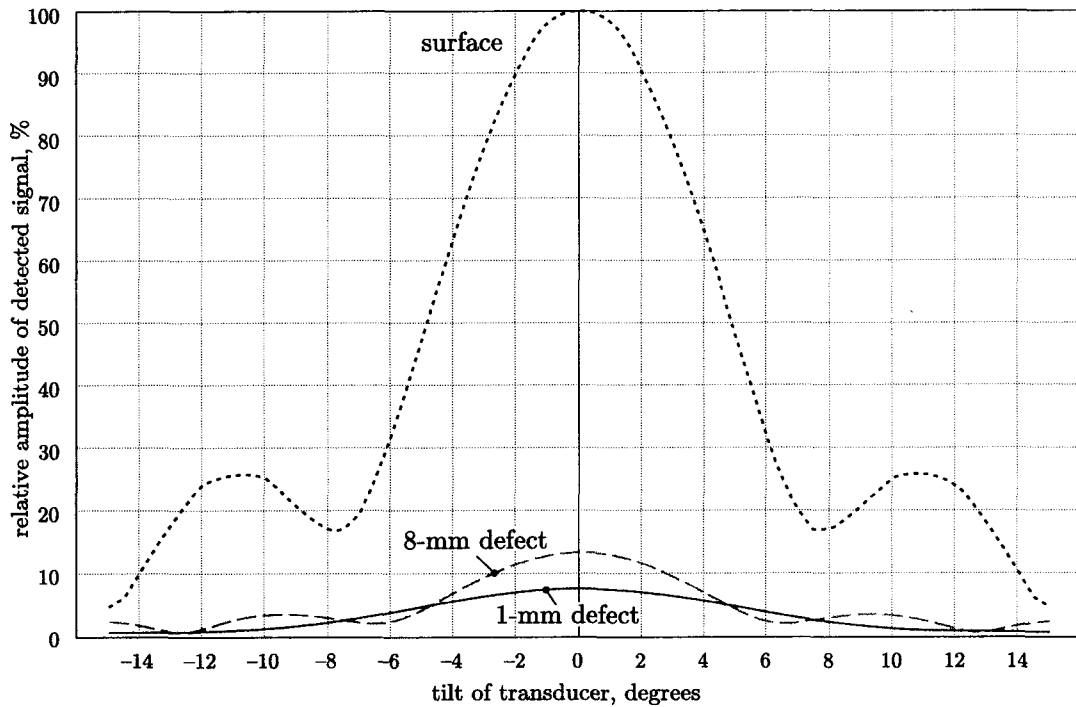


Figure 5.1. Dependence of signal on transducer tilt for reference system

1 mm below the surface. This configuration can also be described as a reflection from the 1 mm thick steel plate. Figure 5.1 shows the data obtained for an 8×8 mm defect, which in this context may be considered infinite. In addition, a small 1×1 mm defect was calculated for the same configuration. The relative amplitude of the large defect reflection is 13.5% (for normal incidence), which decreases down to 7.6% for the small defect.

One of the most important factors influencing the resulting image is the angular stability of the transducer. As we can see, even small variations of a few degrees in tilt of transducer relative to the sample surface may cause severe changes in the received signal. In this chapter we will be paying a lot of attention to the angular stability. The results of the theoretical calculations in this chapter illustrate how changes in the reference system alter this dependence.

5.2 Influence of Delay Line and Immersion Layer

As a first step in these virtual experiments, consider dependence of the received signal on the thickness of the polystyrene delay, as shown in figure 5.2. In addition, a couple of angular dependencies for different thicknesses of the delay line are shown in figure 5.3. Notice that the amplitude of the surface reflection slightly increases for larger delays and that for small internal defects—decreases. Although the correctness of the method of equivalent transformations should be questioned for small thicknesses of the delay line, the general conclusion is that smaller delay sizes are beneficial. The amplitude of the reflected signal is stronger and the angular dependence is not as sharp as for large delays. The overall change, however, is relatively small, and the system is similarly stable to variations in the immersion layer thickness (figure 5.4).

A simple physical explanation for this stability can be derived from that fact that the wavelength in both delay line and gel is small. At the frequency of 15 MHz, the wavelengths in polystyrene and gel are 0.16 mm and 0.13 mm correspondingly. Compared to 1 mm size of the transducer, it appears to be small enough to behave similar to the plane wave, that is the spreading of the energy is small.

There is also an interest in using the same transducer with a water column instead of the delay line and gel. This system is easier to model, because there are less interfaces on the wave path, however, because the impedance of the water is lower than that of the polystyrene or ultrasonic gel, less signal penetrates inside the sample. Notice from figure 5.5, that the amplitudes of surface and internal reflections are smaller than in the reference system. At the same time, this system appears to be more stable to defect size and for small sizes of water columns, the angular sensitivity is comparable to that in the reference system (figure 5.6).

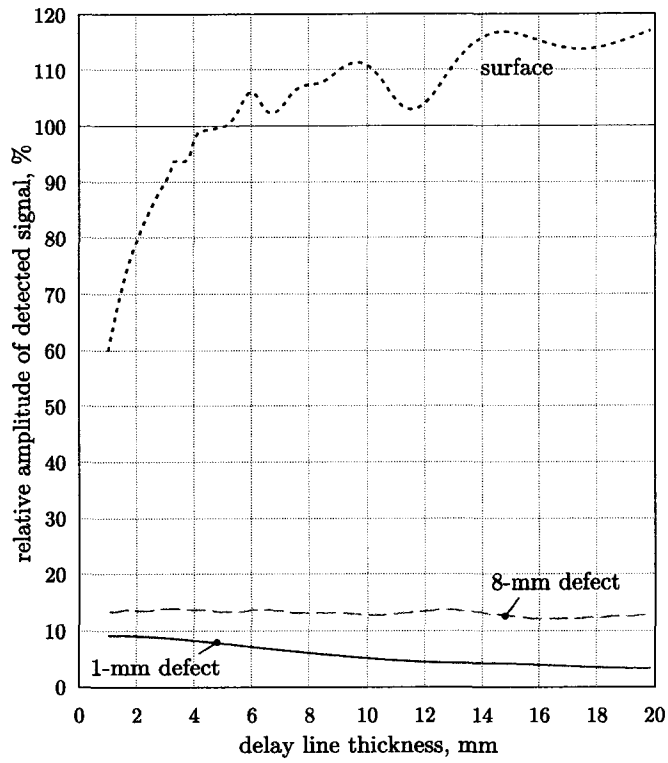


Figure 5.2. Dependence of the signal on thickness of delay line

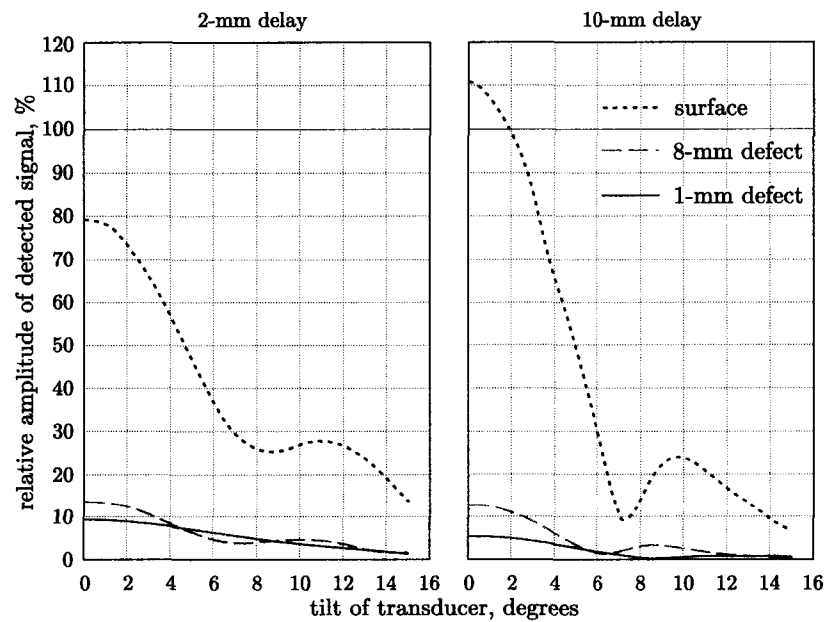


Figure 5.3. Angular sensitivity for different thicknesses of delay line

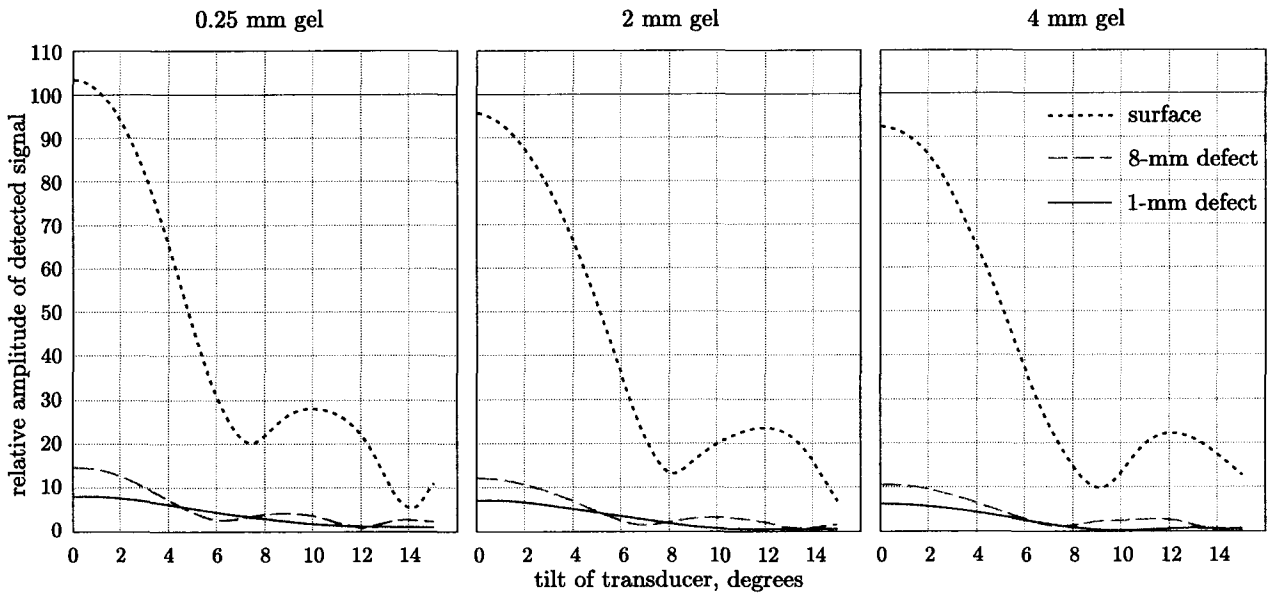


Figure 5.4. Influence of immersion layer thickness

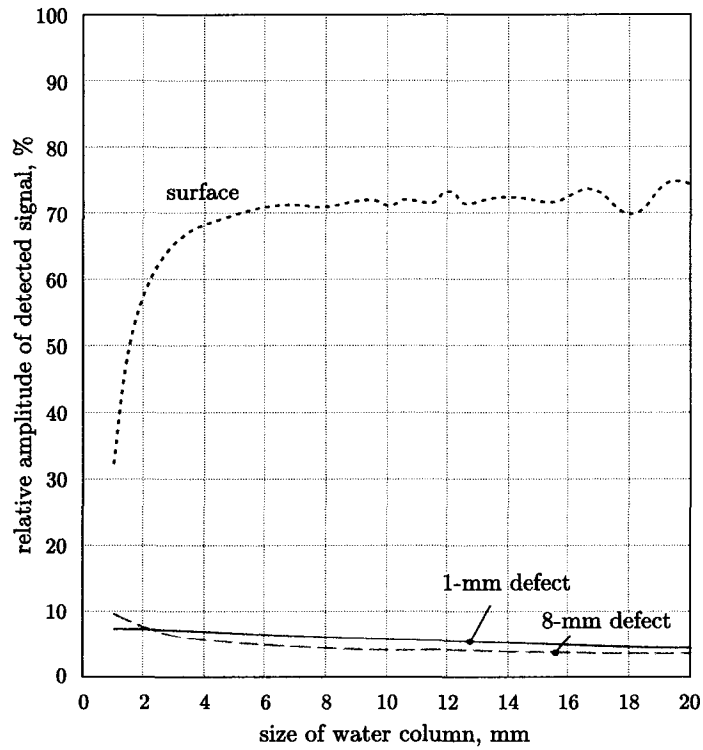


Figure 5.5. Dependence of the signal on thickness of the water column

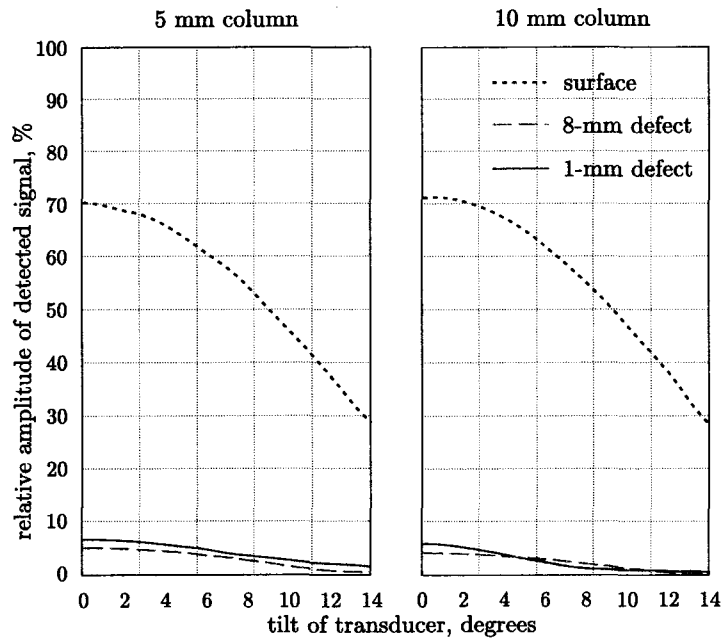


Figure 5.6. Angular sensitivity for various thicknesses of the water column

5.3 Influence of Defect Location and Orientation

The dependence of the detected signal on the depth of the defect is shown in figure 5.7. The defect is centered relative to the transducer. For small defect sizes, the amplitude of the reflected signal grows with the size of the defect, however when the defect becomes larger than the transducer, this growth slows down and eventually, when the size of the defect is above a certain value, the further increase is no longer noticeable. This threshold depends on the size of the element and on its depth. The deeper the defect is inside the sample, the larger this threshold is.

Similarly the dependence on the defect orientation can be obtained. In figure 5.8 such a dependence is shown for various defect sizes. The general conclusion here is that the transducer is less sensitive to orientation of small defects, although even for large defects this sensitivity is less critical than the sensitivity of the transducer to the

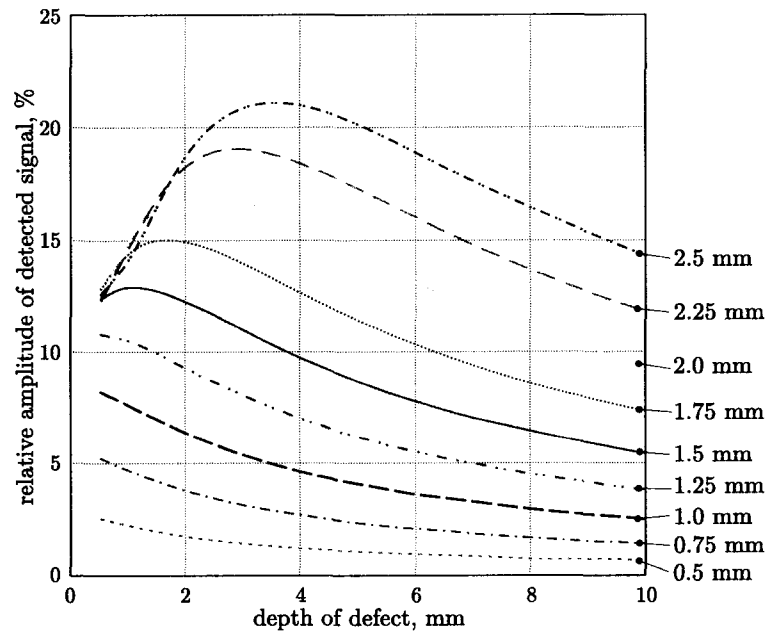


Figure 5.7. Reflection amplitudes vs. defect depth for various sizes of defects

tilt of the surface.

Consider now the defects which are not aligned on the axis of the transducer. Figure 5.10 demonstrates results of numerical modeling for various sizes of defects. In the same figure, a partial coverage of the same defects by the transducer is shown. The partial coverage (figure 5.9) corresponds to the signal which would have been received in an idealized plane wave model. Notice that the calculated curves in figure 5.10 appear to be less dense than those corresponding to partial coverage.

It is possible to choose the effective size of the transducer to make the coverage curves close to that calculated with the method of equivalent transformations. By fitting the coverage factors for various transducer sizes, we deduce that the best effective size of the transducer is 1.5×1.5 mm. Figure 5.11 shows the coverage factors corresponding to a 1.5 mm transducer and the same factors superimposed on the previously obtained displacement dependencies. From the physical point of view this can

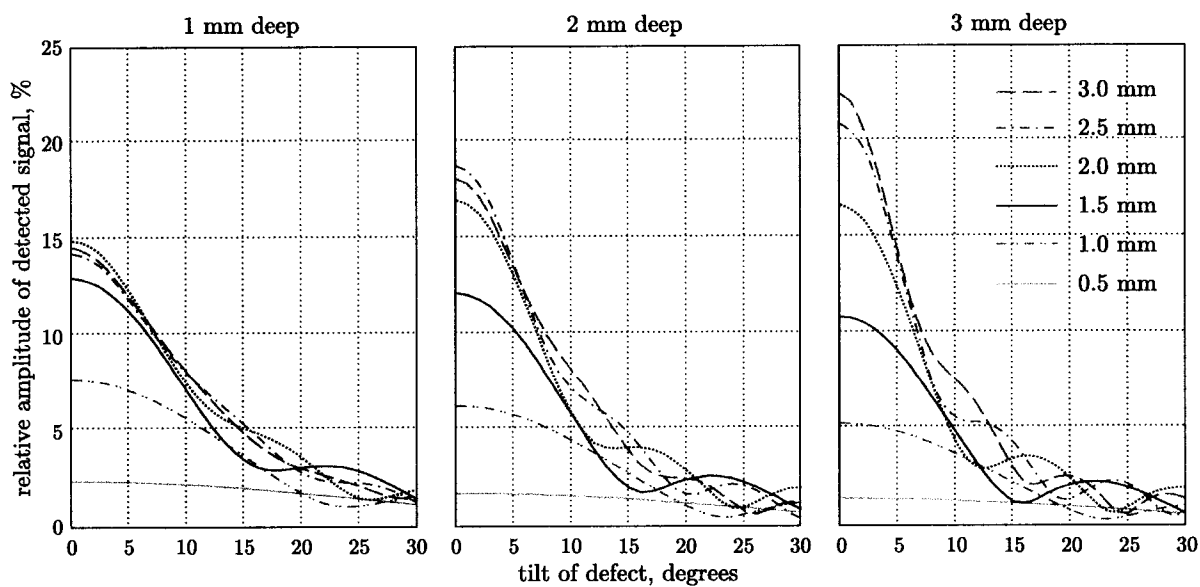


Figure 5.8. Dependence of the reflected signal on defect tilt for various defect sizes

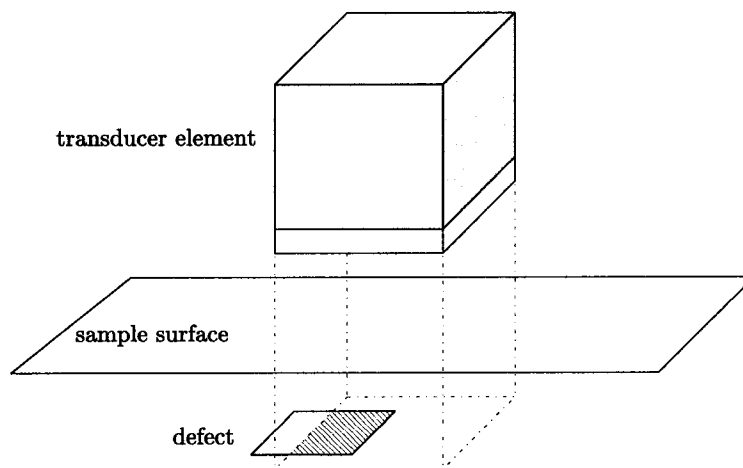


Figure 5.9. Lateral displacement of defects and partial coverage. The partial coverage is the ratio of the hatched area to the area of the transducer's surface.

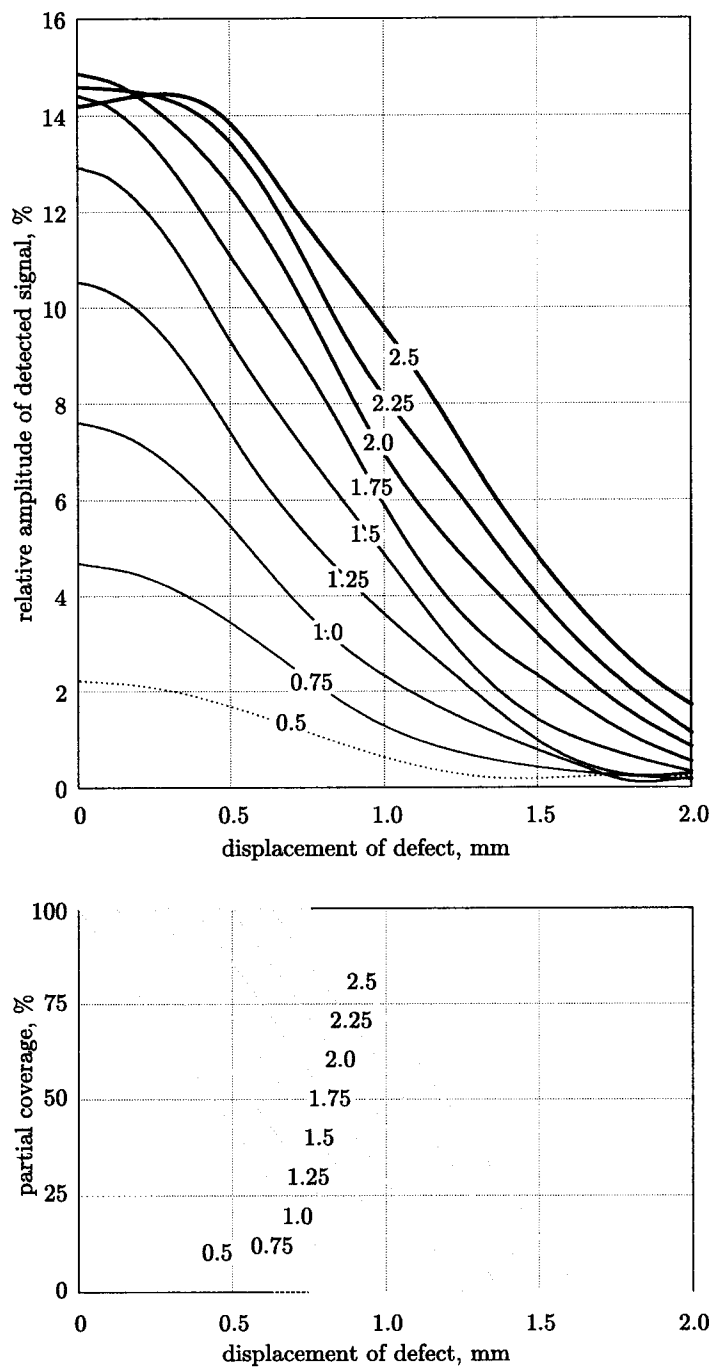


Figure 5.10. Dependence of reflected signal on lateral defect displacement for various defect sizes

be explained as a result of beam spreading inside the sample, which effectively enlarges the area radiated by the transducer. Using this effective transducer size it is possible to choose the size of the resampling kernel to interpolate the image acquired by the transducer.

The effective size of the transducer is larger for deeper effects. The effective size is smaller for larger transducers¹, which can be explained by the larger beam spread for smaller transducer sizes. Figure 5.12 illustrates this dependence.

5.4 Dependence on Transducer Frequency

The frequency of the transducer is influenced by the properties of the piezoelectric material and its thickness. In this work, the transducer is presented as an idealized continuous-wave model with a single frequency. However, the real transducer operates in a short pulse mode and its spectrum is continuous. So far, a 15 MHz frequency has been chosen for modeling, which corresponds to the central frequency of the experimental setup. This simplification does not have a significant impact on the results of the modeling. However, for more precise models, a band of frequencies should be taken into account.

In this section, we proceed with a continuous-wave approximation, but the field structure is now obtained for different frequencies. Figure 5.13 shows the field structure for transducer elements operating at 5, 10, 15, and 20 MHz. Notice that for low frequencies the field tends to be more similar to a point-source field with rapidly decreasing amplitude as we move away from the source. At higher frequencies, the field approaches a plane-wave with substantially smaller spreading. On the other hand,

¹For really large transducers this dependence is reversed and the effective size grows with the transducer

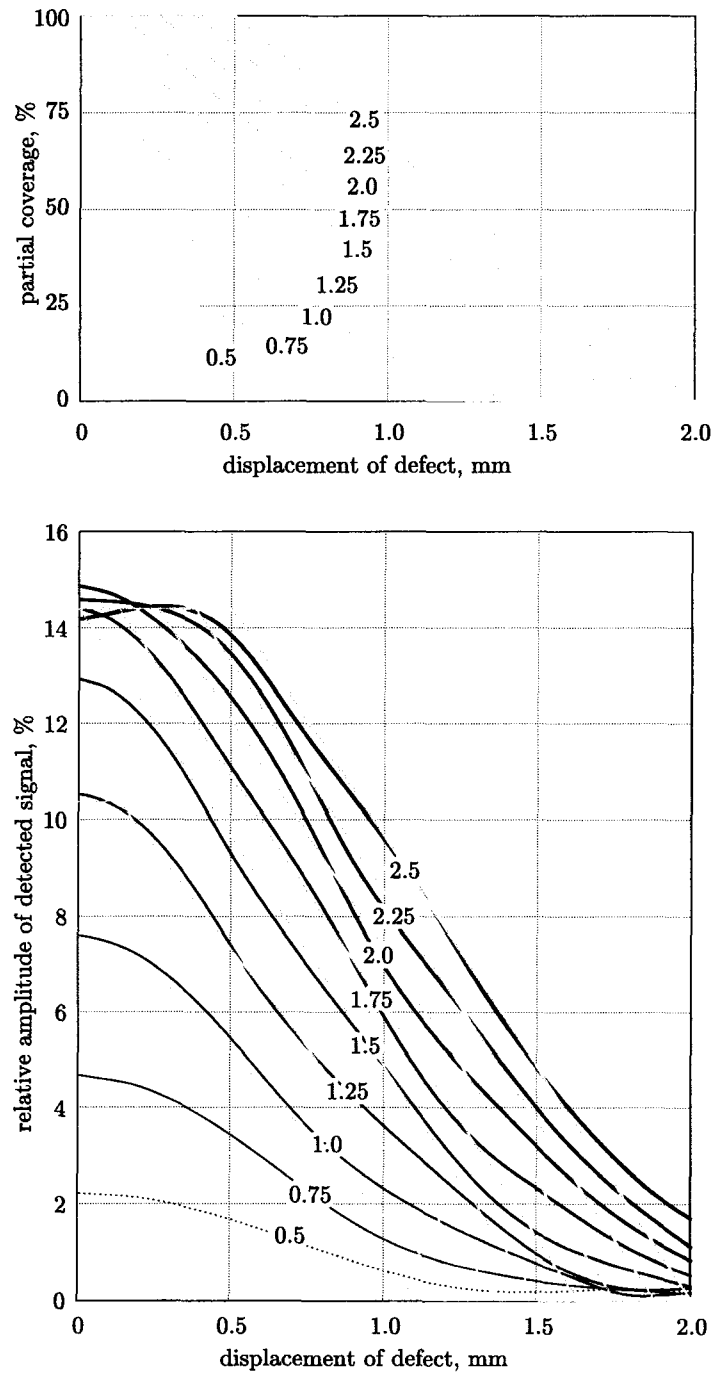


Figure 5.11. Choosing the effective size of the matrix element

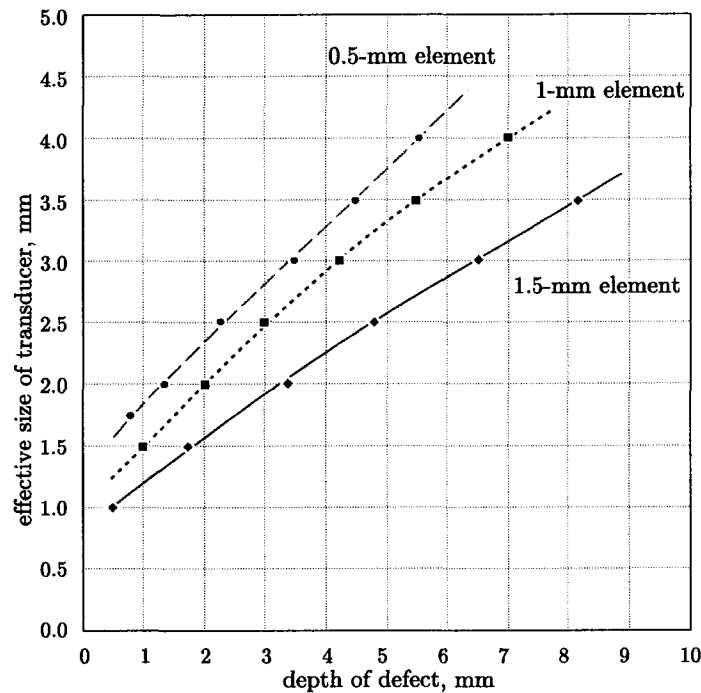


Figure 5.12. Effective sizes of matrix elements

the higher frequency results in a sharper angular dependence. That is, high-frequency transducers are more sensitive to orientation relative to the sample surface.

The angular dependence for various frequencies explains an interesting phenomena, which can actually be observed experimentally. The central frequency of the received signal slightly depends on the tilt of transducer. Different wavelengths in the initial signal spectrum have different angular dependence, therefore the reflected signal from both the surface and the defect tends to have lower central frequency for larger tilts. This effect is illustrated in figure 5.14 where the signal received by the transducer is shown in the time domain and in the frequency domain. The first set of images shows the signal for the element tilted at 0.29° ; the second set was obtained with the transducer tilted at 4.42° relative to the surface. The experimental data for this figure were obtained with a 1.5 mm thick steel plate. As we can see, the central frequency

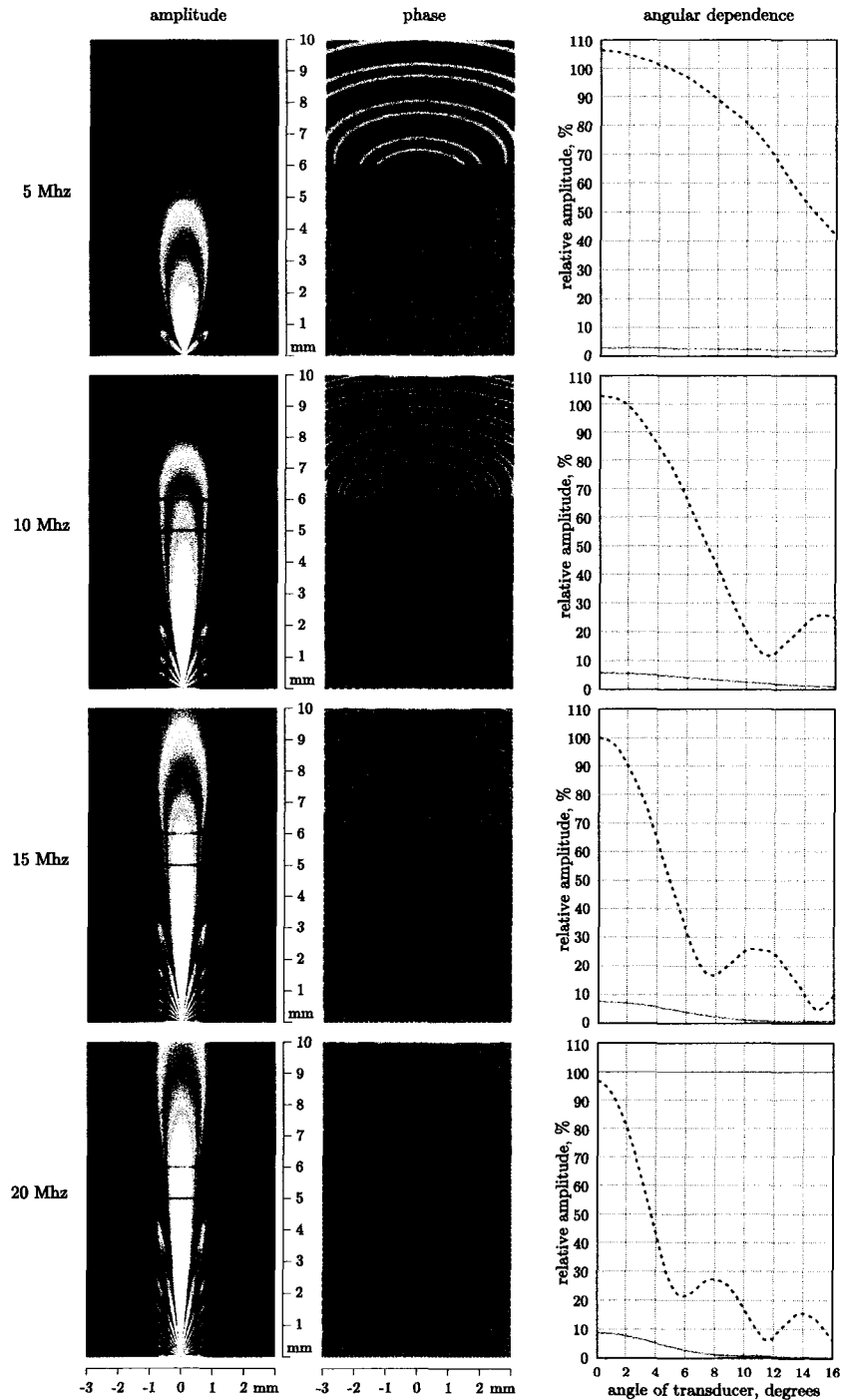


Figure 5.13. Dependence on transducer frequency. The angular dependence graphs show the surface reflection (dashed line) and the reflection from 1×1 mm defect 1 mm deep inside the steel

in the second case is approximately 2–3 MHz lower.

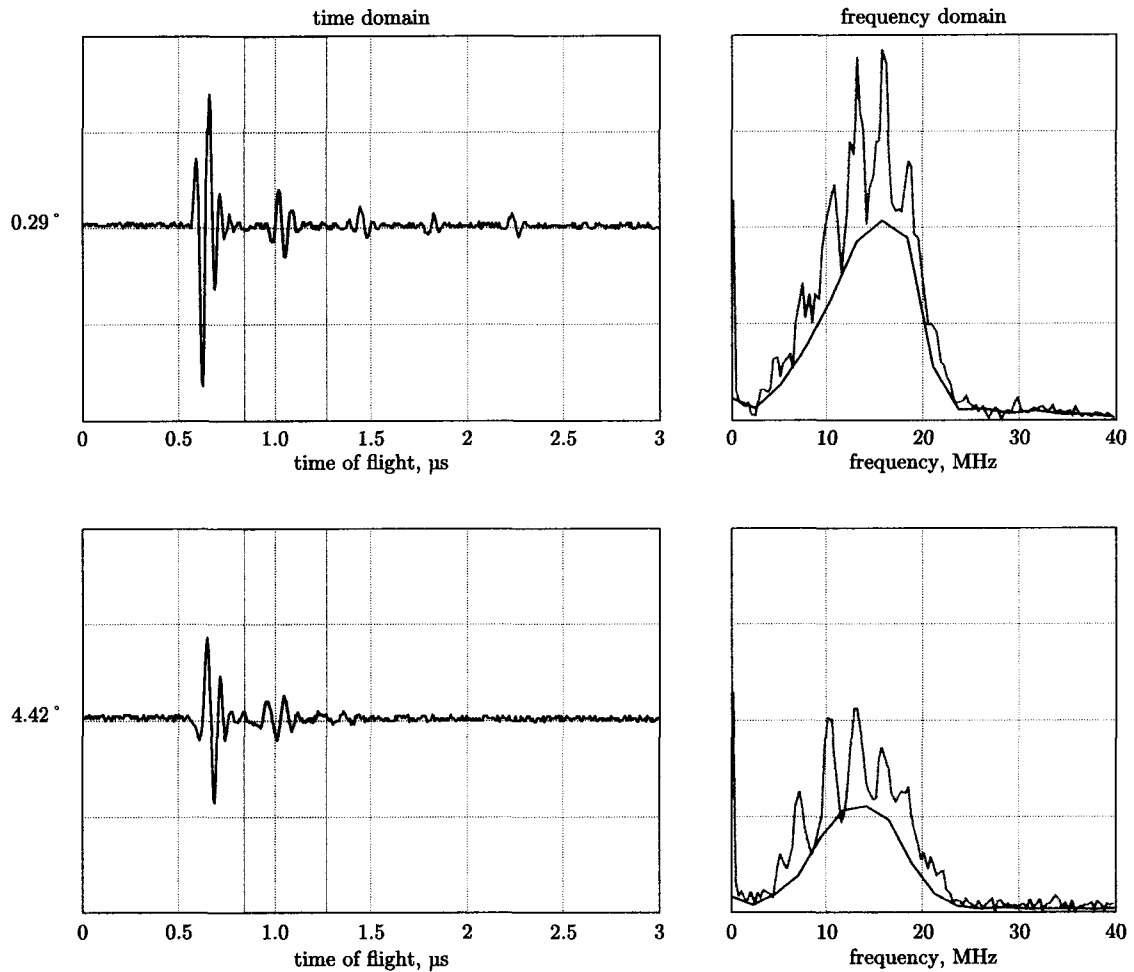


Figure 5.14. Frequency shift for two different angles of transducer. The frequency domain images show the results if the fourier transform for the whole signal (red line) and for the part of the waveform from the signal gates (green line)

5.5 Obtaining Images

Now, when we have some understanding of a single element in the matrix transducer, we can see how 2D images are obtained. As mentioned earlier, the transducer operates

in a short-pulse mode; that is, the arrival of signals reflected from surface and internal defects is separated in time. Figure 5.15 shows a typical waveform received by each element.

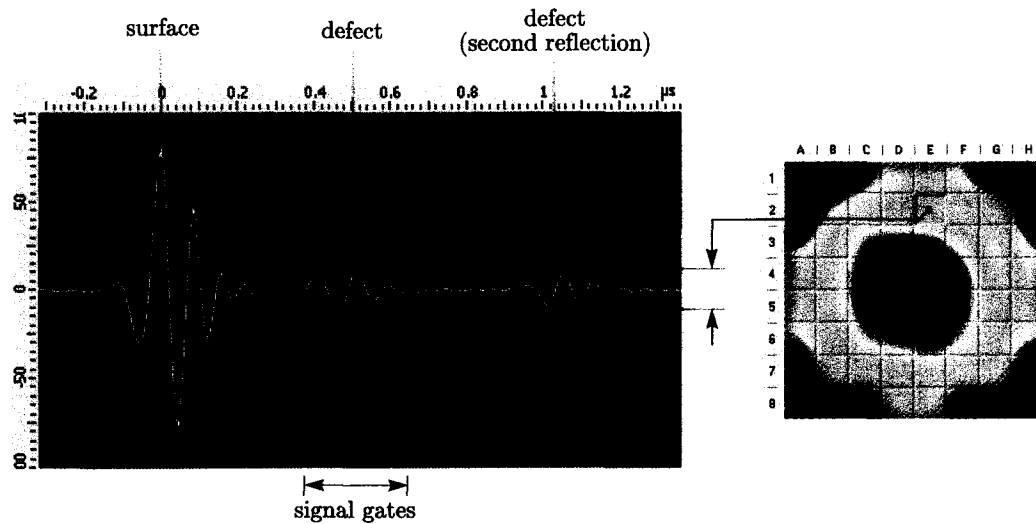


Figure 5.15. A typical waveform received by the element of a transducer

The amplitude of the internal reflection is obtained as a maximum amplitude within the *signal gates*. This value is used to modulate the brightness of an image at the corresponding point. The 2D image is then interpolated and shown in grayscale or using a color palette. This is a standard technique used by many ultrasonic devices also known as *C-scan imaging*. The interpolation stage here is optional, it does not bring in any new information about the sample. However, it produces images that are more suitable for visual inspection. The quality of the interpolation is better if the increased effective size of the transducer elements is taken into account.

Three different techniques have been proposed to improve the quality and stability of the images [19]:

Time-of-Flight (TOF) Compensation

TOF compensation is the method in which, instead of being fixed, the position of the signal gates is set dynamically relative to the surface peak position. Determining the position of the surface peak is an easy problem since this is always the largest peak. When the sound velocity in the sample is known, the location of the signal gates can be calculated for a specified depth. This method is sometimes also referred to as the *front surface follower*. An alternative implementation involves shifting entire waveforms in the time domain so that the location of all surface peaks is the same. In this implementation, the position of the signal gates remains fixed.

Per-Element Calibration

The method of per-element calibration uses the fact that for some configurations the reflection from flat-parallel defects changes similarly to the surface reflection. Assuming this relation is linear, we can divide the “signal” by the “surface” to compensate for the tilt of the transducer. Notice, for example, from figure 5.1, that in the reference system this assumption will work for angles of up to $\sim 6^\circ$. To calibrate the signals, the amplitude of the surface reflection should be detected, and the rest of the signals should be divided by this amplitude¹. Unfortunately there is no universal calibration for all the possible configurations and types of defects, but this simple method increases the stability and quality of acquired images in many cases.

¹Some special care should be taken to address the issue of small surface amplitudes to avoid division by small numbers

Tilt Correction

The goal of the tilt correction technique is similar to that of the per-element calibration—improving the angular stability. This time, however, the tilt of the transducer is obtained explicitly. Knowing the sound velocity in the immersion, we can restore the distance between the delay line and the surface of the sample for each element of the matrix from the absolute positions of surface peaks in the time domain. Assuming the surface is smooth, these distances can be used to calculate the tilt of elements. This angle together with theoretically or experimentally obtained angular dependence of the internal reflection can be used to restore the signal amplitude back to its normal value, which corresponds to 0° transducer tilt.

TOF compensation can easily be combined with both per-element calibration and tilt correction. The last two methods are designed to achieve the same goal—angular stability, using different approaches. While the per-element calibration technique is less precise, it is much easier to implement. It will also work for samples with non-flat surfaces provided, of course, the curvature is small enough to keep the local tilts at each element within the working range. The method of tilt correction, on the other hand, requires calibration before the measurement can be done and the assumptions on surface flatness (or smoothness) are much more constrained. However, one can expect the results provided by this technique to be more precise.

To illustrate these methods, a set of images has been obtained with a 52-element $\varnothing 8$ mm matrix transducer for a steel calibration sample shown in figure 5.16. The images obtained at various angles of the transducer relative to the surface are shown in figure 5.17.

We can see that using the described calibration methods the image remains stable

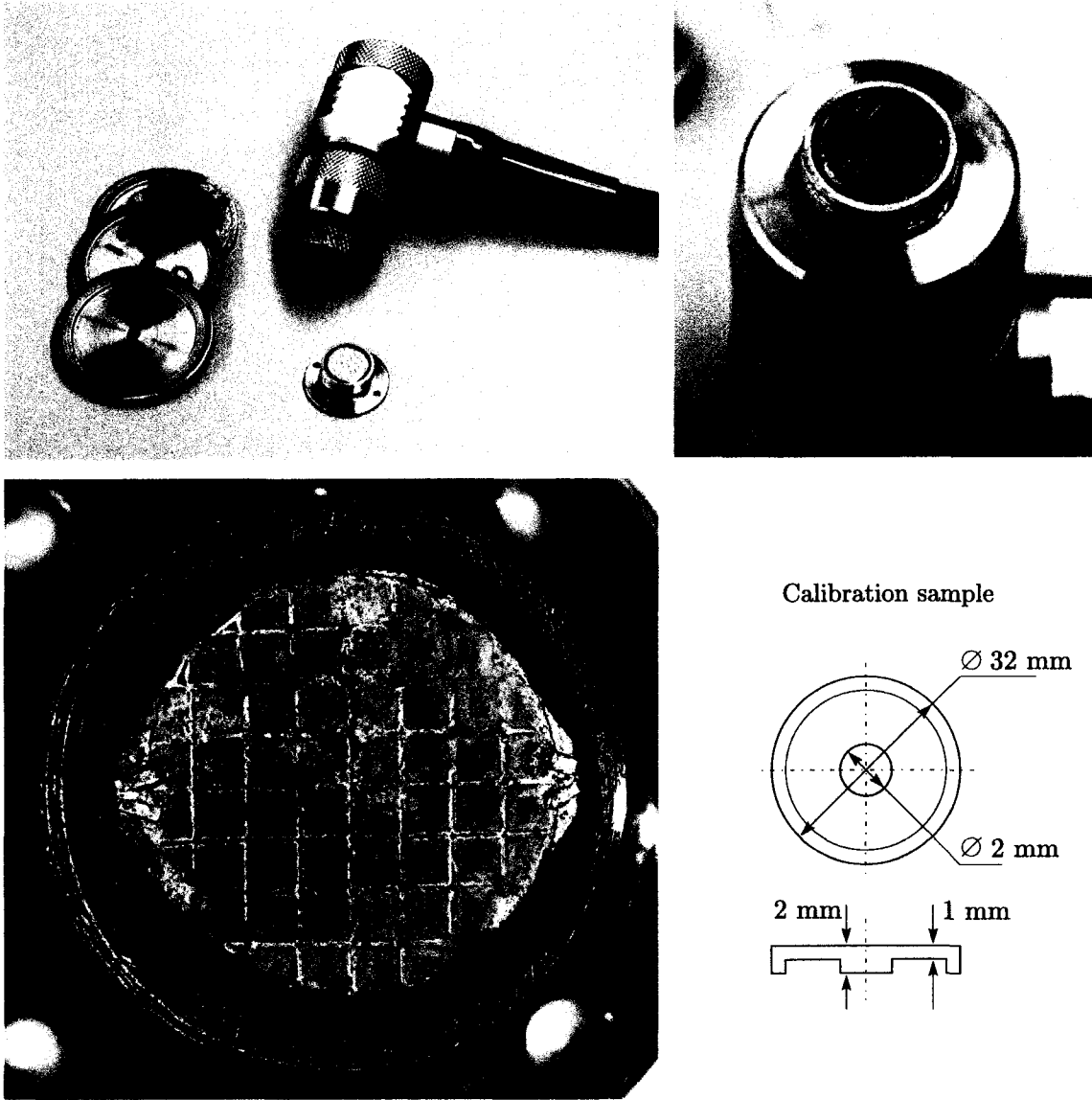


Figure 5.16. The matrix transducer and calibration samples

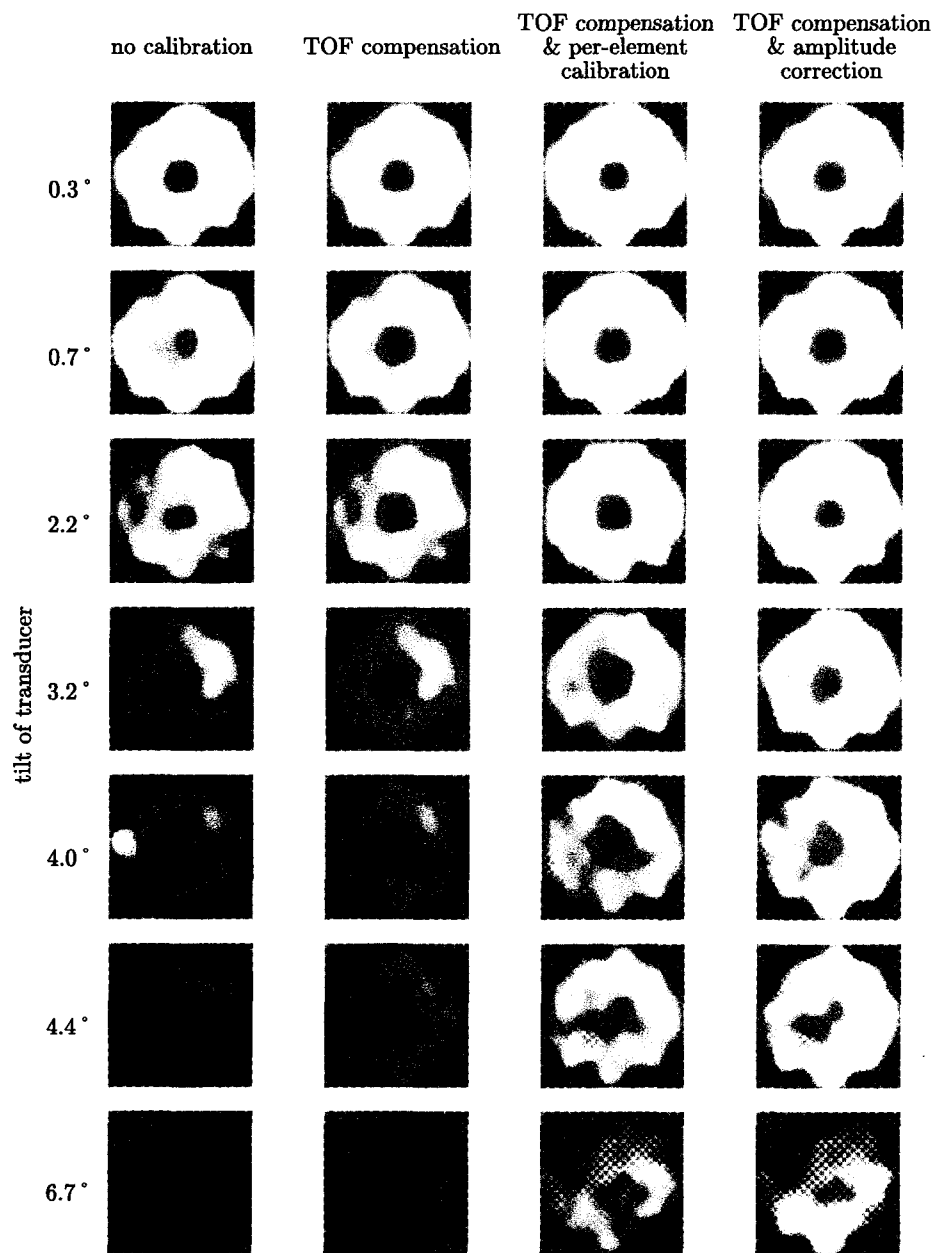


Figure 5.17. Interpolated images of calibration sample

for angles of up to 4° . This angle is mostly limited by noise levels in the system. Notice from figure 5.1 that there is not much room for improvement. Provided the better signal-to-noise ratio is achieved, this stability could probably be improved for angles of up to 6–7 degrees.

From the previous sections, we can see that the angular sensitivity is controlled by several factors, but there is always a compromise. By manufacturing transducers with smaller elements, or by decreasing the frequency we achieve better angular stability, but at the same time, signal amplitudes are lower and the image will appear more blurry due to the increased effective size of the elements (see figure 5.12 and figure 5.13). Even though it is possible to choose the size of the resampling kernel to compensate for larger effective size, the influence of increased noise level will prevent fulfilling this compensation properly. Notice also that for water column transducers the limitation on tilt should be less severe (figure 5.6).

Choosing larger elements for the array is more beneficial for deeper defects as it decreases the beam spreading and permits delivering more energy to the reflector.

Different problems require different solutions. The model developed in this work is capable of predicting the behavior of transducer elements. By studying how the signals will change in various configurations we can design the one with the best performance.

This model is also a useful tool in selecting processing methods to improve image quality, although the final tuning of these methods should probably be performed experimentally after the new matrix transducer is manufactured.

CHAPTER 6

Conclusions and Future Work

We started building the model of a single transducer element in Chapter 3 in the plane wave approximation. The reflection and transmission factors obtained in this simplified model are used in Chapter 4, when we consider a more precise model for finite size transducers and defects. We also derive the method of equivalent transformations. This method works in a paraxial approach, and permits calculating the field structure. Using the method of equivalent transformations together with the Fraunhofer approximation we can obtain the pressure at any point close to the main beam axis completely analytically at a very high speed. As the last step in building the model, we discuss a technique of estimating the response of the transducer to the reflection from an arbitrary reflector on its path. The advantage of this technique is that knowing the structure of the forward propagating wave and the location of the reflector one can estimate this response without calculating the backward propagating reflected wave. In Chapter 5 we demonstrate how these methods can be used to study transducer's performance in various situations. Finally, the image formation in 2D

array of transducers is discussed. We show what can be done to improve the quality and stability of these images.

The described model appears to be adequate to the current stage of development of the matrix transducers. However, with further improvements in materials and manufacturing processes, it can be refined to cover a wider range of applications.

One of the weakest points in the model is that it works in continuous wave approximation. From Section 5.4, we see how our continuous-wave model can be applied to different frequencies. For a known shape of the signal of the transducer, we can subdivide its frequency spectrum into several bands and superimpose the results of the modeling obtained for each frequency. However, an additional study is required to answer the question of how narrow should these bands be to provide a result with a given precision.

Another clear deficiency of the method of equivalent transformations is the assumed flatness of the elements of the array. Some modification of this method is required to accommodate for focused elements when development of such array transducers becomes feasible.

We have also chosen the piston model for each element, as well as a linear uniform sensitivity, which appears to be a good approximation, however, when building more precise models, other approximations should probably be considered.

To complete the model, the attenuation factors should also be included. The attenuation in the current setup appears to be below the detectable level, that is why it was not considered here. If necessary (for higher frequencies or materials with higher attenuation), this effect can easily be incorporated into the model.

An important direction in future work is developing criteria of applicability of this model. Currently, the only way of validating the method of equivalent transformations is comparing it with the direct Rayleigh-Sommerfeld integration, which is a time

consuming operation.

APPENDIX A

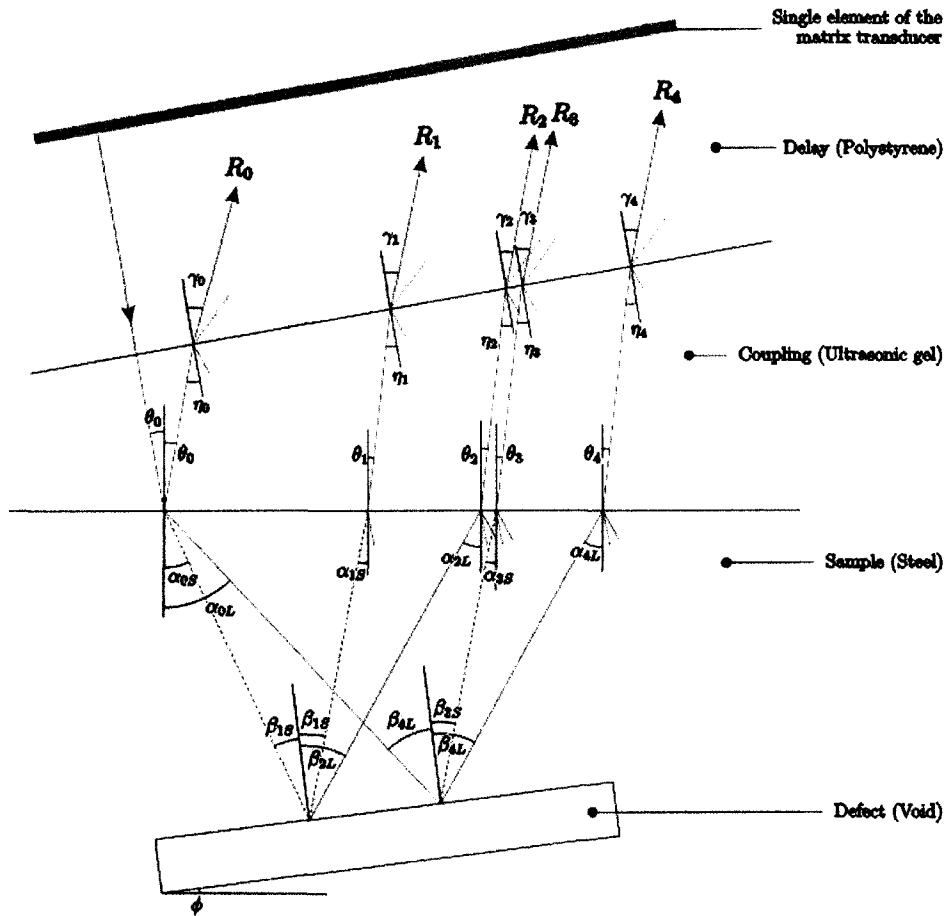
MathCAD Source for Obtaining Transmission and Reflection Factors

In this section a MathCAD source for calculating reflection and transmission factors is presented. These is the code which was used to obtain numerical data for Chapter 3. In order to compile these sources MathCAD 2000 or later version is required.

Transmission and Reflection

Media properties

Delay line (Polystyrene):	$\rho_{plst} := 1050$	$cL_{plst} := 2400$	$cS_{plst} := 1100$
Coupling (Ultrasonic gel):	$\rho_{gel} := 1300$	$c_{gel} := 1900$	
Sample (Steel):	$\rho_{stl} := 7900$	$cL_{stl} := 5900$	$cS_{stl} := 3200$



Media vector components:	$L1 := 0$	$S1 := 1$	$L2 := 2$	$S2 := 3$
Component indices in result:	$ANGL := 0$	$AMPL := 1$	$ENRG := 2$	

Reflection and refraction for a P-wave incidence (Smooth interface)

$$\text{TransferP}(\alpha, \rho_1, \rho_2, c, A_0) := \left\{ \begin{array}{l} Z_{L1} \leftarrow \rho_1 \cdot c_{L1} \\ Z_{S1} \leftarrow \rho_1 \cdot c_{S1} \\ Z_{L2} \leftarrow \rho_2 \cdot c_{L2} \\ Z_{S2} \leftarrow \rho_2 \cdot c_{S2} \\ \theta \leftarrow \text{asin}\left(\frac{c}{c_{L1}} \cdot \sin(\alpha)\right) \\ \xrightarrow{\quad} \\ X \leftarrow \frac{Z}{\cos(\theta)} \\ \cos 2\theta_{S1} \leftarrow \cos(2 \cdot \theta_{S1}) \\ \Delta_1 \leftarrow X_{L1} \cdot \cos 2\theta_{S1}^2 \\ \Delta_2 \leftarrow X_{L2} \cdot \cos(2 \cdot \theta_{S2})^2 + X_{S2} \cdot \sin(2 \cdot \theta_{S2})^2 + X_{S1} \cdot \sin(2 \cdot \theta_{S1})^2 \\ T_{L1} \leftarrow \Delta_1 - \Delta_2 \\ T_{S1} \leftarrow \frac{Z_{L1}}{\cos(\theta_{S1})} \cdot \sin(4 \cdot \theta_{S1}) \\ T_{L2} \leftarrow \frac{Z_{L1}}{\cos(\theta_{L2})} \cdot 2 \cdot \cos(2 \cdot \theta_{S2}) \cdot \cos 2\theta_{S1} \\ T_{S2} \leftarrow \frac{Z_{L1}}{\cos(\theta_{S2})} \cdot 2 \cdot \sin(2 \cdot \theta_{S2}) \\ T_{S1} \leftarrow 0 \text{ if } \text{Im}(\theta_{S1}) \neq 0 \vee |\theta_{S1}| = \frac{\pi}{2} \\ T_{L2} \leftarrow 0 \text{ if } \text{Im}(\theta_{L2}) \neq 0 \vee |\theta_{L2}| = \frac{\pi}{2} \\ T_{S2} \leftarrow 0 \text{ if } \text{Im}(\theta_{S2}) \neq 0 \vee |\theta_{S2}| = \frac{\pi}{2} \\ T \leftarrow \frac{T \cdot A_0}{\Delta_1 + \Delta_2} \\ I \leftarrow \left(\frac{\overrightarrow{(Z \cdot \cos(\theta))}}{Z_{L1} \cdot \cos(\theta_{L1})} \cdot (|T|)^2 \right) \\ \text{augment}(\text{augment}(\theta, T), I) \end{array} \right.$$

Reflection and refraction for SV-wave incidence (Smooth interface)

$$\begin{aligned}
 \text{TransferS}(\beta, \rho_1, \rho_2, c, A_0) := & \left\{ \begin{array}{l}
 Z_{L1} \leftarrow \rho_1 \cdot c_{L1} \\
 Z_{S1} \leftarrow \rho_1 \cdot c_{S1} \\
 Z_{L2} \leftarrow \rho_2 \cdot c_{L2} \\
 Z_{S2} \leftarrow \rho_2 \cdot c_{S2} \\
 \theta \leftarrow \text{asin}\left(\frac{c}{c_{S1}} \cdot \sin(\beta)\right) \\
 \xrightarrow{\quad} \\
 X \leftarrow \frac{Z}{\cos(\theta)} \\
 \Delta_1 \leftarrow X_{S1} \cdot \sin(2 \cdot \theta_{S1})^2 \\
 \Delta_2 \leftarrow X_{L1} \cdot \cos(2 \cdot \theta_{S1})^2 + X_{L2} \\
 T_{S1} \leftarrow \Delta_1 - \Delta_2 \\
 T_{L1} \leftarrow \frac{Z_{S1}}{\cos(\theta_{L1})} \cdot \sin(4 \cdot \theta_{S1}) \\
 T_{L2} \leftarrow \frac{Z_{S1}}{\cos(\theta_{L2})} \cdot 2 \cdot \sin(2 \cdot \theta_{S1}) \\
 T_{S2} \leftarrow 0 \\
 T_{L1} \leftarrow 0 \text{ if } \text{Im}(\theta_{L1}) \neq 0 \\
 T \leftarrow \frac{T \cdot A_0}{\Delta_1 + \Delta_2} \\
 I \leftarrow \left(\frac{\overrightarrow{(Z \cdot \cos(\theta))}}{\overrightarrow{Z_{S1} \cdot \cos(\theta_{S1})}} \cdot (|T|)^2 \right) \\
 \text{augment}(\text{augment}(\theta, T), I)
 \end{array} \right.
 \end{aligned}$$

Adaptive Mesh Generation

The GenMesh function generates an optimized mesh for a given function in specified range of argument values. It works similar to the Simpson's rule.

Maximum number of iterations: DMAX := 36

Recursive part of the meshing routine:

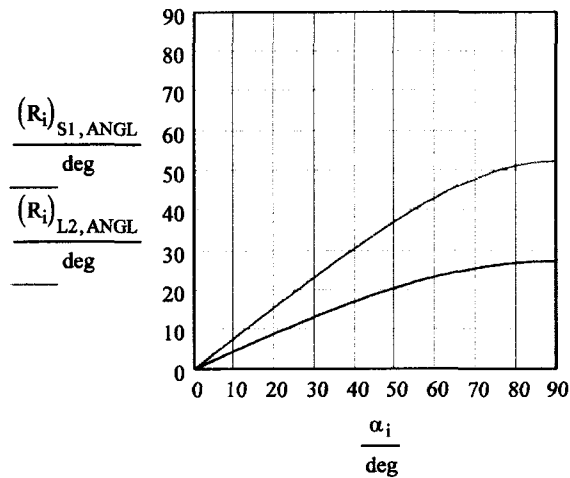
$$\begin{aligned}
 M(f, a, b, fa, fc, fb, tol, SV, N, D, A) := & \left. \begin{aligned}
 & fac \leftarrow f(0.75 \cdot a + 0.25 \cdot b) \\
 & fcb \leftarrow f(0.25 \cdot a + 0.75 \cdot b) \\
 & S1 \leftarrow \frac{b-a}{12} \cdot (fa + 4 \cdot fac + fc) \\
 & S2 \leftarrow \frac{b-a}{12} \cdot (fc + 4 \cdot fcb + fb) \\
 & \text{if } |SV - S1 - S2| > tol \wedge \text{cols}(A) < N \wedge D < DMAX \\
 & \quad \left. \begin{aligned}
 & q \leftarrow \frac{a+b}{2} \\
 & A1 \leftarrow M\left(f, a, q, fa, fac, fc, \frac{tol}{2}, S1, N, D+1, A\right) \\
 & A2 \leftarrow M\left(f, q, b, fc, fcb, fb, \frac{tol}{2}, S2, N, D+1, A1\right) \\
 & S1 \leftarrow A1_0 \\
 & S2 \leftarrow A2_0 \\
 & A \leftarrow A2_1
 \end{aligned}
 \right. \\
 & A_{0, \text{cols}(A)} \leftarrow \frac{a+b}{2} \\
 & \left(\begin{array}{c} S1 + S2 \\ A \end{array} \right)
 \end{aligned}
 \right.
 \end{aligned}$$

$$\begin{aligned}
 \text{GenMesh}(f, a, b, tol) := & \left. \begin{aligned}
 & fa \leftarrow f(a) \\
 & fb \leftarrow f(b) \\
 & fc \leftarrow f\left(\frac{a+b}{2}\right) \\
 & Q \leftarrow M\left[f, a, b, fa, fc, fb, tol, \frac{b-a}{6} \cdot (fa + 4 \cdot fc + fb), 2000, 0, (a \ b)\right]_1 \\
 & \text{sort}(Q^T)
 \end{aligned}
 \right.
 \end{aligned}$$

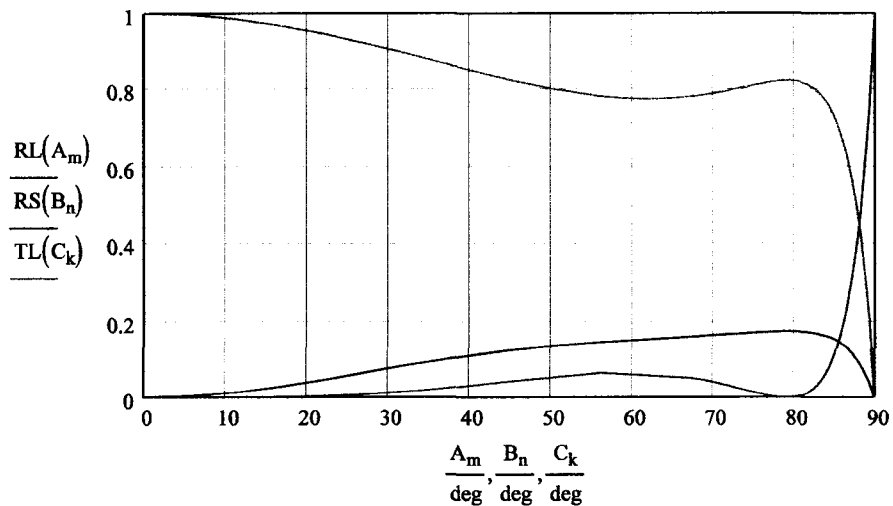
Solid-Fluid Interface #1 (P-Wave) Forward propagation from polysterene into gel

$$\rho_1 := \rho_{\text{plst}} \quad c_{L1} := c_{L_{\text{plst}}} \quad c_{S1} := c_{S_{\text{plst}}} \quad \rho_2 := \rho_{\text{gel}} \quad c_{L2} := c_{\text{gel}} \quad c_{S2} := 0$$

$$i := 0..90 \quad \alpha_i := i \cdot \frac{\pi}{180} \quad R_i := \text{TransferP}(\alpha_i, \rho_1, \rho_2, c, 1)$$



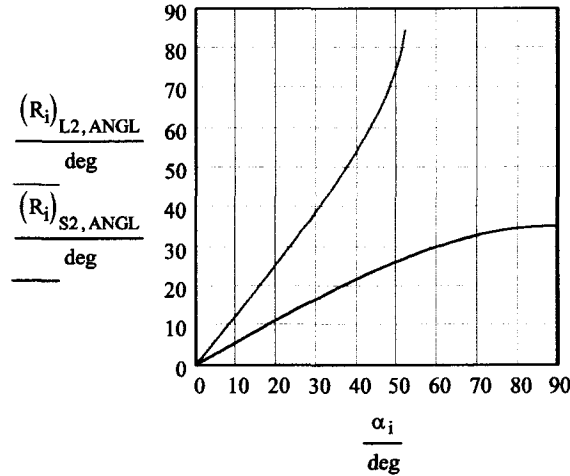
$$\begin{aligned} \text{RL}(\alpha) &:= \text{TransferP}(\alpha, \rho_1, \rho_2, c, 1)_{L1, \text{ENRG}} \quad A := \text{GenMesh}\left(\text{RL}, 0, \frac{\pi}{2}, 10^{-5}\right) \quad m := 0.. \text{length}(A) \\ \text{RS}(\alpha) &:= \text{TransferP}(\alpha, \rho_1, \rho_2, c, 1)_{S1, \text{ENRG}} \quad B := \text{GenMesh}\left(\text{RS}, 0, \frac{\pi}{2}, 10^{-5}\right) \quad n := 0.. \text{length}(B) \\ \text{TL}(\alpha) &:= \text{TransferP}(\alpha, \rho_1, \rho_2, c, 1)_{L2, \text{ENRG}} \quad C := \text{GenMesh}\left(\text{TL}, 0, \frac{\pi}{2}, 10^{-5}\right) \quad k := 0.. \text{length}(C) \end{aligned}$$



Fluid-Solid Interface #1 Backward propagation from gel into polystyrene

$$\rho_1 := \rho_{\text{gel}} \quad c_{L1} := c_{\text{gel}} \quad c_{S1} := 0 \quad \rho_2 := \rho_{\text{plst}} \quad c_{L2} := c_{L_{\text{plst}}} \quad c_{S2} := c_{S_{\text{plst}}}$$

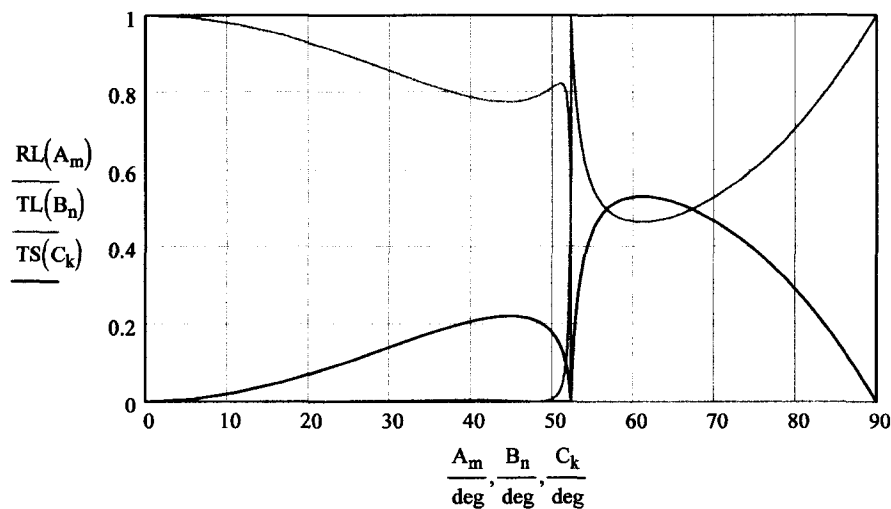
$$i := 0..90 \quad \alpha_i := i \cdot \frac{\pi}{180} \quad R_i := \text{TransferP}(\alpha_i, \rho_1, \rho_2, c, 1)$$



Critical angles:

$$\text{asin}\left(\frac{c_{L1}}{c_{L2}}\right) = 52.342 \text{ deg}$$

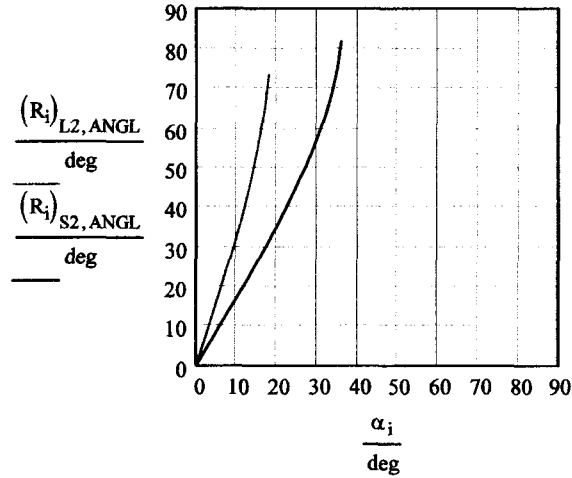
$$\begin{aligned} RL(\alpha) &:= \text{TransferP}(\alpha, \rho_1, \rho_2, c, 1)_{L1, ENRG} \quad A := \text{GenMesh}\left(RL, 0, \frac{\pi}{2}, 10^{-5}\right) \quad m := 0.. \text{length}(A) \\ TL(\alpha) &:= \text{TransferP}(\alpha, \rho_1, \rho_2, c, 1)_{L2, ENRG} \quad B := \text{GenMesh}\left(TL, 0, \frac{\pi}{2}, 10^{-4}\right) \quad n := 0.. \text{length}(B) \\ TS(\alpha) &:= \text{TransferP}(\alpha, \rho_1, \rho_2, c, 1)_{S2, ENRG} \quad C := \text{GenMesh}\left(TS, 0, \frac{\pi}{2}, 10^{-5}\right) \quad k := 0.. \text{length}(C) \end{aligned}$$



Fluid-Solid Interface #2 Forward propagation from gel into steel

$$\rho_1 := \rho_{gel} \quad c_{L1} := c_{gel} \quad c_{S1} := 0 \quad \rho_2 := \rho_{stl} \quad c_{L2} := c_{L_{stl}} \quad c_{S2} := c_{S_{stl}}$$

$$i := 0..90 \quad \alpha_i := i \cdot \frac{\pi}{180} \quad R_i := \text{TransferP}(\alpha_i, \rho_1, \rho_2, c, 1)$$



Critical angles:

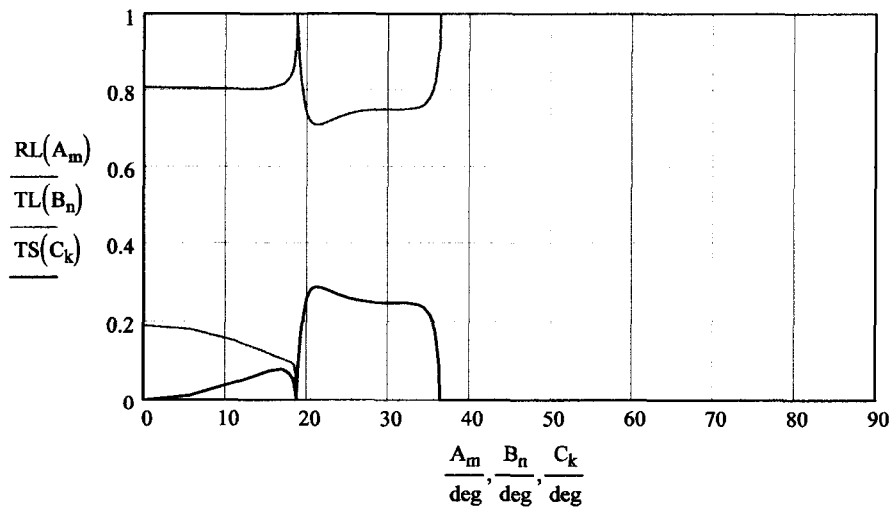
$$\text{asin}\left(\frac{c_{L1}}{c_{L2}}\right) = 18.786 \text{ deg}$$

$$\text{asin}\left(\frac{c_{L1}}{c_{S2}}\right) = 36.424 \text{ deg}$$

$$RL(\alpha) := \text{TransferP}(\alpha, \rho_1, \rho_2, c, 1)_{L1, ENRG} \quad A := \text{GenMesh}\left(RL, 0, \frac{\pi}{2}, 10^{-4}\right) \quad m := 0.. \text{length}(A)$$

$$TL(\alpha) := \text{TransferP}(\alpha, \rho_1, \rho_2, c, 1)_{L2, ENRG} \quad B := \text{GenMesh}\left(TL, 0, \frac{\pi}{2}, 10^{-4}\right) \quad n := 0.. \text{length}(B)$$

$$TS(\alpha) := \text{TransferP}(\alpha, \rho_1, \rho_2, c, 1)_{S2, ENRG} \quad C := \text{GenMesh}\left(TS, 0, \frac{\pi}{2}, 10^{-4}\right) \quad k := 0.. \text{length}(C)$$

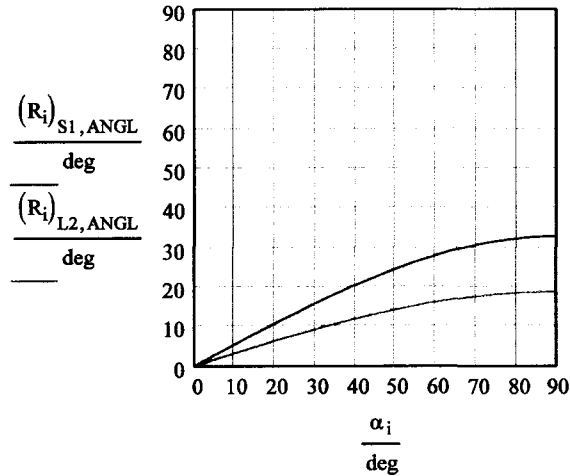


Solid-Fluid Interface #2 (P-Wave)

Backward propagation from steel into gel

$$\rho_1 := \rho_{\text{stl}} \quad c_{L1} := c_{L_{\text{stl}}} \quad c_{S1} := c_{S_{\text{stl}}} \quad \rho_2 := \rho_{\text{gel}} \quad c_{L2} := c_{\text{gel}} \quad c_{S2} := 0$$

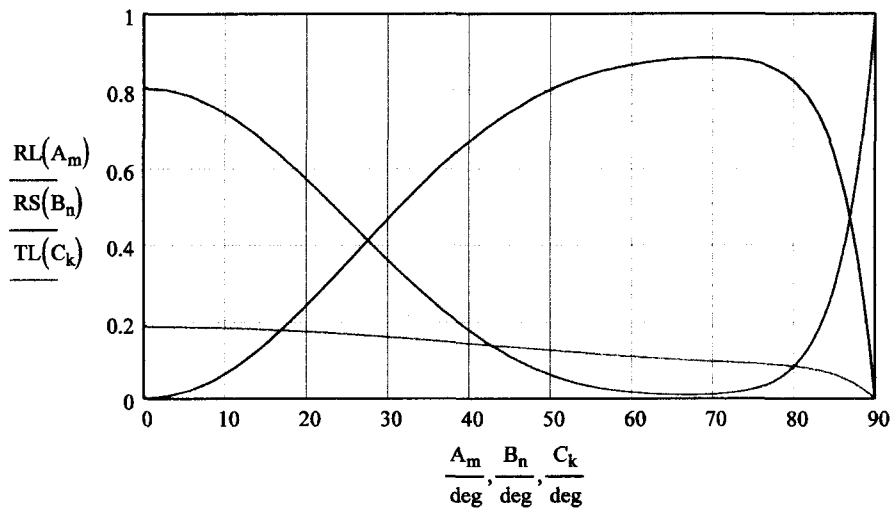
$$i := 0..90 \quad \alpha_i := i \cdot \frac{\pi}{180} \quad R_i := \text{TransferP}(\alpha_i, \rho_1, \rho_2, c, 1)$$



$$RL(\alpha) := \text{TransferP}(\alpha, \rho_1, \rho_2, c, 1)_{L1, \text{ENRG}} \quad A := \text{GenMesh}\left(RL, 0, \frac{\pi}{2}, 10^{-5} \right) \quad m := 0.. \text{length}(A)$$

$$RS(\alpha) := \text{TransferP}(\alpha, \rho_1, \rho_2, c, 1)_{S1, \text{ENRG}} \quad B := \text{GenMesh}\left(RS, 0, \frac{\pi}{2}, 10^{-5} \right) \quad n := 0.. \text{length}(B)$$

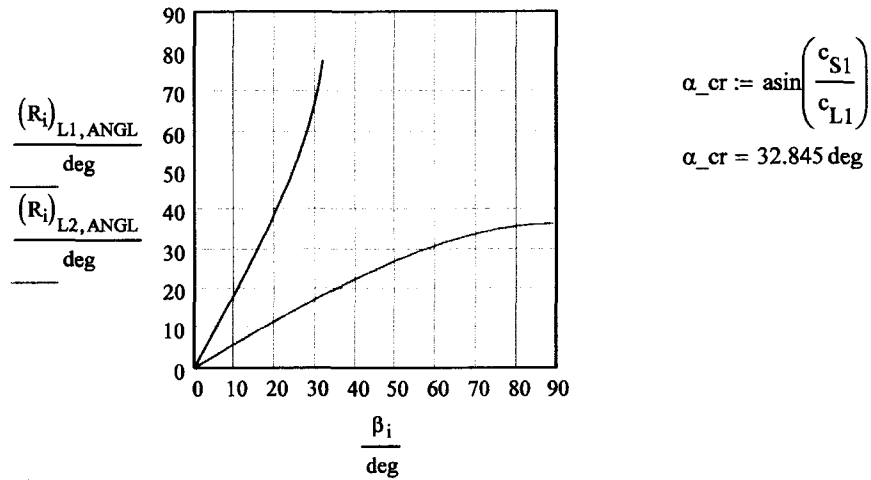
$$TL(\alpha) := \text{TransferP}(\alpha, \rho_1, \rho_2, c, 1)_{L2, \text{ENRG}} \quad C := \text{GenMesh}\left(TL, 0, \frac{\pi}{2}, 10^{-5} \right) \quad k := 0.. \text{length}(C)$$



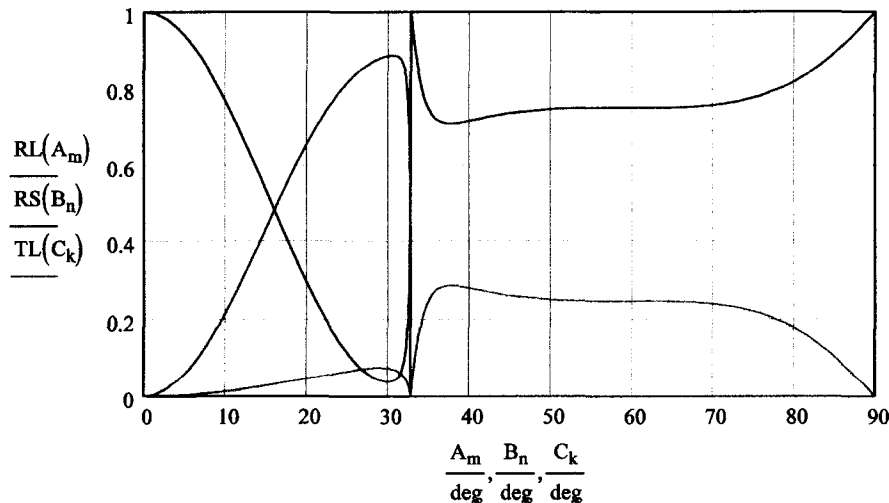
Solid-Fluid Interface #2 (SV-Wave) Backward propagation from steel into gel

$$\rho_1 := \rho_{\text{stl}} \quad c_{L1} := c_{L\text{-stl}} \quad c_{S1} := c_{S\text{-stl}} \quad \rho_2 := \rho_{\text{gel}} \quad c_{L2} := c_{\text{gel}} \quad c_{S2} := 0$$

$$i := 0..89 \quad \beta_i := i \cdot \frac{\pi}{180} \quad R_i := \text{TransferS}(\beta_i, \rho_1, \rho_2, c, 1)$$



$$\begin{aligned} \text{RL}(\beta) &:= \text{TransferS}(\beta, \rho_1, \rho_2, c, 1)_{L1, \text{ENRG}} \quad \text{A} := \text{GenMesh}\left(\text{RL}, 0, \frac{\pi}{2}, 10^{-5}\right) \quad m := 0.. \text{length}(\text{A}) \\ \text{RS}(\beta) &:= \text{TransferS}(\beta, \rho_1, \rho_2, c, 1)_{S1, \text{ENRG}} \quad \text{B} := \text{GenMesh}\left(\text{RS}, 0, \frac{\pi}{2}, 10^{-5}\right) \quad n := 0.. \text{length}(\text{B}) \\ \text{TL}(\beta) &:= \text{TransferS}(\beta, \rho_1, \rho_2, c, 1)_{L2, \text{ENRG}} \quad \text{C} := \text{GenMesh}\left(\text{TL}, 0, \frac{\pi}{2}, 10^{-5}\right) \quad k := 0.. \text{length}(\text{C}) \end{aligned}$$

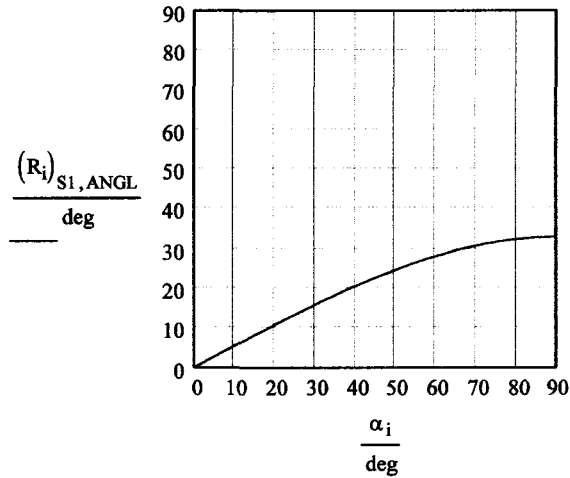


Reflection in a Solid 3 (P-Wave)

Reflection from a void defect in steel

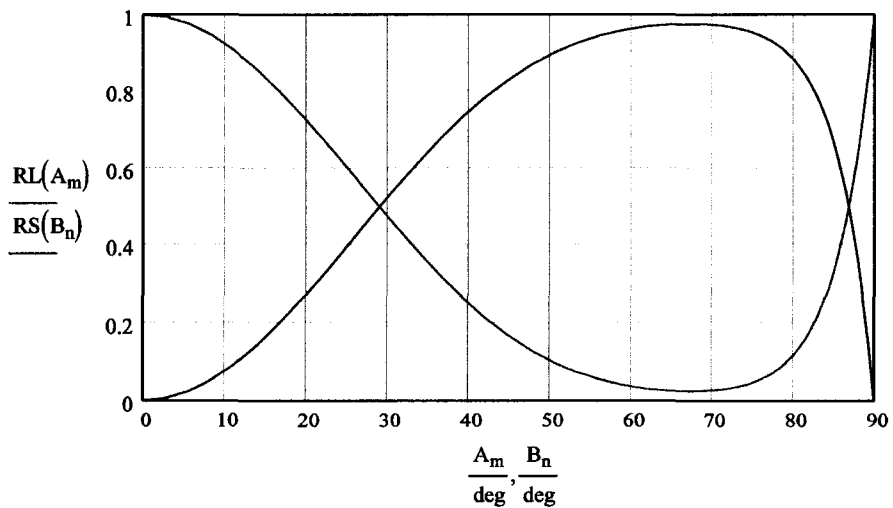
$$\rho_1 := \rho_{\text{stl}} \quad c_{L1} := c_{L_{\text{stl}}} \quad c_{S1} := c_{S_{\text{stl}}} \quad \rho_2 := 1 \quad c_{L2} := 1 \quad c_{S2} := 0$$

$$i := 0..90 \quad \alpha_i := i \cdot \frac{\pi}{180} \quad R_i := \text{TransferP}(\alpha_i, \rho_1, \rho_2, c, 1)$$



$$RL(\alpha) := \text{TransferP}(\alpha, \rho_1, \rho_2, c, 1)_{L1,ENRG} \quad A := \text{GenMesh}\left(RL, 0, \frac{\pi}{2}, 10^{-5} \right) \quad m := 0.. \text{length}(A)$$

$$RS(\alpha) := \text{TransferP}(\alpha, \rho_1, \rho_2, c, 1)_{S1,ENRG} \quad B := \text{GenMesh}\left(RS, 0, \frac{\pi}{2}, 10^{-5} \right) \quad n := 0.. \text{length}(B)$$

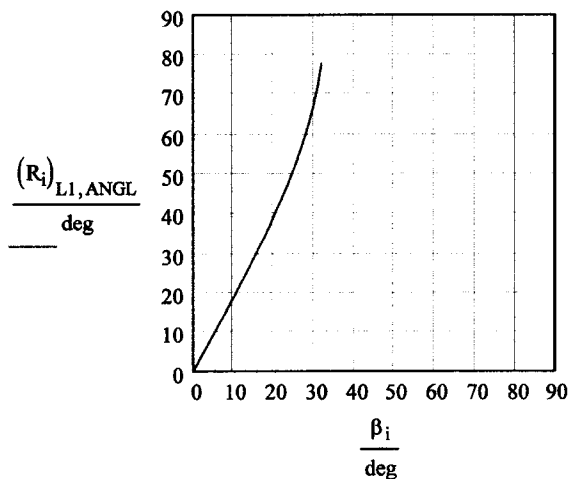


Reflection in a Solid 3 (SV-Wave)

Reflection from a void defect in steel

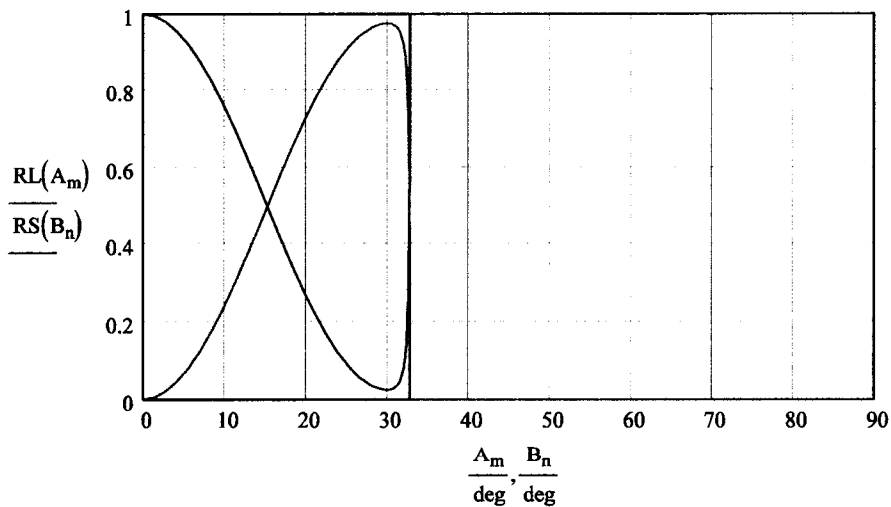
$$\rho_1 := \rho_{\text{stl}} \quad c_{L1} := c_{L_{\text{stl}}} \quad c_{S1} := c_{S_{\text{stl}}} \quad \rho_2 := 1 \quad c_{L2} := 1 \quad c_{S2} := 0$$

$$i := 0..90 \quad \beta_i := i \cdot \frac{\pi}{180} \quad R_i := \text{TransferS}(\beta_i, \rho_1, \rho_2, c, 1)$$



$$RL(\beta) := \text{TransferS}(\beta, \rho_1, \rho_2, c, 1)_{L1,ENRG} \quad A := \text{GenMesh}\left(RL, 0, \frac{\pi}{2}, 10^{-5} \right)_{m := 0..length(A)}$$

$$RS(\beta) := \text{TransferS}(\beta, \rho_1, \rho_2, c, 1)_{S1,ENRG} \quad B := \text{GenMesh}\left(RS, 0, \frac{\pi}{2}, 10^{-5} \right)_{n := 0..length(B)}$$



Multiple Interfaces

$$\text{Initial angle: } \theta \quad \text{Angle of the defect: } \phi := 0 \cdot \frac{\pi}{180}$$

Delay–Immersion:

$$\text{Delay:} \quad \rho_1 := \rho_{\text{plst}} \quad c_{L1} := c_{L_{\text{plst}}} \quad c_{S1} := c_{S_{\text{plst}}}$$

$$\text{Immersion:} \quad \rho_2 := \rho_{\text{gel}} \quad c_{L2} := c_{\text{gel}} \quad c_{S2} := 0$$

$$A00 := \text{TransferP}(0, \rho_1, \rho_2, c, 1)_{L2, \text{AMPL}}$$

Immersion–Sample:

$$\text{Immersion:} \quad \rho_1 := \rho_{\text{gel}} \quad c_{L1} := c_{\text{gel}} \quad c_{S1} := 0$$

$$\text{Sample:} \quad \rho_2 := \rho_{\text{stl}} \quad c_{L2} := c_{L_{\text{stl}}} \quad c_{S2} := c_{S_{\text{stl}}}$$

$$\alpha_{0L}(\theta) := \text{asin}\left(\frac{c_{L2}}{c_{L1}} \sin(\theta)\right)$$

$$\alpha_{0S}(\theta) := \text{asin}\left(\frac{c_{S2}}{c_{L1}} \sin(\theta)\right)$$

$$R\sigma_0(\theta) := \text{TransferP}(\theta, \rho_1, \rho_2, c, A00)_{L1, \text{AMPL}} \quad (\text{Reflection from sample surface})$$

$$A0L(\theta) := \text{TransferP}(\theta, \rho_1, \rho_2, c, A00)_{L2, \text{AMPL}}$$

$$A0S(\theta) := \text{TransferP}(\theta, \rho_1, \rho_2, c, A00)_{S2, \text{AMPL}}$$

Reflection from the defect:

$$\text{Sample:} \quad \rho_1 := \rho_{\text{stl}} \quad c_{L1} := c_{L_{\text{stl}}} \quad c_{S1} := c_{S_{\text{stl}}}$$

$$\text{Void defect:} \quad \rho_2 := 1 \quad c_{L2} := 1 \quad c_{S2} := 0$$

$$\beta_{1S}(\theta, \phi) := \alpha_{0S}(\theta) - \phi$$

$$\beta_{4L}(\theta, \phi) := \alpha_{0L}(\theta) - \phi$$

$$\beta_{2L}(\theta, \phi) := \text{asin}\left(\frac{c_{L1}}{c_{S1}} \sin(\beta_{1S}(\theta, \phi))\right)$$

$$\beta_{3S}(\theta, \phi) := \text{asin}\left(\frac{c_{S1}}{c_{L1}} \sin(\beta_{4L}(\theta, \phi))\right)$$

$$A1S(\theta, \phi) := \text{TransferS}(\beta_{1S}(\theta, \phi), \rho_1, \rho_2, c, A0S(\theta))_{S1, \text{AMPL}}$$

$$A2L(\theta, \phi) := \text{TransferS}(\beta_{1S}(\theta, \phi), \rho_1, \rho_2, c, A0S(\theta))_{L1, \text{AMPL}}$$

$$A3S(\theta, \phi) := \text{TransferP}(\beta_{4L}(\theta, \phi), \rho_1, \rho_2, c, A0L(\theta))_{S1, \text{AMPL}}$$

$$A4L(\theta, \phi) := \text{TransferP}(\beta_{4L}(\theta, \phi), \rho_1, \rho_2, c, A0L(\theta))_{L1, \text{AMPL}}$$

Sample–Immersion:

$$\text{Sample: } \rho_1 := \rho_{\text{stl}} \quad c_{L1} := c_{L_{\text{stl}}} \quad c_{S1} := c_{S_{\text{stl}}}$$

$$\text{Immersion: } \rho_2 := \rho_{\text{gel}} \quad c_{L2} := c_{\text{gel}} \quad c_{S2} := 0$$

$$\alpha_1 S(\theta, \phi) := \beta_1 S(\theta, \phi) - \phi \quad \alpha_2 L(\theta, \phi) := \beta_2 L(\theta, \phi) - \phi$$

$$\alpha_3 S(\theta, \phi) := \beta_3 S(\theta, \phi) - \phi \quad \alpha_4 L(\theta, \phi) := \beta_4 L(\theta, \phi) - \phi$$

$$\theta_1(\theta, \phi) := \text{asin}\left(\frac{c_{L2}}{c_{S1}} \sin(\alpha_1 S(\theta, \phi))\right) \quad \theta_2(\theta, \phi) := \text{asin}\left(\frac{c_{L2}}{c_{L1}} \sin(\alpha_2 L(\theta, \phi))\right)$$

$$\theta_3(\theta, \phi) := \text{asin}\left(\frac{c_{L2}}{c_{S1}} \sin(\alpha_3 S(\theta, \phi))\right) \quad \theta_4(\theta, \phi) := \text{asin}\left(\frac{c_{L2}}{c_{L1}} \sin(\alpha_4 L(\theta, \phi))\right)$$

$$R\sigma_1(\theta, \phi) := \text{TransferS}(\alpha_1 S(\theta, \phi), \rho_1, \rho_2, c, A_1 S(\theta, \phi))_{L2, \text{AMPL}}$$

$$R\sigma_2(\theta, \phi) := \text{TransferP}(\alpha_2 L(\theta, \phi), \rho_1, \rho_2, c, A_2 L(\theta, \phi))_{L2, \text{AMPL}}$$

$$R\sigma_3(\theta, \phi) := \text{TransferS}(\alpha_3 S(\theta, \phi), \rho_1, \rho_2, c, A_3 S(\theta, \phi))_{L2, \text{AMPL}}$$

$$R\sigma_4(\theta, \phi) := \text{TransferP}(\alpha_4 L(\theta, \phi), \rho_1, \rho_2, c, A_4 L(\theta, \phi))_{L2, \text{AMPL}}$$

Immersion–Delay:

$$\text{Immersion: } \rho_1 := \rho_{\text{gel}} \quad c_{L1} := c_{\text{gel}} \quad c_{S1} := 0$$

$$\text{Delay: } \rho_2 := \rho_{\text{plst}} \quad c_{L2} := c_{L_{\text{plst}}} \quad c_{S2} := c_{S_{\text{plst}}}$$

$$\eta_0(\theta, \phi) := \theta + \theta \quad \eta_1(\theta, \phi) := \theta_1(\theta, \phi) + \theta \quad \eta_2(\theta, \phi) := \theta_2(\theta, \phi) + \theta$$

$$\eta_3(\theta, \phi) := \theta_3(\theta, \phi) + \theta \quad \eta_4(\theta, \phi) := \theta_4(\theta, \phi) + \theta \quad \gamma_0(\theta, \phi) := \text{asin}\left(\frac{c_{L2}}{c_{L1}} \sin(\eta_0(\theta, \phi))\right)$$

$$\gamma_1(\theta, \phi) := \text{asin}\left(\frac{c_{L2}}{c_{L1}} \sin(\eta_1(\theta, \phi))\right) \quad \gamma_2(\theta, \phi) := \text{asin}\left(\frac{c_{L2}}{c_{L1}} \sin(\eta_2(\theta, \phi))\right)$$

$$\gamma_3(\theta, \phi) := \text{asin}\left(\frac{c_{L2}}{c_{L1}} \sin(\eta_3(\theta, \phi))\right) \quad \gamma_4(\theta, \phi) := \text{asin}\left(\frac{c_{L2}}{c_{L1}} \sin(\eta_4(\theta, \phi))\right)$$

$$R_0(\theta) := \left(|\text{TransferP}(\gamma_0(\theta, \phi), \rho_1, \rho_2, c, R\sigma_0(\theta))_{L2, \text{ENRG}}| \right)^1$$

$$R_1(\theta) := \left(|\text{TransferP}(\gamma_1(\theta, \phi), \rho_1, \rho_2, c, R\sigma_1(\theta, \phi))_{L2, \text{ENRG}}| \right)^1$$

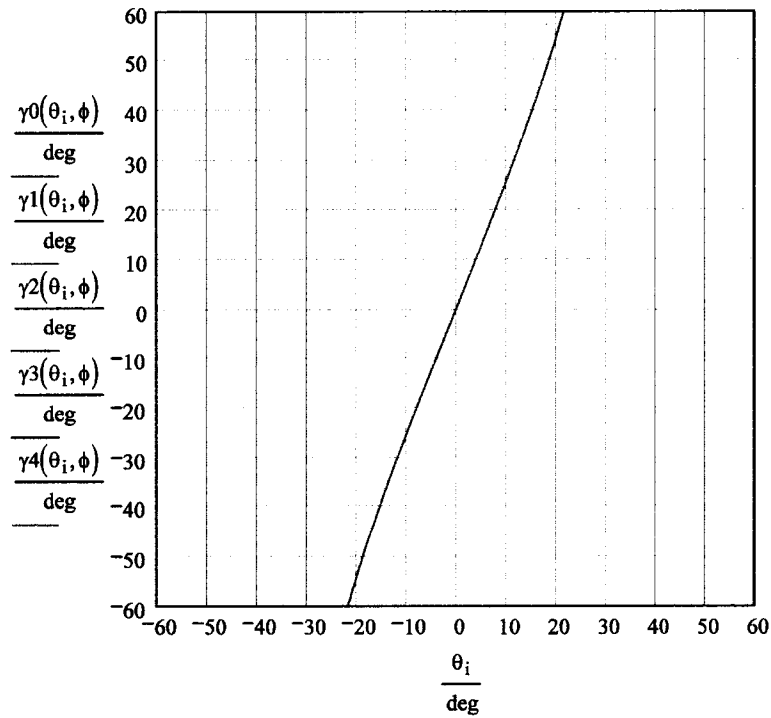
$$R_2(\theta) := \left(|\text{TransferP}(\gamma_2(\theta, \phi), \rho_1, \rho_2, c, R\sigma_2(\theta, \phi))_{L2, \text{ENRG}}| \right)^1$$

$$R_3(\theta) := \left(|\text{TransferP}(\gamma_3(\theta, \phi), \rho_1, \rho_2, c, R\sigma_3(\theta, \phi))_{L2, \text{ENRG}}| \right)^1$$

$$R_4(\theta) := \left(|\text{TransferP}(\gamma_4(\theta, \phi), \rho_1, \rho_2, c, R\sigma_4(\theta, \phi))_{L2, \text{ENRG}}| \right)^1$$

Numerical calculations:

$$i := 0..60 \quad \theta_i := \left[(i - 30) \cdot \frac{\pi}{90} \right]$$



$$\Theta := \frac{\pi}{6} \quad E := 10^{-7}$$

$$x0 := \text{GenMesh}(R0, -\Theta, \Theta, E) \quad n0 := 0.. \text{length}(x0)$$

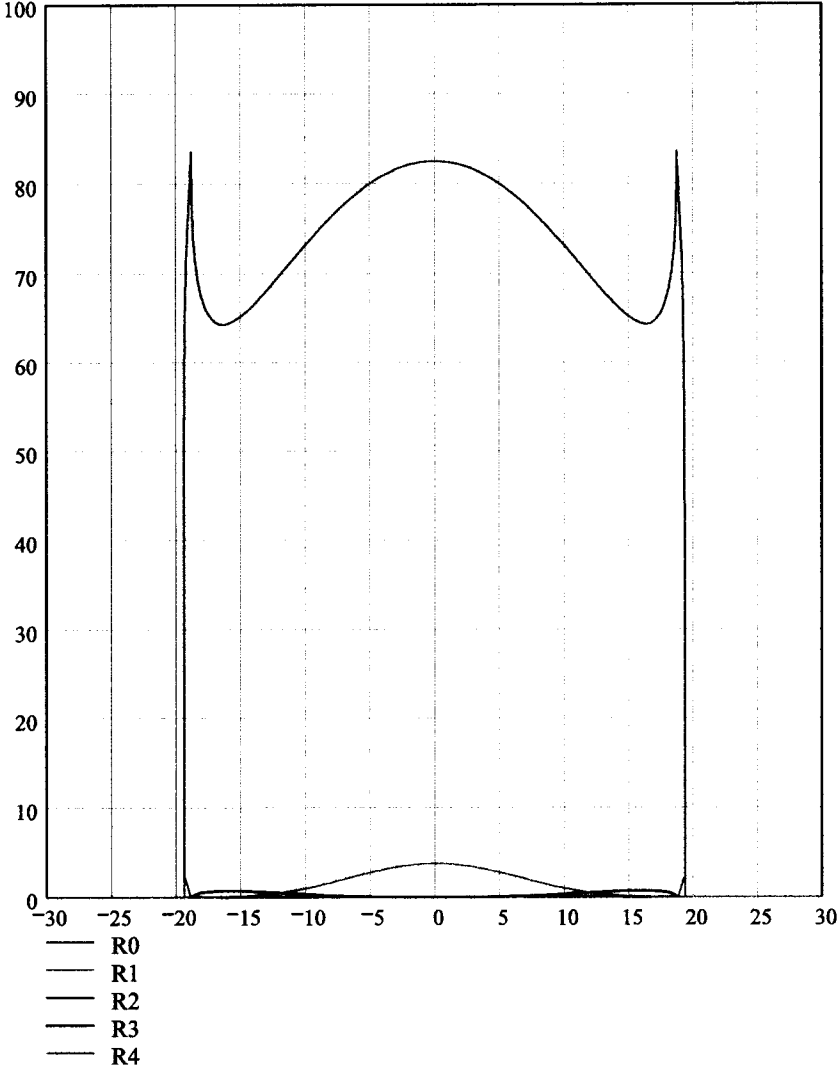
$$x1 := \text{GenMesh}(R1, -\Theta, \Theta, E) \quad n1 := 0.. \text{length}(x1)$$

$$x2 := \text{GenMesh}(R2, -\Theta, \Theta, E) \quad n2 := 0.. \text{length}(x2)$$

$$x3 := \text{GenMesh}(R3, -\Theta, \Theta, E) \quad n3 := 0.. \text{length}(x3)$$

$$x4 := \text{GenMesh}(R4, -\Theta, \Theta, E) \quad n4 := 0.. \text{length}(x4)$$

$\phi = 0 \text{ deg}$



$$\phi := 0\text{deg}$$

$$R1(\theta) := \left(\left| \text{TransferP}(\gamma1(\theta, \phi), \rho1, \rho2, c, R\sigma1(\theta, \phi))_{L2, \text{ENRG}} \right| \right)^1$$

$$R2(\theta) := \left(\left| \text{TransferP}(\gamma2(\theta, \phi), \rho1, \rho2, c, R\sigma2(\theta, \phi))_{L2, \text{ENRG}} \right| \right)^1$$

$$R3(\theta) := \left(\left| \text{TransferP}(\gamma3(\theta, \phi), \rho1, \rho2, c, R\sigma3(\theta, \phi))_{L2, \text{ENRG}} \right| \right)^1$$

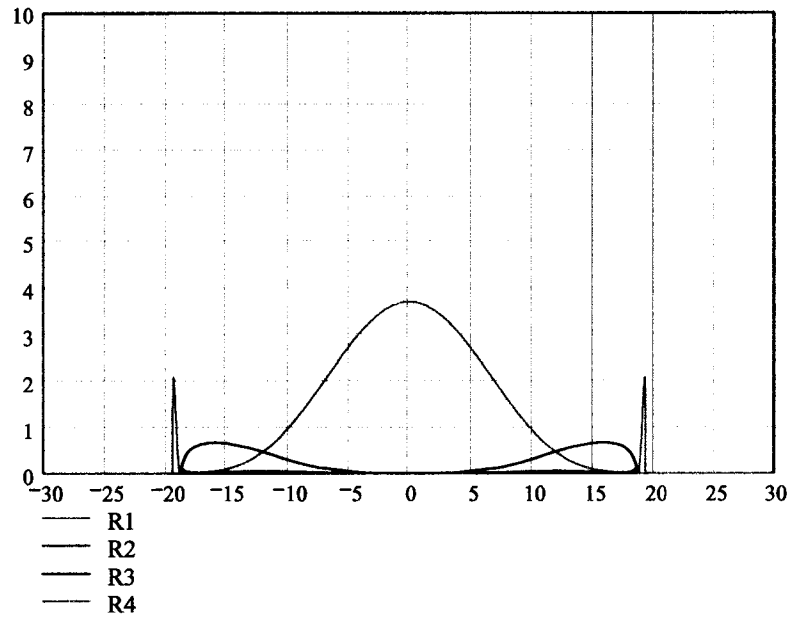
$$R4(\theta) := \left(\left| \text{TransferP}(\gamma4(\theta, \phi), \rho1, \rho2, c, R\sigma4(\theta, \phi))_{L2, \text{ENRG}} \right| \right)^1$$

$$x1 := \text{GenMesh}(R1, -\Theta, \Theta, E) \quad n1 := 0 \dots \text{length}(x1)$$

$$x2 := \text{GenMesh}(R2, -\Theta, \Theta, E) \quad n2 := 0 \dots \text{length}(x2)$$

$$x3 := \text{GenMesh}(R3, -\Theta, \Theta, E) \quad n3 := 0 \dots \text{length}(x3)$$

$$x4 := \text{GenMesh}(R4, -\Theta, \Theta, E) \quad n4 := 0 \dots \text{length}(x4)$$



$\phi := 20\text{deg}$

$$R1(\theta) := \left(\left| \text{TransferP}(\gamma1(\theta, \phi), \rho1, \rho2, c, R\sigma1(\theta, \phi))_{L2, \text{ENRG}} \right| \right)^1$$

$$R2(\theta) := \left(\left| \text{TransferP}(\gamma2(\theta, \phi), \rho1, \rho2, c, R\sigma2(\theta, \phi))_{L2, \text{ENRG}} \right| \right)^1$$

$$R3(\theta) := \left(\left| \text{TransferP}(\gamma3(\theta, \phi), \rho1, \rho2, c, R\sigma3(\theta, \phi))_{L2, \text{ENRG}} \right| \right)^1$$

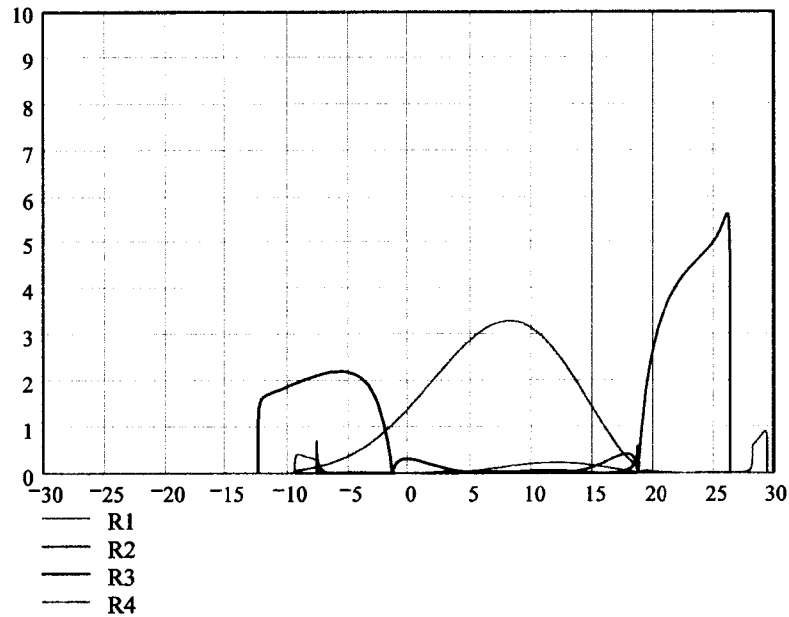
$$R4(\theta) := \left(\left| \text{TransferP}(\gamma4(\theta, \phi), \rho1, \rho2, c, R\sigma4(\theta, \phi))_{L2, \text{ENRG}} \right| \right)^1$$

$x1 := \text{GenMesh}(R1, -\Theta, \Theta, E) \quad n1 := 0 \dots \text{length}(x1)$

$x2 := \text{GenMesh}(R2, -\Theta, \Theta, E) \quad n2 := 0 \dots \text{length}(x2)$

$x3 := \text{GenMesh}(R3, -\Theta, \Theta, E) \quad n3 := 0 \dots \text{length}(x3)$

$x4 := \text{GenMesh}(R4, -\Theta, \Theta, E) \quad n4 := 0 \dots \text{length}(x4)$

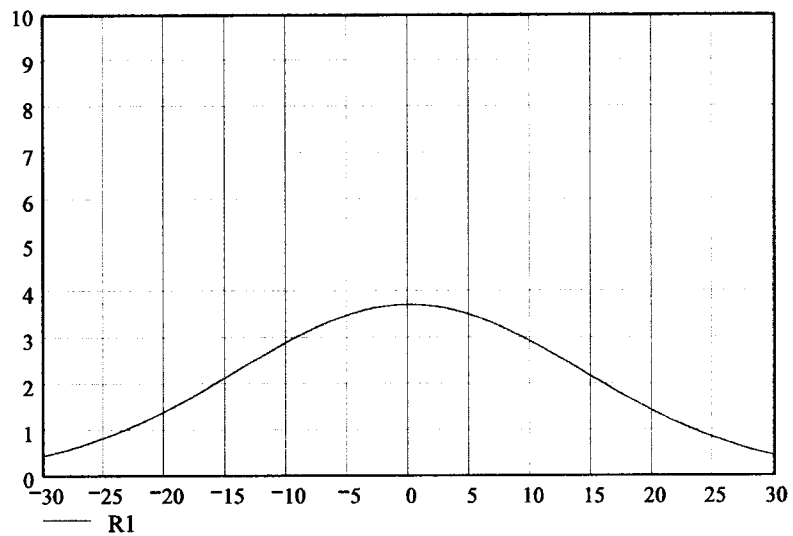


$\theta := 0\text{deg}$ $\Phi := 30\text{deg}$

$$R(\phi) := \left(\left| \text{TransferP}(\gamma_4(\theta, \phi), \rho_1, \rho_2, c, R\sigma_4(\theta, \phi))_{L2, \text{ENRG}} \right| \right)^1$$

$x := \text{GenMesh}(R, -\Phi, \Phi, E)$

$n := 0 .. \text{length}(x)$



APPENDIX B

Obtaining Angle of Incidence from Discrete Phase Values

Consider an interface specified as a rectangular mesh $\mathbf{m}_{i,j}$ where each cell size is $a \times a$:

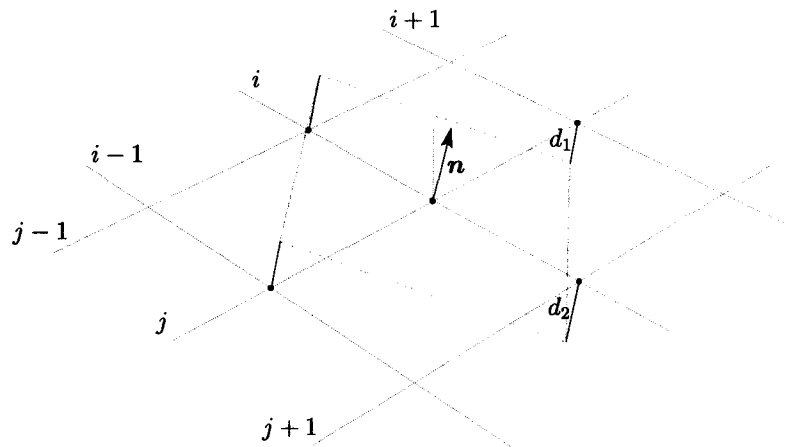


Figure B.1. Phase delays on a rectangular grid

At the moment when the locally flat wavefront crosses a point at $\mathbf{m}_{i,j}$, the distances from mesh vertices at $\mathbf{m}_{i+1,j}$ and $\mathbf{m}_{i,j+1}$ to the same wavefront, correspondingly, are:

$$d_1 = (\phi_{i+1,j} - \phi_{i,j})/k \quad \text{and} \quad d_2 = (\phi_{i,j+1} - \phi_{i,j})/k. \quad (\text{B.1})$$

To determine the direction of the wavefront normal, let's choose a couple of vectors in the wavefront plane:

$$\mathbf{p} = \begin{bmatrix} a \\ 0 \\ z_1 \end{bmatrix} \quad \text{and} \quad \mathbf{q} = \begin{bmatrix} 0 \\ a \\ z_2 \end{bmatrix}, \quad (\text{B.2})$$

where

$$z_1 = \frac{d_1}{\sqrt{1 - d_1^2/a^2}} \quad \text{and} \quad z_2 = \frac{d_2}{\sqrt{1 - d_2^2/a^2}} \quad (\text{B.3})$$

Now the direction of wave propagation can be obtained as

$$\mathbf{n} = \frac{\mathbf{p} \times \mathbf{q}}{|\mathbf{p} \times \mathbf{q}|}. \quad (\text{B.4})$$

Finally, for the vertical component of this normal:

$$n_z = \cos \theta = \frac{a^2}{\sqrt{a^2 z_1^2 + a^2 z_2^2 + a^4}} = \left[\frac{d_1^2}{a^2 - d_1^2} + \frac{d_2^2}{a^2 - d_2^2} + 1 \right]^{-1/2} \quad (\text{B.5})$$

Bibliography

- [1] L. W. Schmerr, Jr, *Fundamentals of Ultrasonic Nondestructive Evaluation. A Modeling Approach*. Plenum Press, 1998.
- [2] J. L. Rose, *Ultrasonic Waves in Solid Media*. Cambridge University Press, 1999.
- [3] B. A. Auld, *Acoustic Fields and Waves in Solids*. Krieger Publishing Company, second ed., 1990.
- [4] G. A. D. Briggs, *Acoustic Microscopy*. Oxford: Clarendon Press, 1992.
- [5] W. P. Mason, ed., *Physical Acoustics. Principles and Methods*, vol. 1A. Academic Press, 1964.
- [6] L. M. Brekhovskikh, *Waves in layered Media*. New York: Academic Press, 1960.
- [7] R. E. McKeighen, "Design guidelines for medical ultrasonic arrays," in *SPIE International Symposium on Medical Imaging*, 1998.
- [8] S. W. Smith, G. E. Trahey, and O. T. von Ramm, "Two-dimensional arrays for medical ultrasound," *Ultrasonic Imaging*, vol. 14, pp. 213–233, 1992.
- [9] K. Erikson, A. Hairston, A. Nicoli, J. Stockwell, and T. White, "A 128×128 ultrasonic transducer array," in *IEEE Ultrasonics Symp.* (S. C. Schneider, M. Levy, and B. R. McAvoy, eds.), p. 1625, IEEE, 1997.
- [10] K. Erikson, J. Stockwell, A. Hairston, J. Marciniak, and R. McPhie, "Matrix arrays for the 21st century," in *Acoustic Imaging*, (in print).
- [11] S. Leeman and A. J. Healey, "Field analysis with a new field simulation and propagation technique," in *Acoustical Imaging* (M. Halliwell and P. N. T. Wells, eds.), vol. 25, pp. 41–50, Kluwer Academic/Plenum Publishers, 2000.
- [12] J. D. Plummer, R. G. Swartz, M. Maginness, J. R. Beaudouin, and J. D. Meindl, "Two-dimensional transmit/receive piezoelectric arrays: Construction and performance," in *IEEE Trans. on Sonics and Ultrasonics*, vol. 25, pp. 273–280, 1978.

- [13] P. K. Weber, R. M. Schmidt, B. D. Tylkowsky, and J. Steck, "Optimization of random sparse 2-D transducer arrays for 3-D electronic beam steering and focusing," in *Proceedings of the IEEE Ultrasonics Symposium*, pp. 1503–1506, 1994.
- [14] D. H. Turnbull, *Two-Dimensional Transducer Arrays for Medical Ultrasonic Imaging*. PhD thesis, University of Toronto, 1992.
- [15] R. Maev, S. Titov, A. Denisov, E. Maeva, F. Ewasyshin, and J. Paille, "Method and apparatus for assessing quality of spot welds." US Patent No. 99-1205US2RAF Application from 18.06.2000.
- [16] A. Ptchelintsev and R. G. Maev, "Ultrasonic array transducer." US Patent No. 98-1258US2RAF Application from 7.11.1998.
- [17] J. H. Heinbockel, *Introduction to Tensor Calculus and Continuum Mechanics*. Trafford, 2001.
- [18] L. D. Landau and E. M. Lifshitz, *Theory of Elasticity*, vol. 7 of *Course of Theoretical Physics*. Pergamon Press, third ed., 1986.
- [19] R. G. Maev, A. Ptchelintsev, and A. A. Denisov, "Ultrasonic imaging with 2D matrix transducers," in *Journal for Material Characterization*, (Bristol, UK), Mar. 2000. 25th Intern. Acoustical Imaging Symposium.

Vita Auctoris

Name: Alexey A. Denisov
Place of birth: Moscow, Russia
Date of birth: July 15, 1975
Education: BSc in 1996 and MSc in 1998 from
Moscow Institute for Physics and Technology (State University)

Articles in Referred Journals

- R. G. Maev, J. Sokolowski, H. Lee, E. Maeva, and A. Denisov, "Bulk and subsurface structure analysis of the 319 aluminum casting using acoustic microscopy methods," *Journal for Material Characterization*, vol. 46, no. 2, pp.326, 2001.
- R. Gr. Maev, L. A. Denisova, E. Yu. Maeva, and A. A. Denisov, "New data on histology and physico-mechanical properties of human tooth tissue obtained with acoustic microscopy," *Ultrasound in Med. and Biol.*, vol. 28, no. 1, pp. 131–136, 2002.
- R. Gr. Maev, L. A. Denisova, E. Yu. Maeva, A. A. Ptchelintsev, A. Denisov, "Investigation of the microstructure and quantitative evaluation of biomechanical properties of dentin using microscopy technique," *Journal of Biomedical Technology*, vol. 24, no. 10, pp. 164–175, 2000.
- R. Gr. Maev, Yu. M. Maximovsky, L. A. Denisova, E. Yu. Maeva, A. A. Denisov, T. D. Chirkova, and D. A. Domyshev, "Acoustic microscopy: a new method for investigation of dental tissues," *Stomatology*, no. 5, pp. 14-19, 2000.
- R. Gr. Maev, L. A. Denisova, E. Yu. Maeva, A. A. Denisov, A. A. Pchelintsev, "Quantitative evaluation of elasto-mechanical properties of human teeth," *News in Dentistry*, no. 2, Moscow, 2001.

Conference Proceedings

- R. Maev, A. Denisov, A. Volozhin, L. Denisova, E. Maeva, A. Krasnov, V. Popov, A. Popova, and E. Bakulin, "Investigation of Polyamide-hydroxyapatite bone implant surface microstructure with acoustic microscopy methods," in *26th International Acoustical Imaging Symposium*, Windsor, Ontario, p. 25, 2001.
- L. Denisova, R. Maev, I. Matveichuk, Yu. Denisov-Nikolsky, A. Denisov, and E. Maeva, "Investigating compact bone microstructure and mechanical properties using acoustic microscope," in *26th International Acoustical Imaging Symposium*, Windsor, Ontario, p. 11, 2001.
- R. G. Maev, A. Ptchelintsev, and A. A. Denisov, "Ultrasonic imaging with 2D matrix transducers", in *25th International Acoustic Imaging Symposium*, Bristol, UK., Mar. 2000, p. 326, 2000.
- R. Gr. Maev, L. A. Denisova, E. Yu. Maeva, and A. Denisov, "Mineralized tooth tissue study using scanning acoustic microscopy," in *25th Intern. Acoustical Imaging Symposium*, Bristol, UK, 2000.
- A. Denisov, E. Yu. Maeva, L. Denisova, R. Gr. Maev, "Ultrasonic visualization of healthy and pathological human dental tissue using acoustic microscopy," in *Proc. of the II Biophysical Congress*, v. 2, Moscow, Russia, pp. 668–670, August 1999.
- R. G. Maev, A. Ptchelintsev, and A. A. Denisov, "Acoustical imaging using matrix of piezoelectric transducers for nondestructive evaluation of plastic composites," in *Sixth Intern. Conf. on Composites Engineering*, Orlando, USA, pp. 665–668, June 1999.

Research Reports

- R. G. Maev, A. Ptchelintsev, and A. A. Denisov, E. Maeva, and F. Seviarin, "Development of the prototype for NDE portable system for spot weld joints inspection. Version for fill-scale plant tests," current progress report for DaimlerChrysler, University of Windsor, Apr. 1999.
- R. G. Maev, A. Ptchelintsev, E. Maeva, and A. A. Denisov, and F. Seviarin, "Various ultrasonic techniques for spot weld quality monitoring. Comparative results," progress report for DaimlerChrysler, University of Windsor, May 1999.

Patents

- R. Maev, S. Titov, A. Denisov, E. Maeva, F. Ewasyshin, and J. Paille, “Method and apparatus for assessing quality of spot welds.” US Patent No. 99-1205US2RAF Application from 18.06.2000.